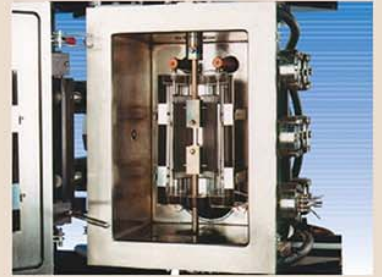




The Scientific Bulletin of Valahia University MATERIALS and MECHANICS



2016

Vol. 14 No. 11

SPECIAL CONCRETE WITH POLYMERS

Nicolae ANGELESCU¹, Ioana ION¹, Darius STANCIU¹,
José BARROSO AGUIAR², Elena Valentina STOIAN¹, Vasile BRATU¹

¹Valahia University of Targoviste, Faculty of Materials Engineering and Mechanics, Str. Aleea Sinaia, No. 13, Targoviste, Romania

²Minho University, Guimarães, Portugal

E-mail: nicolae.angelescu@yahoo.com, elenastoian22@gmail.com

Abstract. *The development of polymeric materials offers new perspectives of science and technology due to their outstanding properties. These properties are obtained either due to the effect of dispersion polymers and their polymerization either due to their intervention in structure formation. They were prepared epoxy resin polymer concrete, Portland cement, coarse and fine aggregate and to evaluate the influence of resin dosage on microstructures and density of such structures reinforced concrete mixtures. The paper detailing the raw materials used in experimental works and structural properties of concrete studied.*

Keywords: *polymer concrete, density, porosity, epoxy resin*

1 INTRODUCTION

Polymer materials are widely used for many years but recently they are present in almost every branch of civil engineering due to their specific. Since polymer materials improve the technical properties of these systems are often used as additives or components of mixtures. If concrete structures with polymers is possible to change their composition due to, on the one hand, the demands of the market and, on the other hand, the need for development of high mechanical strength.

Polymers in concrete or concrete type composites - polymer drew attention to the trade because these innovative materials have superior mechanical and chemical properties [1]. These composites have jumped on the widespread development of resistance structures, renovation and restoration of concrete structures already in place.

Uncured epoxy resins offer greater fluidity before hardening, and increases the adhesion force between particles with positive consequences on strengthening the mixture.

Reactions of polymers and cement particles in the concrete mix have great influence on the performance quality and have been scrutinized in recent years such as: concrete with vinyl polymers [2] concrete with vinyl chloride [3], polystyrene [4] or phenolic resins [5].

The properties of concrete composites - polymer are influenced by the chemical nature of the polymer type and quantity used.

Table 1 The characteristics of the polymer

2 RAW MATERIALS

Technical data and chemistry	Epoxy resin	Hardener
Function	Reducing the water content, strengthens the concrete structure	Contribute to polymerize the resin
Appearance	White liquid	Yellowish liquid
Relative density (20°C):	1,05 g/cm ³	1.3 g/cm ³
pH, 20°C:	5	5
Viscosity (20°C):	< 100 cps	<90
Chloral content:	≤ 0,1 %	≤ 0,1 %
Alkali content	≤ 2 %	≤ 2 %

For the preparation of polymer concrete have been used:
- SIKA epoxy resin range, which combined with hardener and cement concrete forming polymer binder [6]
- Cement CEM I 42.5R,
- Aggregates crushed granite in two varieties: 0-4 mm (Sort I) and 4-8 mm (Sort II).

2.1. Polymers

It used epoxy resin and hardener in the composition SikaFlor81 era. Technical data for this polymer are shown in Table 1 [6].

The polymers are designed to improve both the workability and strength of concrete mixes with

polymers. Epoxy resins have two roles within compositions:

- by polymerization of influencing their structure, using its elastic connection points between the constituent materials,
 - forms a thin layer on the cement particles, negatively charged them and produces a repulsion between them.
- By participating directly in the formation of the mechanical strengths of their influence.

2.2 The cement

The cement used was the type CEM I 42.5R, Blaine specific surface area equal to 380 m² / kg and specific gravity of 3.12 kg / m³ [7]. Oxidic composition thereof is shown in table 2.

2.3 The aggregate

In terms of physical properties, borders are hard rocks, compact, with fine grain size and / or coarse metamorphic or volcanic origin, with the following characteristics:

- hardness: 6 to 7 on the Mohs scale,
- Density: 2.6 - 2.8 Kg / cm³
- compressive strength: 140-210 N / mm²,
- modulus of rupture: 15-25 N / mm²,
- water absorption: 0.1-0.6%
- relatively low porosity,
- resistant to weather.

Table 2 The composition -oxide of (CEM I 42.5 R)

Oxide composition, %	
Type of oxid	The cement CEM I 42,5R
SiO ₂	19.30
Al ₂ O ₃	5.57
Fe ₂ O ₃	3.46
CaO	63.56
MgO	0.86
Na ₂ O	0.13
K ₂ O	0.80
SO ₃	2.91
Cl	0.013
TiO ₂	-
L.O.I.	2.78

In terms of chemical composition, borders are igneous rocks composed of quartz, feldspar and minerals such as ferromagnesian Kriol, chlorite, garnet etc. A typical granite will have the following chemical composition:

- Quartz (SiO₂): 70-75%
- aluminum oxide (Al₂O₃): 10-15%
- Calcium oxide (CaO): 0.5%
- Peridot (MgO): 0.5%
- Bauxite (Al₂O₃.nH₂O): 2-4%
- Alkaline: 4-6%
- Peridot (TiO₂): less than 0.5%
- Loss on ignition (PC) less than <0.5%.

In figure 1 are presented the grading curve of the aggregates used [8] of the two types of sort mentioned above.

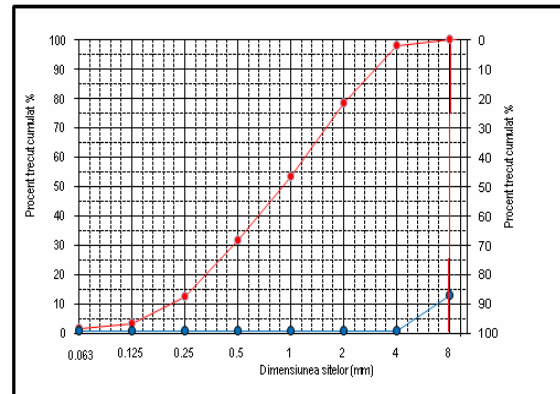


Fig. 1. Analysis of particle size of the aggregate used

2.4 Obtaining the polymer concretes

In this study, three compositions were made of polymer concrete. Epoxy resin content varied between 1 and 10%. Dosages satisfy the workability required.

Polymer concretes with different compositions were prepared by mixing the required amount of binder (cement and epoxy with hardener) the aggregate and water. On hardened concrete we studied the microstructure and were determined their porosity and densities.

3 RESULTS AND DISCUSSIONS

3.1 The density polymer concrete

It analyzed the influence of dosage resin density concrete, which were considered three dosages of resin and experimental data are presented in figure 2.

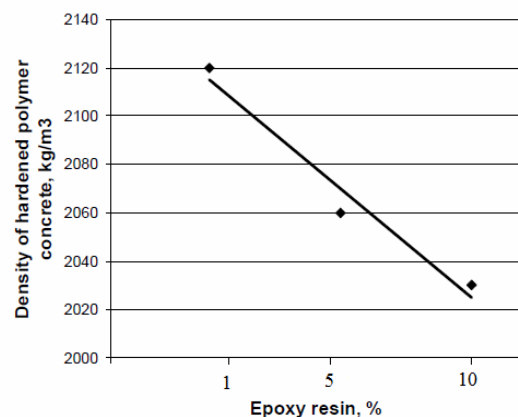


Fig. 2. Hardened concrete density variation depending on the content of resin

The results show that the density of concrete reinforced with polymer decreases the dosage of resin, featuring a linear dependence.

For all analyzed polymer concrete density values have shown that they can be classified as normal concrete with densities (> 2000 kg / m³ and <2600 Kg / m³) [9]

3.2 The microstructure of the polymer concrete

Figure 3 shows the concrete surface obtained only from aggregate, cement and water without polymer additives, where they notice the presence of a large number of goals with a maximum diameter of 0.35 mm.

In the ordinary concrete, it can be seen as byproducts have developed moisturizers and how embedding of aggregate in the mix.

Not can notice neither any formation elastic but just how new hydration byproducts covers both unit and still-hydrated cement particles. These neoformation of hydration continues to develop and evolve over time, as the process evolves hydrating cement particles.

On the other hand, may be noticed in figure 4 an increasing number of goals in the concrete structure of polymers in small proportion (1%), but their diameter shrinks. There had not been bridging linking aggregate value this polymer dosage.

In Figure 5 which shows the microscopic analysis of a concrete with a rate of 5% polymer resin dislocations observed in concrete. It can be concluded that the proportion of value agglomeration process begins polymer resin, which tends to achieve concrete links between constituents.

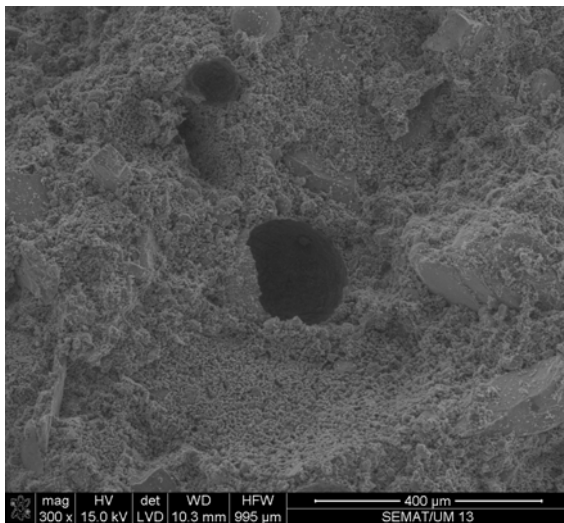


Fig. 3. Microscopic analysis of a concrete normal

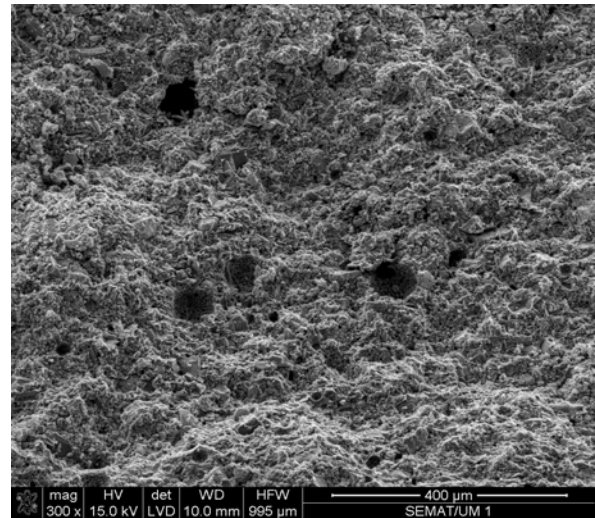


Fig. 4. The microstructure of concrete with 1% resin

In figure 6, it is shown the structure of a concrete containing epoxy resin in a proportion of 10%, where there is clear tendency to form bridges stretch between particles components of concrete, which results in increased strength in compression and tension by bending the structures strengthened .

At the same time congestion can be seen in different places crosslinking of the polymer, and a greater number of such links between particles.

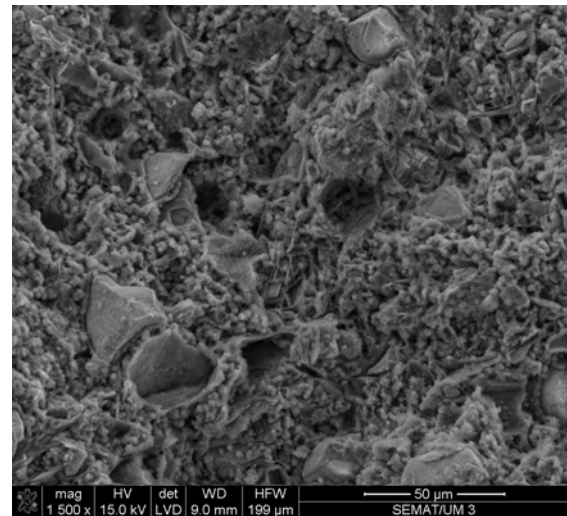


Fig. 5. The microstructure of concrete with an epoxy resin proportion of 5%

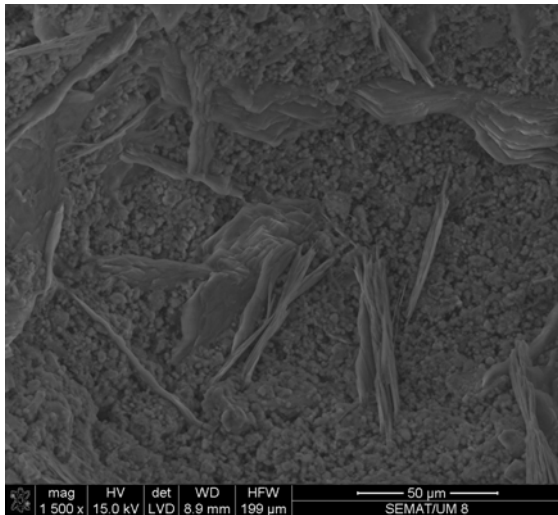


Fig. 6 The microstructure of concrete with an epoxy resin proportion of 10%

It can be concluded that an amount of 10% epoxy resin can reduce the diameters of the holes, you get a denser structure and can also influence the hardening of concrete due to congestion elastic resin that tend to blend aggregates.

3.3 The porosity of concrete polymer

Table 3. The porosity of concretes

Type concrete	The porosity, %
Concretes usual	7.2
Concrete with epoxy resin 1%	7.2
Concrete with epoxy resin 5%	7
Concrete with epoxy resin 10%	7.1

From table 3 it can be seen that the porosity of concretes containing polymers is close to that of concrete without polymers, but as was noted above volume is higher goals without polymer concrete structure. Polymer concretes tendency exists to fill these gaps with polymer clusters, which have the effect of improving the mechanical properties thereof.

4 CONCLUSIONS

Polymer concrete were obtained by using different dosages of epoxy resin (1-10%), with cement and aggregate.

Microscopic analysis of the resulting polymer concrete structure with the 5% - 10% epoxy resin to form a crosslinked structure of the polymer concrete with the smaller holes.

The density of the concrete cured state with varying proportions of polymer allows for the concrete normal it

as a normal volume weight. The resin content increases was a decrease linear density in its cured state.

The porosity of concrete polymer is lower than usual and also number of goals inside the structure is lower, a consequence of the fact that these holes are partly filled by clusters of resin. By using epoxy resin to prepare concrete structures are obtained compact with small holes.

5 REFERENCES

[1] Lech Czarnecki “ Concrete polymer composites (C - PC) – Change per continuation”, 13th International Congress on Polymers on Concrete, Portugal, 2010.
 [2] Sugama T, Kukacka L.E. “ The effect Of dicalcium silicate (C₂S) and tricalcium silicate (C₃S) on the thermal stability of vinyl type polymer concrete”, *Cem . Concr.Res.*,vol 9, No 1, p 69-76.
 [3] Larbi J.A., Bijen J.M.J.M. “ A study of interface between some polymer dispersionand Portland cement during hydration”, *Proc Of VI ICPIC*, p. 185 – 192.
 [4] Putterman M., Malorny W, “ Some doubts and ideas on the microstructure formation of PCC”, *Proc Of IX ICPIC*, sept 14-18, p. 165-178.
 [5] Nair, Priya and A. Paul ”Microstructure of phenolic resin cement concrete”, *Proc Of 25th Conference On Cement Muicroscopy And Symposium On Rietveld Techniques*, ICMA, U.S.A.. 2003.
 [6] www.sika.com.
 [7] Fisa tehnica Ciment CEM I, 42,5R.
 [8] European Standard EN 933 – 1/2000 – Tests for geometrical properties of aggregates.Determination of particle size distribution, Sieving method.
 [9] European Standard EN 12390- 7/ 2003 – Testing hardened concrete. Density of hardened concrete.

Acknowledgement

This work was partly financed by the European Social Fund through the POSDRU/CPP107/DMI1.5/S/77497 Program for PhD. Student

DETERMINATION OF OVERALL HEAT TRANSFER COEFFICIENT BY SIMPLE THERMAL ANALYZE

Mirela POPESCU, Tibor BEDO, Bela VARGA

Transilvania University of Brasov, Material Science Department, 29 Eroilor Blvd., 500036, Brasov, Romania

E-mail: mireladrageoiu1@yahoo.com, bedo.tibor@unitbv.ro, varga.b@unitbv.ro

Abstract. To know more precise the value of overall heat transfer coefficient is on a special importance to programs (software) that models the solidification process for project casting technology in order to optimize them by dimensioning and appropriate placement both the gating system and the risers for eliminate casting defects, shrinkages. The paper aims to determin the value of overall heat transfer coefficient on the cooling curve recorded in casting-solidification real conditions. The values obtained for the overall heat transfer coefficient $(2.34 \text{ to } 25.41) \cdot 10^{-4} [\text{cal/s.grad.cm}^2]$ for different casting conditions prove that this parameter can not be considered as a constant of the casting mould material.

Keywords: overall heat transfer coefficient, thermal analyze, cooling curve, mould vibration, aluminium alloy.

1. INTRODUCTION

The properties of part castings are determined by solidification structure. The solidification structure is considered both the granulation and distribution and fineness of eutectic phases and the dimension and the shapes of intermetallic compounds formed in acceptable limits of metal impurities. The casting structure is caused by cooling rate applied of alloy both in liquid state and in solidification range. Cooling rate value is determined by the intensity of heat exchange between the liquid alloy and the mould. The intensity of heat exchange can be appreciate by the overall heat transfer coefficient value. At the same time, as accurate as possible knowing of overall heat transfer coefficient value is on special importance in forming operation of solidification process softwares for design casting technology in order to optimize them by dimensioning and appropriate placement both the gating system and the risers for eliminate casting defects, shrinkages [1-2]. These desiderates have determined the resumption and intensification of researches in this field [3-7]. A series of works [8-14] analyzes the overall heat transfer coefficient for concrete cases of casting alloys processing.

This paper aims to determin the value of overall heat transfer coefficient on the cooling curve recorded in casting-solidification real conditions.

As it is known, the cooling curves are described by an exponential function (1):

$$t = t_0 + (t_k - t_0) e^{-w\tau} \quad (1)$$

where: t_k - represents initial temperature of melt; t_0 - initial temperature of mould and τ -time.

The "w" coefficient includes both the geometrical characteristics of casting sample and thermo-physical properties of cast alloy as well as the overall heat transfer coefficient that characterizes the heat exchange between melt and mould, Eq. (2):

$$w = \frac{k \cdot A}{m \cdot c} \quad (2)$$

where: m- is alloy weight, casting sample;
c- specific heat for alloy;
A- the surface where is performed the sample cooling,

while k- is the overall heat transfer coefficient between casting sample and mould.

It must be mentioned that this equation is valid only on temperature ranges where there are not phase transformations produced. In experimental determinations it is considered as 30°C the initial mould temperature, while the initial melt temperature corresponds to maximum value on cooling curve.

2. EXPERIMENTAL DETERMINATIONS, RESULTS

In context of experimental determinations there were cast cylindrical and tubular samples in graphite mould (G), refractory brick (C) and sodium silicate made moulds (S), from various nonferrous alloys: lead alloy–PbSn37 (solder), hypoeutectic silumin - AlSi7Mg0.3 and eutectic silumin - AlSi12. In all cases, it was used tight moulds and the supplying of mould cavity with liquid alloy it was accomplished by direct casting, through the pouring cup racticed in the top of the wall mould (in the cover), Fig. 1.

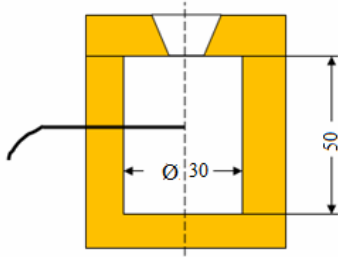


Fig.1 Casting mould with thermocouple assembled

To measure temperature there were used type K thermocouples. In order to register more accurate temperature, the tops of thermocouples were left open (without protective sheath) and covered with a refractory paint layer. Thermocouples' peaks in all experimental determinations were placed at half height of the sample and in the middle of cross-section. To register temperature was used an ADAM type with 11 channels interface. At mathematical processing of experimental data to determine the proper equations of cooling curves above the liquidus temperature was used ORIGIN program. In Table 1 there are presented the sizes of castings samples and geometric and thermo-physical characteristics of them, necessary to calculate "w" coefficient, in Eq. (1).

Table 1 Sample codification

Sample code	Alloy	Mould material	Sample mould	Sample dimension [mm]	Alloy density [g/cm ³]	A [cm ²]	m [g]	c [cal/g·°C]		
1-C	Pb	Refractory brick	cylindrical	Ø 30 × 50	11.3	61.23	399	0.03		
2-G		Graphite								
3-C	PbSn37	Refractory brick		Ø 40 × 50	9.92	61.23	350	0.041		
4-C-p										
5-C	AlSi7	Sodium silicate process	bar	Ø 60 × 150	2.7	340	1145	0.29		
6-C-v	Mg0.3		tube	Ø 100/40 × 150					791	2670
7-S-	AlSi12		tube	Ø 160/100 × 100					1061	3307

Index "p" for 5-C-p sample means that the mould has been preheated, while the index "v" for 6-C-v specimen means that, during solidification, the mould was subjected to mechanical vibrations. Concerning to alloys, density and specific heat have been calculated by additivity rules.

Further it is shown the working methodology for determining the value of overall heat transfer coefficient by a detailed description of work stages in case of 1-C sample.

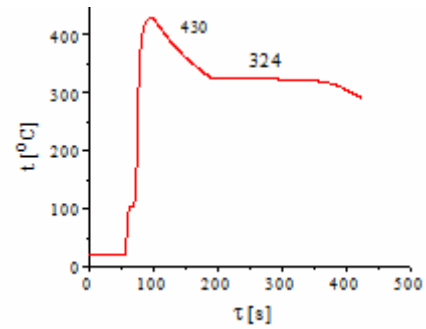


Fig.2 Cooling curve recorded for 1-C sample

Figure 2 shows the cooling curve recorded for 1-C sample. For establishing Eq. (1), it is significant just the portion corresponding to alloy cooling in liquid, Figure 3. By mathematical processing of experimental datas (ORIGIN program) results the Eq. (1.a), which perfectly overlaps with the experimental curve.

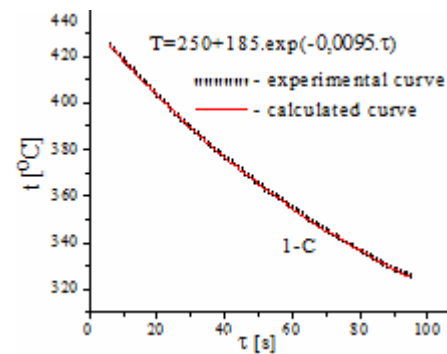


Fig.3. Experimental and calculated cooling curve for temperature above the solidification one

$$t = 247.6 + 182 \cdot \exp(-0.0093 \cdot \tau) \quad (1.a)$$

Because the coefficients values „t₀“and „(t_k - t₀)“ obtained in Eq. (1.a) differ from those imposed by initial conditions of the experiment and that they were the basis in relation (1) deduction, it is proceed to replace them, resulting:

$$t = 30 + 397.86 \cdot \exp(-0.0093 \cdot \tau) \quad (1.b)$$

that is no longer overlaps with the experimental curve, Figure 3. Curve superposition corresponding to Eq. (1.b) with the experimental curve is performed by replacing exponent "w" with "w_{adjusted}", in such a way to ensure the best possible approximation of experimental cooling curve corresponding to the cooling of alloy in liquid phase. By repeated tests, from Eq. (1.b) result Eq. (1.c),

$$t = 30 + 397.86 \cdot \exp(-0.0033 \cdot \tau) \quad (1.c)$$

The Eq. (1.c) by „t₀“and „(t_k - t₀)“ coefficients respects the initial conditions and, at the same time, by choosing appropriate "w_{adjusted}" overlaps, with good approximation, with the experimental cooling curve for higher than liquidus temperatures, in presented case, than the solidification temperature, Figure 4.

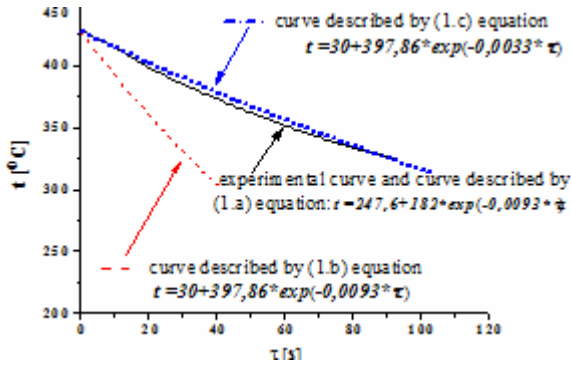


Fig.4. Recorded cooling curve and corresponding curves of Eq. (1.a), (1.b), (1.c) for 1-C sample

Further, based on the value of “ $w_{adjusted}$ ” coefficient in Eq. (1.c) is calculated the overall heat transfer coefficient, resulting $k = 0.00065 \text{ cal / s.grad.cm}^2$. The values of corresponding coefficients in Eq. (1.a): “ $w_{adjusted}$ ” and overall heat transfer coefficient are listed in Table 2.

Table 2 Coefficients value in (1.a) equation, “ $w_{adjusted}$ ” and overall heat transfer coefficient

Sample code	t_0 [°C]	$(t_s - t_0)$ [°C]	$w \cdot 10^{-4}$ [1/s]	$w_{adjusted} \cdot 10^{-4}$ [1/s]	k	
					[cal/s.grad.cm ² 10 ⁻⁴]	[W/grad.cm ²]
1-C	247.6	182.0	93.0	33.0	6.45	27.0
2-G	302.0	34.9	2.300	130.0	25.41	107.0
3-C	182.0	280.0	52.0	24.0	5.62	24.0
4-C-p	236.0	260.0	18.6	10.0	2.34	10.0
5-C	479.0	239.0	20.0	6.0	3.78	16.0
6-C-v	541.0	196.0	78.0	15.0	9.46	40.0
7-S	508.5	178.7	47.3	9.0	8.80	37.0
8-S	530.6	138.2	134.2	20.0	19.60	82.0
9-S	537.7	137.1	93.6	12.0	10.80	45.0

For 2-G sample calculations results are shown in Table 2.

In case of PbSn37 solder casting was done in non-preheated and at 100°C preheated refractory brick moulds. Figure 5a there are presented the cooling curves recorded, while in Figure. 5b there are the sections of cooling curves corresponding for cooling in a liquid state and the appropriate deduced regression equations curves.

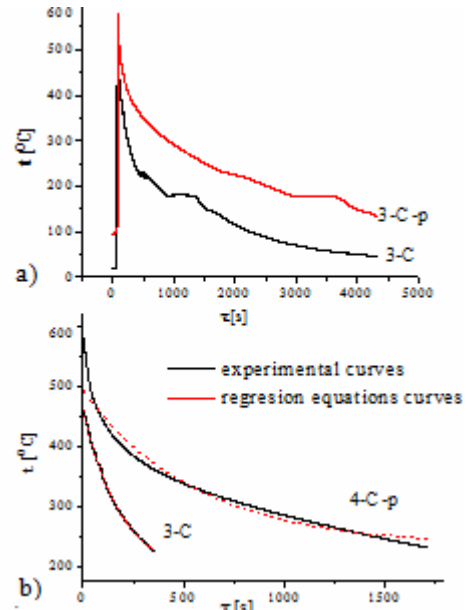


Fig.5. Cooling curves recorded for samples 3-C and 4-C-p (a) and corresponding sections of the liquid phase (b)

The values of the regression equations coefficients are presented in Table 2.

Through experiments, for “ $w_{adjusted}$ ” coefficient results values: 0.0024 and 0.001 s⁻¹, respectively.

Finally, the values for overall heat transfer coefficient results are: 0.000562 for non-preheated mould and 0.000234 cal/s.grad.cm² in case of preheated mould.

For 5-C and 6-C-v samples cooling curves are shown in Figure. 6. As there is noted in Table 1, the solidification of 6-Cv sample has been achieved with mechanical vibration on mould, the parameters were: frequency 50 Hz, amplitude 0.07 [mm], speed 14 [mm / s] and acceleration 15 [m/s²], [15].

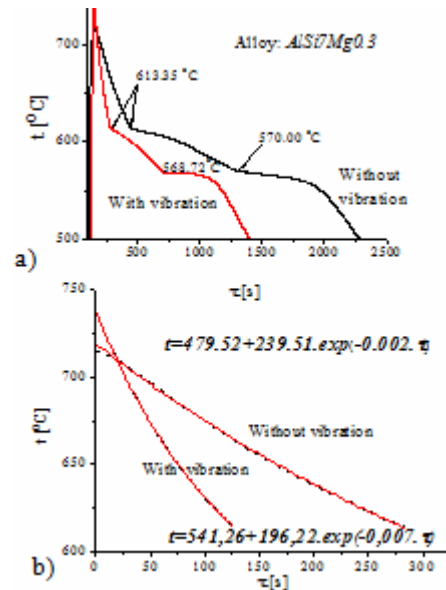


Fig.6. Cooling curves recorded for the samples 5-C and 5-C-v (a) and corresponding sections of the liquid phase (b)

By processing the corresponding curve of alloy cooling in liquid state resulted the regression equations like relation (1) whose coefficients are shown in Table 2.

Through tests, for “ $w_{adjusted}$ ” coefficient, the values are: 0.0006 and 0.0015 s^{-1} , respectively. Therefore, the value of overall heat transfer coefficient obtained is 0.000378 for nonvibrate mould and 0.000946 $cal/s.grad.cm^2$ for vibrated mould

In the next series of determinations, three samples were cast in sodium silicate as binder moulds (samples codes - 7S, 8S and 9S, respectively):

- bar type casting: $\varnothing 60 \times 150$, volume of 424 cm^3 .
- cylindrical casting with a high H/ \varnothing ratio: dimensions $\varnothing 100/40 \times 150$, volume of 989 cm^3 and wall thickness of 30 mm,
- cylindrical casting with a small H/ \varnothing ratio: dimensions $\varnothing 160/100 \times 100$, volume of 1,225 cm^3 and wall thickness of 30 mm.

It should be mentioned that the outside diameter for these three moulds was 180, 200 and 240 mm, respectively, and the thickness of the front parts (up / down) was 50 mm. Further, it is also specified the ratio between the volume of metallic castings and volume of the mould (moulding sand) in order to obtain a more evident image on the heat exchange between the liquid alloy and mould: at sample S-7 is 0.125, at S-8 one is 0.266 and at S-9, the last sample, is 0.371.

For these determinations it has been used a silumin with easy hypoeutectic composition. The alloy composition is shown in Table 3.

Table 3 Chemical composition of the alloy AlSi 12

Element	Content [wt%]	Element	Content [wt%]
Al	87,3	Zn	0,74
Si	9,7	Pb	0,07
Fe	0,8	Sn	0,06
Cu	0,8	Ni	0,02
Mn	0,14	V	0,01
Mg	0,3	Ti	0,03
Cr	0,03		

Considering the complex composition of the alloy, the eutectic temperature was calculated with Mondolfo’s relation:

$$t_{Ecalc} = t_{E0} - (12.5/[Si]) \{ (4.43[Mg] + 1.43[Fe] + 1.93[Cu] + 1.7[Zn] + 3[Mn] + 4[Ni]) \} \approx 570 \text{ } ^\circ\text{C}$$

where:

- t_{E0} - eutectic temperature: 577 $^\circ\text{C}$ in Al-Si Thermal Equilibrium Diagram
- t_{Ecalc} - eutectic temperature for complex allied alloy
- [Mg]-concentration of allied element (metallic impurities).

In Fig. 7a it is presented a draft of the casting mould and the placement of the thermocouples: in the middle of the

wall thickness for first one, on 10 mm from casting surface for the second and just on melt-mould interphasic surface for the third. Fig. 7b shows the mould completely ready, and in Fig. 7c there is the used assembly to record cooling curves.

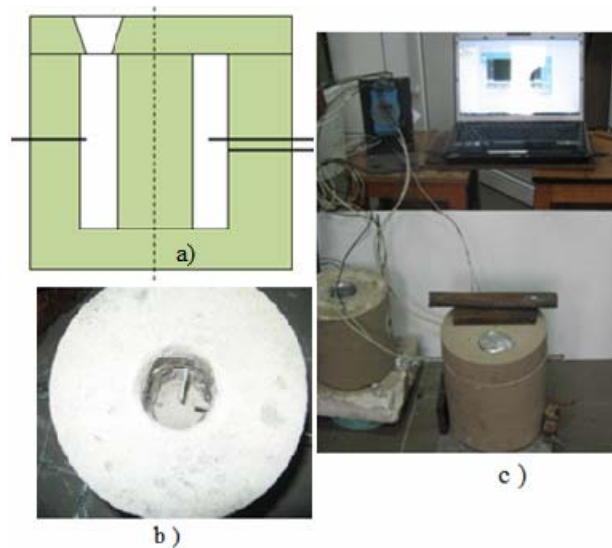


Fig. 7. Casting mould and the used assembly

To calculate the overall heat transfer coefficient were used recorded curves by thermocouples placed in the middle of the section, Fig. 8a.

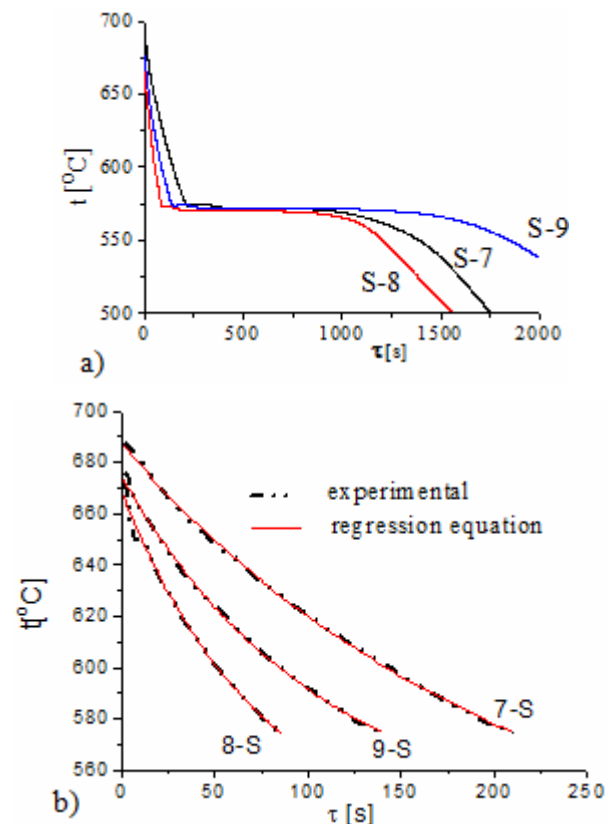


Fig.8. The cooling curves recorded for samples 7-S, 8-S and 9-S (a) and corresponding sections of liquid phase (b)

It is worth mentioning that for all three cooling curves it is observed the undercooling phenomenon both to primary crystallization and to eutectic transformation. The eutectic temperatures indicated by cooling curves are 0.6 to 2 degrees higher than the corresponding value, calculated by Mondolfo's equation.

The regression equations (ratio (1)) were obtained after the processing upon corresponding curves of cooling alloy in the liquid state, Fig. 8b. In Table 2 are shown these coefficients. By tests, the resulting values for " $w_{adjusted}$ " coefficient are 0.0009; 0.002 and 0.0012 s^{-1} , respectively. Therefore, for the overall heat transfer coefficient have been obtained 0.00088 (sample S7), 0.00196 (S8) and 0.00108 [$cal/s.grad.cm^2$] for sample S9. These values are much lower than those reported in work [3], which refers to Al-Cu4.5% alloy cast in cylindrical moulds made with sodium silicate as binder and hardened with carbon dioxide.

It should be mentioned that for all casting samples, the Biot criterion is much smaller than one (varies in the range 0.005 to 0.006), which means that during the cooling of liquid alloy, the heat transported from inside the melt to melt-mould interphase surface is much higher than that what can be absorbed by the mould material, which induced a volume solidification.

3. CONCLUSION

Based on obtained values for the overall heat transfer coefficient (Table 2) it can be said that it depends very much on casting conditions (melt temperature, casting dimensions, mould material and inner cores presence).

Casting in graphite moulds determines of about 4 times increase on overall heat transfer coefficient compared with that cast in refractory brick moulds.

Preheating the melt determines the decrease of approximately 2.4 times of overall heat transfer coefficient.

The mould vibration cause the increase about 2.5 times of the overall heat transfer coefficient. This increase is the result of penetration liquid alloy in mould surface depressions which causes a better contact between the melt and mould material but also leads to grow roughness castings surface.

Similar effects can have both melt overheating by increasing fluidity and decreasing the surface tension and casting high pieces, to which the metallostatic pressure can cause a better contact between the melt and the mould material. This conclusion is in agreement with results reported in [6, 9, 10], concerning the pressure effect on the value of global heat transfer coefficient.

In case of casting in sodium silicate moulds to 8-S sample, the overall heat transfer coefficient is about 2 times greater than for those other two samples (7-S and 9-S). The significant difference can only be attributed to differences between the geometrical characteristics of those three moulds made by sodium silicate process.

The obtained values of overall heat transfer coefficient (2.34 to 25.41) $\cdot 10^{-4}$ [$cal/s.grad.cm^2$]), for different casting conditions demonstrates that this parameter can not be considered as a mould material constant.

It is mention that the method described for determining the overall coefficient of heat transfer from the melt-mould interface is an average value and takes account, incorporates, the so controversial phenomenas effect from melt-mould area contact.

4. ACKNOWLEDGMENTS

We hereby acknowledge the structural funds project, (SOP HRD), ID137516 financed from the European Social Fund and by the Romanian Government and the structural funds project POSDRU/159/1.5/S/137516 for providing the infrastructure used in this work.

5. REFERENCES

Journals:

- [1] Varga Bela, Musteață Florin, Ciobanu Ioan, Bedo Tibor, Munteanu Ion Sorin, Crișan Aurel: Study on Shrinkage Development Inside an Al-Si Alloy Casting by Computer Solidification Simulation, , RECENT Vol. 17, no. 1(47), March, 2016, pp. 55-68
- [2] Bedo Tibor, Dăian Marcel, Varga Bela, Stoicănescu Maria, Crișan Aurel, Ciobanu Ioan: A Simulation and Experiment Concerning the Solidification of an Al-Zn Alloy Casting, RECENT, Vol. 17, no. 2(48), July, 2016, pp. 83
- [3] Bencomo A., Bisbal R., Morales, R.: Simulation of the aluminum alloy A356 solidification cast in cylindrical permanent molds, Revista Matéria, v. 13, n. 2, pp. 294 – 303, 2008
- [4] Konopka Z., Łągiewka M., Zyska A.: Evaluation of the heat transfer coefficient at the metal-mould interface during flow, Archives of Foundry Engineering, Volume 7, Issue 4/2007, 101-104
- [5] Ulkarni S.N. K., Adhkrishna D.K. R: Effect of casting/mould interfacial heat transfer during solidification of aluminium alloys cast in CO₂-sand mould, Materials Science-Poland, 29(2), 2011, pp. 135-142
- [6] Jabbari M., Fardi Ilkhchy A., Davami P.: Effect of pressure on heat transfer coefficient od A356 aluminium alloy, Journal of Materials Science and Engineering with Advanced Technology, Volume 4, Number 1, 2011, Pp 1-20
- [7] Sahin H. M., Kocatepe K., Kayıkcı R., Akar N.: Determination of unidirectional heat transfer coefficient during unsteady-state solidification at metal casting–chill interface, Energy Conversion and Management 47 (2006) 19–34
- [8] Felczak, G. De Mey and B. Więcek, Determination of the heat transfer coefficient distribution, Quantitative InfraRed Thermography, 2016, pp 236-241
- [9] Fardi Ilkhchy A., Varahraam N., Davami P., Evaluation of Pressure Effect on Heat Transfer Coefficient at The Metal- Mold Interface For Casting of A356 Al Alloy,

- Iranian Journal of Materials Science & Engineering Vol. 9, Number 1, March 2012
- [10] Fardi Ilkhchy A., Jabbari M., Davami P., Effect of pressure on heat transfer coefficient at the metal/mold interface of A356 aluminum alloy, International Communications in Heat and Mass Transfer 39 (2012) 705–712
- [11] Jer-Haur Kuo, Ruey-Jer Weng, Weng-Sing Hwang Effects of Solid Fraction on the Heat Transfer Coefficient at the Casting/Mold Interface for Permanent Mold Casting of AZ91D Magnesium Alloy Materials Transactions, Vol. 47, No. 10 (2006) pp. 2547 to 2554, The Japan Institute of Metals
- [12] Alloy Kuo J H, Hsu F L, Hwang W S, Yeh J L, Chen S J Effects of Mold Coating and Mold Material on the Heat Transfer Coefficient at the Casting / Mold Interface for Permanent Mold Casting of A356 Aluminum Transactions of American Foundry Society, Volume 109, Pp 1-17, 2001
- [13] Pedram Mehraram, Measuring Heat Transfer during Twin Roll Casting of Metals, A thesis presented to the University of Waterloo in fulfillment of the thesis requirement for the degree of Master of Applied Science in Mechanical Engineering Waterloo, Ontario, Canada, 2010, pp. 115
- [14] Pehlke R.D., John M. Cookson, Shouwei Hao , Prasad Krishna, Kevin T. Bilkey: Heat Transfer at the Mold - Metal Interface in Permanent Mold Casting of Aluminum Alloys Project Final Report Department of Materials Science and Engineering The University of Michigan Ann Arbor, MI 48109-2136 December 14,2001 Prepared for THE U.S. DEPARTMENT OF ENERGY AWARD NO. DE-FC07-97ID13559
- [15] Mirela Popescu, Bela Varga: Structures of Aluminium Base Alloys Solidified by Vibrations, in Advanced Materials Research, vol. 1128, Advanced Technologies of Materials Processing, 2015, pp. 88-97.

NATURAL GAS CONSUMPTION REDUCING IN ALUMINUM MELTING FURNACES BY HEAT RECOVERY OF FLUE

Vasile BRATU, Aurel GABA, Elena Valentina STOIAN, Florina Violeta ANGHELINA

Valahia University of Targoviste, Faculty of Materials Engineering and Mechanics, Str. Aleea Sinaia, No. 13, Targoviste, Romania

E-mail: v_bratu22@yahoo.com, aurel_gaba@yahoo.com, elenastoian22@gmail.com, vianghelina@yahoo.com

Abstract. *This article presents different solutions to reduce natural gas consumptions of the aluminum melting furnaces, through recovery of the heat from flue gases. In order to be able to analyze the recovery solutions, a mathematical model for energy balance of these furnaces was adapted. This mathematical model allows drawing up energy balances together with the main working technique and economical parameters of these types of furnaces, in actual conditions, and the same, under optimizing conditions, by applying recovery solutions.*

The mathematical model which can elaborate energy balances for aluminum melting furnaces, was transposed in M. Excel based software, where the quantification of different solutions for natural gas consumption saving is possible. One of the applications of this computer software for an aluminum melting furnace, either for actual working conditions or per upgraded furnace by use an air pre-heater, materials pre-heater, or a regenerative burner system, is presented in this article.

Keywords: *recovery, heat, flue gases, aluminum melting furnace*

1 INTRODUCTION

Aluminum melting furnaces are the greatest consumers of natural gas and they represent over 75% from the total energy consumed in the secondary aluminum industry [1].

For most aluminum melting furnaces their thermal efficiency is around 23% (26.3%-27.5%) whilst the heat included in flue gases arise at the level of (50..70)% [1], (55.6%-62.5)%, [2].

Recovering the heat contented in flue gases output from aluminum melting furnaces, is performed nowadays by the heat transfer to the air combustion intended for gas burners use, or by preheating aluminum scrap cold charge.

Preheat combustion air is performed by using a radiation air pre-heater, convection air pre-heater or in the other applications, by regenerative burner system. Preheating radiation air used in this furnaces are usually Schack type, built from two concentric tubes columns, with flow waste gases inside the tube and flow combustion air between the tubes, in forward flow. The co-current flow is preferred because of very high temperature of the waste gases, usually more than 1000 °C. North American Manufacturing Company and Bloom Engineering Inc. mentioned that a typical aluminum melting furnace discharges flue gases in temperature range of 982-1204°C [1].

The co-current flow keeps the refractory steel inner tube under lower temperature, which means a major lifetime for that tube as well as a lower air combustion temperature e.g. approx. 7-8 % less resulting thus a smaller recover efficiency than in the case of to the counter-current flow stage [3,4,5].

Convection air pre-heaters used to this furnaces, are usually cross-flow type, with vertical tubes between air chambers and with flue gases flowing among the tubes, upright on these [1].

Recovery of heat contented in flue gases, from the aluminum melting furnace using radiation and convection pre-heaters, lead to saving energy (natural gas) up to 30% [1].

Due to the exhausting high temperature of the flue gas (over 1000°C), and to the resulting compounds from adding fluxing agents (fluorine, chlorine, etc.) used in melting process, or from the oxidation of aluminum or magnesium based components which have been transferred in flue gases, the lifetime of metallic heat exchangers is very short [1]. Because of the extremely corrosive flue gases environments in this industry, the few metal heat exchangers in service must be maintained at low tube wall temperatures, typically < 540 °C, to control hot corrosion and tube wall recession rates within reason. Consequently, even through flue gases temperatures range normally between 1100 and 1315 °C, the preheated combustion air provided by these metallic heat exchangers is relatively low in temperature, only 315 to 425 °C [6].

Therefore, there have been developed research studies on the substitution of the refractory steel by ceramic materials, and there were manufactured some heat recuperators by using silicon carbide. This type of heat recuperator made of Field tubes module, has been tested and the air combustion temperature reached 815 °C, at a waste gases temperature of 1205 °C [6]. Thus, the use of ceramic material air pre-heaters lead to natural gas energy saving in aluminum melting furnaces up to 40 % [6]. Nevertheless, these ceramics heat exchangers still

have issues of mechanical sealing and mechanical or thermal shock resistance. Also, like metallic heat exchangers, ceramics recoveries are very expensive.

Regenerative burners, whose principle scheme is shown in figure 1, are used in melting furnaces for more than 10 years. In North America alone there are over 80 such furnaces (operational ones) resulting an energy saving of the used fuels up to 50..60 % [7].

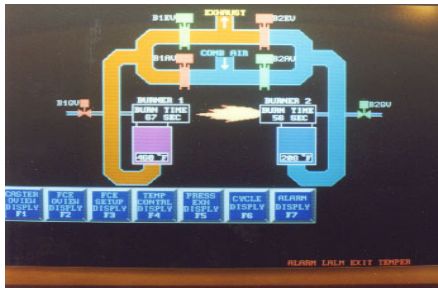


Fig.1. View of Control Display for Regenerative Burner in service, with burner 2 in combustion and burner 1 in discharge of flue gases

The general trend is to use regenerative burners since most customers use some type of fluxing or variable quality scrap that causes problems in use recuperators [1]. Heat recovery contained in flue gases from aluminum melting furnaces is reached, in some cases from Europe, China, Japan, etc., by charge preheating either in separate heaters or in furnaces extension, prior to charge loading in the furnace thus resulting an energy (natural gas) saving up to 20-35 % [1].

The variety of the heat recovery solutions contained by flue gases from aluminum melting furnaces could be divided as follows:

- usage of radiation and convection air metallic pre-heaters, lead to energy (natural gas) saving up to 30 %;
- usage of convection air pre-heaters made of ceramic materials, lead to energy (natural gas) saving up to 40 %;
- usage of regenerative burner system, lead to energy (natural gas) saving up to 50 – 60 %;
- usage of preliminary heating devices for cold metal charge, lead to energy (natural gas) saving up to 20-35 % .

This diversity of the aluminum melting furnace modernization solutions requires a specific analysis of their application for each type of furnace separately.

This analysis, which entails a multitude of steps, for boilers and furnaces modernization, was named the energy diagnosis [8].

The first step of the energy diagnosis is an audit of the boiler or furnace for which constructive and functional data are known. This audit takes into account the real (actual functional data) and optimal (future functional data for boiler or furnace operation with modernization solutions) energy balance. The mathematical model which can perform this audit was translated in Fortran [9] and then in Microsoft Excel programming and was adapted for various boilers and furnaces types:

- steam boiler;
- hot water boiler;

- rotary kiln;
- ladle dry-pre-heater stand;
- melting furnace;
- heating furnace;
- treatment furnace;
- fired heater [8,10].

The second step of the energy diagnosis is a computation of new installations designed parameters can be achieved by simulating the boiler or furnace operation with specific mathematical models [5,11,12,13]. The book [5] describes the original mathematical models used to simulate the operation in a boiler or furnace endowed with a new installation.

The third step of the energy diagnosis is a choosing of new installation optimal variant. The new installation constructive variants (combustion air pre-heaters, super-heaters, economizers, etc.) can be designed with the original mathematical model which was translated in C++ computer program [5].

The first step of the energy diagnosis for an aluminum melting furnace will be explained in this paper. It consists in an audit of the aluminum melting furnace, i.e. the energy balances in actual conditions and under optimizing conditions by applying the heat recovery solutions of flue gases. These energy balances are made by applying the mathematical model described in [8].

The mathematical model which can perform this audit for the aluminum melting furnace was translated in Microsoft Excel programming, making possible the quantification of different solutions for reducing the natural gas consumption by heat recovery of flue gases.

2 EXPERIMENTAL

The aluminum melting furnace is a furnace which has a discontinuous operating process, working in charges. One charge has a capacity up to 60t (up to 50t solid aluminum scrap and another part, of molten aluminum, up to 30t). The charge is loaded through the front part of the furnace by a moto-charger, into the free space left by the swung door. A view of such a melting furnace is shown in figure 2.



Fig.2 View from the swing filling door of an aluminum melting furnace

Discharge of a molten aluminum charge, is made by revolving the furnace to the back, by discharging molten

aluminum on discharge hole, located in the rear wall side and over the level of aluminum molten bath (in horizontal position).

The effective dimensions of the furnace are:

- length = 8m;
- width heart = 6,7 m;
- high = 3 m.

Working process is discontinuous, in cycles of up to 6 hours, depending on the solid charge weight. Maximal temperature inside the furnace is about 1200°C. The furnace is made of the followings main parts:

- structural steel;
- refractory and insulated brick walls;
- burning system and gas exhausting devices;
- revolving door device and rotation device of furnace.

The steel structure of the furnace assures and sustains all others components of the furnace, and it is made of profiles and metallic sheet plate. The inside brick wall is a body which defines the working space of a furnace. The refractory bricking is part of hearth, wall, arch. The refractory bricking part will assure:

- high temperature strength;
- resistance to corrosive inner agents;
- outside bricking heat insulation;
- reduction of heat loss to the outer environment.

The furnace walls and the hearth have a refractory thickness of 250 mm and thermo-insulated wall of 100 mm. The arch have the thickness of the refractory wall of 180 mm and thermo-insulated wall of 120 mm. Burning system have as main functions:

- assure the directions and flow velocity for all burning components (natural gas and combustion air);
- develop the conditions to prepare burner steady state (good mixing for all components);
- insert the mixing compounds in burning space;
- flame stabilization;
- assure flame parameters stated by characteristics of thermo-technological process.

Burner system of aluminum melting furnace contains 4 burners with nominal power heat of 2500 [kW] each. The burners are located in pairs on the two lateral walls with jet directed down onto the hearth. The burners has the flow rate of 250 [m³N/h] and use as fuel natural gas with calorific power Hi=35570 [kJ/ m³N]. Burner system of a furnace is feed by a single fan with air flow of 11000 [m³N/h].

Actual energy balance was performed taking into account the measurement values for main working parameters. Because the aluminum melting furnace works with different mass range, Rm (Rm=weight solid charge / weight of melted aluminum charge) some of the parameters were adopted to be within one group of the followings:

-Rm =5 (50 t weight of charge solid aluminum scrap / 10 t weight of melted aluminum charge); Wsc=50 t/charge; lifetime is 6 hours;

-Rm = 2 (40 t weight of charge solid aluminum scrap /20 t weight of melted aluminum charge); Wsc= 40 t/charge ; lifetime is 5 hours;

-Rm = 1 (30 t weight of charge solid aluminum scrap /30 t weight of melted aluminum charge); Wsc= 30 t/ charge; lifetime is 4 hours.

The physical heat of a charge depends on the weight of melted bath, therefore outlet heat values are found separately in sensible heat of the secondary product.

For each of the 3 above group where considered:

- the same average temperature for refractory wall-parts;
- the same average temperature for insulated wall parts;
- the same average temperature on external wall of furnace;
- the same average temperature of flue gases = 1093 °C;
- the same amount of slag = 2%Wsc;
- the output heat delivery with airborne dust was neglected.

In table 1 and 2, there are contained the components of actual energy balance of the furnace (table 1=input heats, table 2=output heats), where the following definitions are used:

- Q₁ – chemical heat of the fuel;
- Q₂- sensible heat of the fuel;
- Q₃- physical heat of a charge;
- Q₅- total heat of the combustion air;
- Q₆- outlet heat from heat generation reaction;
- Q_{int}- sum of inlet heats;
- Q₁₀- sensible heat of a main product at the furnace outlet;
- Q₁₁-heat lost trough wall and hearth;
- Q₁₃- radiation heat over unsealing spaces;
- Q₁₄- heat of flue gases;
- Q₁₇- sensible heat of a secondary product at the furnace outlet;
- Q₂₂-accumulated heat inside the wall furnace;
- Q₂₃- sensible heat of slag;
- Q_{ies}- sum of outlet heats;
- Q_{er}- balance error.

Table 1. Compound of actual heat balance-inlet heats

Symbol	Values for Rm =5		Values for Rm =2		Values for Rm =1	
	[kJ/t]	[%]	[kJ/t]	[%]	[kJ/t]	[%]
Q ₁	3629847.0	93.19	377050.3.4	86.53	3986782.7	77.89
Q ₂	3328.4	0.08	3353.5	0.08	3545.9	0.07
Q ₃	231968.3	5.95	552121.1	12.67	1094975.0	21.39
Q ₅	26960.4	0.69	28005.1	0.64	29611.5	0.58
Q ₆	3441.9	0.09	3441.9	0.08	3441.9	0.07
Q _{int}	3895446.0	100.00	435742.5.0	100.00	5118357.0	100.00

Table 2 Compound of actual heat balance-outlet heats

Symbol	Values for Rm =5		Values for Rm =2		Values for Rm =1	
	[kJ/t]	[%]	[kJ/t]	[%]	[kJ/t]	[%]
	Q ₁₀	148567.5	38.14	148567.5	34.10	148567.5
Q ₁₁	55750.5	1.43	58073.5	1.33	61945.0	1.21
Q ₁₃	5098.4	0.13	6372.9	0.15	8497.3	0.17
Q ₁₄	195221.7	50.12	20278.6	46.54	21441.8	41.89
Q ₁₇	230602.0	5.92	57650.1	13.23	11530.0	22.53
Q ₂₂	146466.1	3.76	18308.2	4.20	24411.0	4.77
Q ₂₃	18828.5	0.48	18828.5	0.43	18828.5	0.37
Q _{er}	808.5	0.02	1021.9	0.02	2105.2	0.04
Q _{res}	389544.6	100.00	43574.2	100.0	51183.0	100.00

A capture from Excel programming of the actual energy balance for Rm=2, for this aluminum melting furnace, is shown in figure 3.

Fig. 3 The capture from Excel programming of the actual energy balance for Rm=2

3 RESULTS AND DISCUSSIONS

Optimized heat balance, is obtained when the working process from the furnace is simulated with different solutions of heat recovery from flue gases, and permits the quantization of reducing the amounts of natural gas, used in aluminum melting furnace.

In tables 3 and 4, compounds of optimized heat balance of furnace are presented (table 3=inlet heats; table 4=outlet heats), in conditions of simulated working furnace, in Rm=5 state, with each of all 3 recovery solution of flue gases:

- the furnace with recovery device for preheat air combustion up to = 480°C, Typ rec.= PA;
- the furnace with regenerative burner system for preheat air combustion up to = 800°C, Typ rec.= RB;
- the furnace with preheating solid aluminum charge up to = 400°C, Typ rec.= PC.

Table 3 Compounds of optimized heat balance-input heats

Symbol	Values for PA		Values for RB		Values for PC	
	[kJ/t]	[%]	[kJ/t]	[%]	[kJ/t]	[%]
	Q ₁	2642529.0	78.52	2192428.0	70.20	2845800.0
Q ₂	2350.3	7.0	1949.9	6.0	2531.1	7.0
Q ₃	231968.6	6.89	231968.3	7.43	601188.0	17.31
Q ₅	485440.2	14.42	693250.6	22.20	21069.0	0.61
Q ₆	3441.9	0.10	3441.9	1.01	3441.9	0.10
Q _{int}	3365730.0	100.00	3123039.0	100.00	3474030.0	100.00

Table 4 Compounds of optimized heat balance output heats

Symbol	Values for PA		Values for RB		Values for PC	
	[kJ/t]	[%]	[kJ/t]	[%]	[kJ/t]	[%]
	Q ₁₀	148567.5	44.14	148567.5	47.57	148567.5
Q ₁₁	55750.5	1.66	55750.5	1.79	55750.5	1.60
Q ₁₃	5098.4	0.15	5098.4	0.16	5098.4	0.15
Q ₁₄	142121.4	42.23	117913.9	37.76	153053.8	44.06
Q ₁₇	230602.0	6.85	230602.0	7.38	230602.0	6.64
Q ₂₂	146466.1	4.35	146466.1	4.69	146466.1	4.22
Q ₂₃	18828.5	0.56	18828.5	0.60	18828.5	0.54
Q _{er}	2095.3	0.06	1479.1	0.05	1071.3	0.03
Q _{res}	336573.0	100.00	312303.9	100.00	347403.0	100.00

A capture from Excel programming of the optimized energy balance for Rm=2, for this aluminum melting furnace, endowed with recovery heat exchanger for preheat combustion air up to 480 °C, is shown in figure 4.

Fig.4 The capture from Excel programming of the optimized energy balance for Rm=2

With data extracted from Excel Programming, in conditions of simulation working conditions of the furnace, in all stages (Rm=5, Rm=2, Rm=1), and taking into account all 3 solutions for recovery the heat from flue gases, it is possible to calculate the decreasing

quantities of natural gas, respectively the gain of thermal efficiency. The thermal efficiency was defined as the ratio between heat contained by the main product and the heat brought by the burning of the natural gas.

In diagram from figure 5, it is shown the quantities of natural gas, Q , used by initial furnace (without recovery, Typ rec.= WR), and quantities of natural gas used by furnace fitted with recovery system.

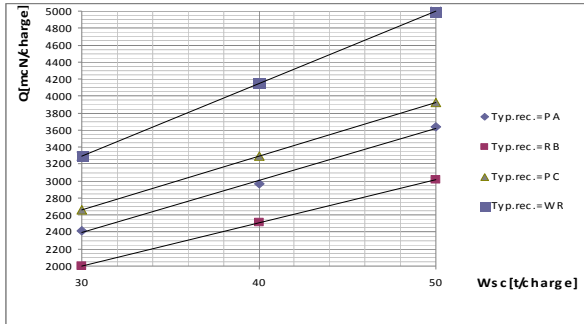


Fig.5 Consuming of natural gas for furnace Q, in term of weight solid charge, Wsc, and recovery flue gas heat type

Thus, in the case of recovery with preheating air combustion up to 480°C, consumption of natural gas was reduced with about 27-28 %, for all working state (28.6% [14] and respectively 30% [1]);

- in the case of recovery with regenerative burner system air combustion up to 800 °C, consumption of natural gas was reduced with about 39 %, for all working state (40% [1]);

- in the case of use recovery for preheating solid aluminum charge up to 400 °C, consumption of natural gas was reduced with 19.3 %, for working state $R_m = 1$, reduced up to 21.6 %, for working state $R_m = 5$ (20%-35% [1] and respectively 18.9% [15]).

In diagram from figure 6, it is shown thermal efficiency, E_f , obtained by initial furnace (without recovery), and thermal efficiency obtained by furnace fitted with recovery system.

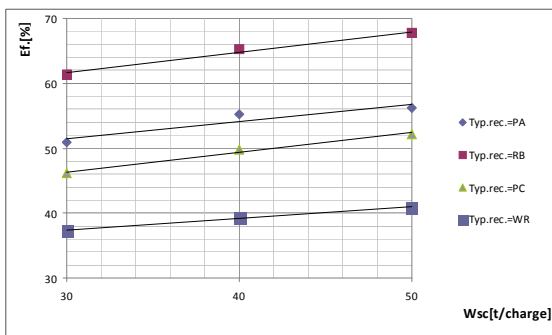


Fig.6 Thermal efficiency, E_f in term of weight solid charge, Wsc, and recovery flue gas heat type

Thus, in the case of aluminum melting furnace in service, leads to the following values for thermal efficiency:

- 37.26 %, for working state $R_m = 1$;
- 39.40 %, for working state $R_m = 2$;
- 40.93 %, for working state $R_m = 5$.

These values are very close to the values presented in some specific books, regarding the actual energy efficiency of the aluminum melting furnaces proposed to be upgraded by recovery, within the range of 20-45 % [16], 32% [7], 30-35% [17] and respectively 30-45 % [18].

Applying this design program on the same aluminum melting furnace, under optimized service, is simulated in an working furnace with different recovery solutions and the following values of thermal efficiency were obtained:

- 50.95 % (for working state $R_m = 1$) up to 56.22 % (for working state $R_m = 5$), in the case of recovery with preheating air combustion up to 480°C (a high efficiency recuperator can offer a thermal efficiency up to 49-55% and deliver preheated air at about 500-537 °C) [1,7];
- 61.39 % (for working state $R_m = 1$) up to 67.76 % (for working state $R_m = 5$), in the case of recovery with regenerative burner system air combustion up to 800°C (a high efficiency regenerative burner system can offer a thermal efficiency up to 71% and deliver preheated air up to 1130 °C) [7];
- 46.16 % (for working state $R_m = 1$) up to 52.20 % (for working state $R_m = 5$), in the case of use recovery for preheating solid aluminum charge up to 400 °C (a company reports a thermal efficiency of 43% [19].

4 CONCLUSIONS

The variety of the heat recovery solutions contained in flue gases from aluminum melting furnaces, are as following:

- use of radiation or convection metallic pre-heaters for air combustion;
- use of air pre-heater from ceramics materials;
- use of regenerative burner system;
- use of pre-heaters for solid aluminum charge.

This diversity leads to an exhaustive analysis of these applications, for each furnace.

The first step of this analysis, named energy diagnosis, was presented in this article and was explained by application of mathematical model with designing of energy balance, for aluminum melting furnaces, transposed in a Excel programming. Applying this computer program, in the melting furnace in service, leads to the following values for thermal efficiency:

- 37.26 %, for working state $R_m = 1$;
- 39.40 %, for working state $R_m = 2$;
- 40.93 %, for working state $R_m = 5$.

These values are very close to the values presented in some specific books, regarding the actual energy efficiency of the aluminum melting furnaces proposed to be upgraded by recovery, within the range of 20-45 % [16], 32% [7], 30-35% [17] and respectively 30-45 % [18].

Applying this computer program on the same aluminum melting furnace, under optimized service, is simulated in an working furnace with different recovery solutions and the following values of thermal efficiency were obtained:

- 50.95 % (for working state $R_m = 1$) up to 56.22 % (for working state $R_m = 5$), in the case of recovery with preheating air combustion up to 480 °C (a high efficiency heat exchanger can offer a thermal efficiency up to 49-55% and deliver preheated air at about 500-537 °C) [1,7];
- 61.39 % (for working state $R_m = 1$) up to 67.76 % (for working state $R_m = 5$), in the case of recovery with regenerative burner system air combustion up to 800 °C (a high efficiency regenerative burner system can offer a thermal efficiency up to 71% and deliver preheated air up to 1130 °C) [7];
- 46.16 % (for working state $R_m = 1$) up to 52.20 % (for working state $R_m = 5$), in the case of use recovery for preheating solid aluminum charge up to 400 °C (a company reports a thermal efficiency of 43% [19]).

In the same time, by applying the computer program, the quantification of a reduction of the natural gas consumption was obtained.

- Thus, in the case of recovery with preheating air combustion up to 480 °C, consumption of natural gas was reduced with about 27-28 %, for all working state (28.6% in [14] and 30% in [1]);
- in the case of recovery with regenerative burner system air combustion up to 800 °C, consumption of natural gas was reduced with about 39 %, for all working state (40% in [1]);
- in the case of use recovery for preheating solid aluminum charge up to 400 °C, consumption of natural gas was reduced with 19.3 %, for working state $R_m = 1$, reduced up to 21.6 %, for working state $R_m = 5$ (20%-35% in [1] and 18.9% in [15]).

Quantification of natural gas reduced consumption by applying the mathematical model for energy balances, justifies this first step of the energy diagnosis of the aluminum melting furnace modernization by heat recovery contented in flue gases.

For adopting a right decision for the aluminum melting furnace modernization, this analysis will be continued with a study for each type of recovery solution.

The numerous construction possibilities of the metallic convection pre-heater have been analyzed, by sizing them, by means of the C++ computer program [5].

5 REFERENCES

Journals:

- [1] Gorog, P., Improved materials and operation of recuperators for aluminum melting furnaces, DE-FC36-04GO14035, sept.2007, <http://www.ornl.gov/sci/ees/itp/documents/FnIRptRecuperatorsFinal.pdf>.
- [2] Subodh, K.D., Aluminum melting furnace design optimization to improving energy efficiency by integrated modeling, University of Kentucky, july 2008, http://www.phinix.net/services/Energy_Management/Aluminum_Melting_Furnace.pdf.

- [4] Heiligenstaedt, W., Thermique appliques aux fours industriels, Dunod, Paris 1971.
- [6] Ward, M.E. a.a., Application of a new ceramic recuperator technology for use on an aluminum remelt furnace, Gas Warne International, 37, nr. 3, 1988, p. 144.
- [7] Schalles, D.G., The next generation of combustion technology for aluminum melting, <http://www.bloomeng.com/aluminum-studies.html>.
- [9] Gaba, A., Valceanu, S., Analysis using a mathematical model of heat balance heating furnaces, Metallurgical Research (Bucharest) 18, 1977, p. 333-338.
- [11] Murza, S., Henning, B., Jasper, H.D., CFD simulation of melting furnaces for secondary aluminum, Heat processing, nr.2, 2007, p.122-126.
- [12] Pisa, L., Prisecaru, T., Negreanu, G., Researches on the renewable fuels gas production and their economical and ecological utilization, Rev. Chim. (Bucharest) 59, nr.1, 2008, p.97-100.
- [13] Sacadura, J.F., Initiations aux transferts thermiques, Technique et Documentation, Paris 1980.
- [14] U.S Department of Energy, Efficient process heating in aluminum industry, <http://www1.eere.energy.gov/manufacturing/resources/aluminum/pdfs>.
- [15] Southern California Gas Company, Industrial furnace energy efficiency, B-RP-06-599-13, april 2006. <http://www.socalgas.com/.../Furnace%20&%20Ovens%20WP%20>.
- [16] U.S Department of Energy, Improving energy efficiency in aluminum melting, <http://www1.eere.energy.gov/manufacturing/resources/aluminum/pdfs>
- [17] Schwam, D., Melting efficiency in Die casting operations, DE-FC36-04GO14230, dec.2012, http://www.esmarrt.org/final%20reports/Task2.1_Melting_Efficiency_in_Die_Casting_Operations.pdf
- [18] ITP Metal Casting, Advanced melting technologies : Energy saving concepts and opportunities for the metal casting industry, nov. 2005, <http://www1.eere.energy.gov/manufacturing/resources/metacasting/pdfs/advancedmeltingtechnologies.pdf>
- [19] Subodh, K.D., Improving energy efficiency in aluminum melting, DE-FC07-01ID14023, april 2007, http://www.phinix.net/services/Energy_Management/Improving_Energy_Efficiency.pdf

Books:

- [3] Schack, A., Industrial heat transfer, Chapman and Hall, London 1965.
- [4] Heiligenstaedt, W., Thermique appliques aux fours industriels, Dunod, Paris 1971.
- [5] Gaba, A., Heat transfer in industrial installations, Publishing Bibliotheca, Targoviste 2004, p.295, ISBN 973-8413-42-7.
- [8] Gaba, A., Boilers and furnaces modernization, Valahia University Press, Targoviste 2013, p. 345, ISBN 978-606-603-076-2.
- [10] Gaba, A., Valceanu, S., Catangiu, A., Paunescu, L., Energy audit in metallurgy, Publishing Bibliotheca, Targoviste, 2003, p. 248, ISBN 973-8413-41-9.

ROLE OF SUPERPLASTICIZER ADDITIVES UPON HYDRATION PROCESS OF CEMENT PASTES

Nicolae ANGELESCU ¹, Darius STANCIU ¹, José BARROSO DE AGUIAR ²,
Hakim S. ABDELGADER ³, Vasile BRATU ¹

¹ Valahia University of Targoviste, Romania

² Minho University, Guimaraés, Portugal

³ Tripoli University, Tripoli, Libya

E-mail: nicolae.angelescu@yahoo.com

Abstract. The article presents a comparative analysis on the hydration of cement paste without superplasticizer and water/cement ratio of 0.35 and a cement paste with the same water /cement ratio but has in its composition 2% superplasticizer additive Glenium Sky 526. For characterizing the hydration process of cement paste, both mixtures were subjected to X-ray diffraction and thermogravimetry analysis, at 3, 7, and 28 days passed since the initiation of hydration process.

Keywords: portland cement, superplasticizer additive, X-ray diffraction, termogravimetry

1. INTRODUCTION

Coagulation structures that occur in the curing / hydration process of Portland cement binders, are of great importance in implementing technologies in the work of Portland cement based products. Based on coagulation structures develop crystallization structures and condensation-crystallization structures with different properties, their occurrence as a consequence of hydration-hydrolysis processes of mineralogical constituents passing into stable hydration systems.

The present of superplasticizers additives can alter the kinetics of hydration than by changing curing time and the occurrence of specific hydration products at different time intervals [1].

2. MATERIALS USED AND EXPERIMENTAL WORKS

2.1. Superplasticizers

In present study are used two types of polycarboxylate based superplasticizer, more exactly polycarboxylate ether admixtures/additives. First used is the superplasticizer known as Glenium Sky 526. For this superplasticizer additive the technical data and the chemistry are presented also in table 1 [2].

2.2. The cement

Cement paste mixtures were prepared with a CEM I 42.5R type cement with Blaine specific surface area of 380 m²/kg and specific gravity of 3.12. The same

cement was also used in concrete mixtures. Oxide composition of the cement is shown in table 2.

Table 1 Technical data and chemistry for Glenium Sky 526

Superplasticizer type	Glenium Sky 526
Relativ density (20°C):	1,07 ± 0,02 g/cm ³
Viscosity (20°C):	< 100 cps
Alkali content	≤ 2.5 % (EN 934-1 / 2008)

Table 2 The chemical properties of cement (CEM I 42.5 R)

Oxide (%)	SiO ₂	Al ₂ O ₃	Fe ₂ O ₃	CaO	MgO	Na ₂ O	K ₂ O	SO ₃	Cl	L.O.I
Cement	19.30	5.57	3.46	63.56	0.86	0.13	0.80	2.91	0.013	2.78

3 . RESULTS AND INTERPRETATION OF EXPERIMENTAL WORKS

3.1. Analysis by X-ray diffraction

There were determined the mineralogical compounds of Portland cement (cement paste prepared with a water/cement ratio of 0.35 and without superplasticizer), such as alite, belite and celite, and CaO, the compounds of the blast-furnace slag, admixture of cement (SiO₂, Al₃Fe₅O₁₂, Al₃FeSi, Ca₃Al₂Si₃O₁₂), and hydration products Ca₆Si₂O₇SiO₄ (OH)₂, which is a type CSH and portlandite Ca(OH)₂ (figure1). Following roentgenographic

spectrum in figure 1 a, b and c, it can be seen that with increasing hydration period from 3, 7 and then at 28 days, the alite spectral lines decrease in intensity. This phenomenon proves that the alite after hydration turns into CSH, even if they are not very well highlighted in figure 1 b and c. CSH can be seen only by X-ray diffraction analysis in simple cement paste at 3 days of hydration. The difficulties of highlighting the CSH hydration product in simple cement paste at periods of 7 and 28 days, is because this product is not well crystallized, being in the form of gel, which makes hard to identify it, in the X-ray spectrum [1, 3- 5].

X-ray diffraction analysis carried out on a sample of cement paste with 2% additive Glenium Sky 526, at 3, 7 and 28 days highlighted the presence of mineralogical and hydration products - also determined on simple cement paste, supplementary one more compound, $\text{CaFe}+2\text{SiO}_4$, originated probably from the addition of blast-furnace slag used in the preparation of portland cement (figure 2).

Following the results of X-ray diffraction analysis for both normal and additivated cement pastes, it can be seen that the spectral intensities reveals that alite hydration process occurs similarly from 3 to 7 days in both mixtures and from 7 to 28 days, more intense hydration process occurs in the mixture with 2% additive Glenium Sky 526, as evidenced by the reduced spectral intensities of alite (figure 2 c), in comparison with the simple cement paste (figure 1 c) [3 - 5].

3.2. Thermogravimetric analysis of cement pastes

For the samples without superplasticizers additive there were 3 temperature intervals where there were mass losses. Interval I ($50^\circ - 200^\circ \text{C}$), the maximum effect of this mass loss occurs at the minimum of the DTG curve at 127.2°C , denoted by A on the curve, this loss being 6.07% (point 1 – figure 3 a) at 3 days of hydration. At 7 days the mass loss was 7.31% (1) at a temperature of 125.1°C (point A, figure 3 b), and at 28 days (Fig. 3 c) a loss of mass was 10.89% with a maximum at 145.5°C . In this temperature interval the mass loss was due to the elimination of free water.

On the interval II ($420^\circ - 520^\circ \text{C}$) the mass loss was recorded only at 28 days, 3.15% (point 2) with a maximum temperature of 486.5°C , mass loss due to dehydration of calcium hidrosilicates and, possible, hydrosulphite aluminate phases.

The third interval ($700^\circ - 800^\circ \text{C}$) had a mass losses of 14.27% (2) with a temperature maximum at 822.9°C (B) at 3 days. At 7 days the mass losses was 16.26% at 825.2°C and after 28 days the mass losses were 9.65% (3) at a temperature of 836.5°C . The mass loss on interval III are due to the elimination of the chemically bound water of hydration products of the cement, such as calcium hidrosilicates CSH (type II) in crystalline form [6 - 10].

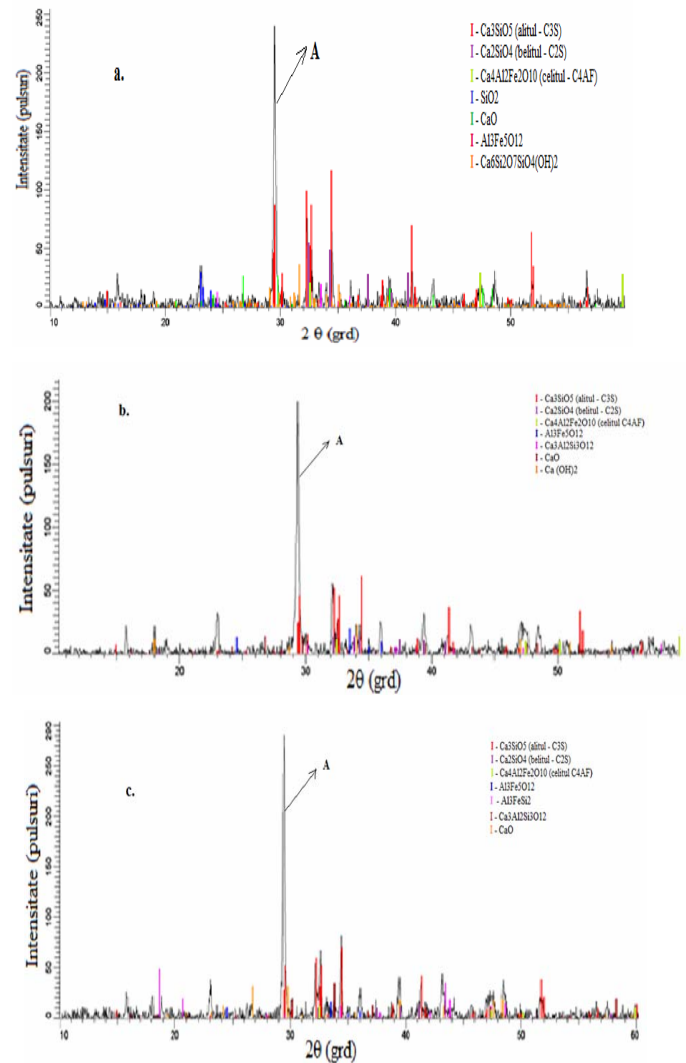


Fig. 1. X-ray diffraction spector of simple cement paste, without superplasticizer additive: a. at 3 days of hydration, b. 7 days of hydration; c. 28 days of hydration

In the case of cement paste with 2% superplasticizer additive Glenium Sky 526, the mass losses interval I ($50^\circ - 200^\circ \text{C}$), at 3 days was 9.31% with a maximum at 134.9°C . At 7 days there was a mass loss of 8.98% with a maximum at 136.5°C and at 28 days there was a mass loss of 10.56% with a maximum at 134.7°C (figure 4).

In second interval II ($420^\circ - 520^\circ \text{C}$) were recorded at 3 days a mass losses of 1.76%, with a maximum at 475.8°C (figure 4 a), at 7 days the mass losses was 1.65 % at a temperature of 479.3°C (figure 4 b), and at 28 days the mass losses was 2.56% with a maximum at 479.3°C (figure 4 c).

On interval III ($700^\circ - 800^\circ \text{C}$), mass losses were 11.09% with a maximum at 833.4°C , at 3 days, at 7 days were recorded mass losses of 14.45% within at 838°C and at 28 days the mass losses were of 11.07% with a maximum at 839.1°C [6 - 10].

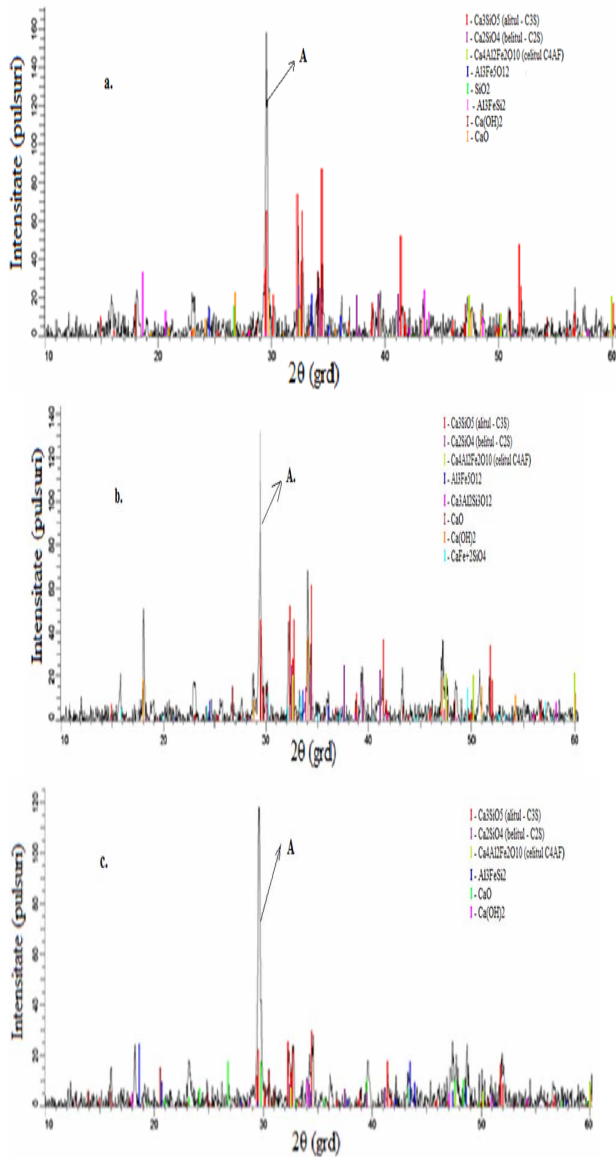


Fig. 2. X-ray diffraction spector of cement paste with 2% superplasticizer additive Glenium Sky 526: a. at 3 days of hydration, b. 7 days of hydration; c. 28 days of hydration

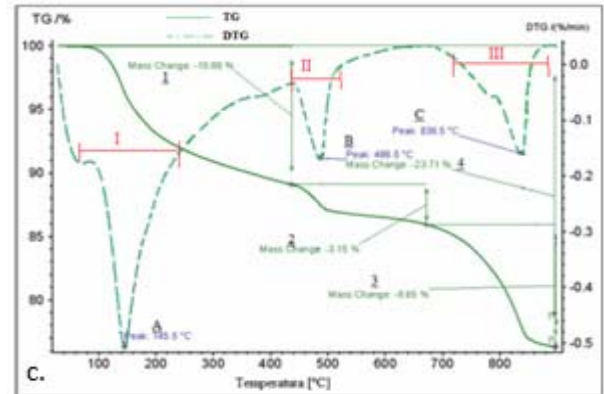
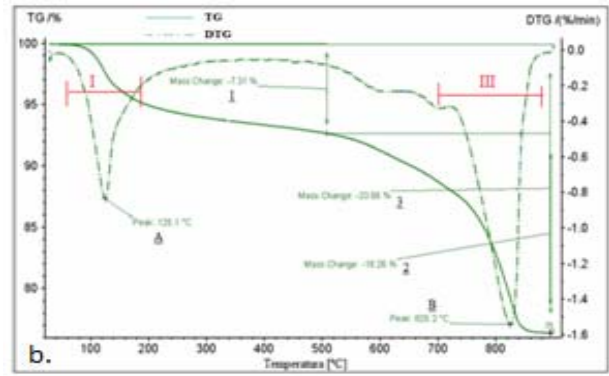
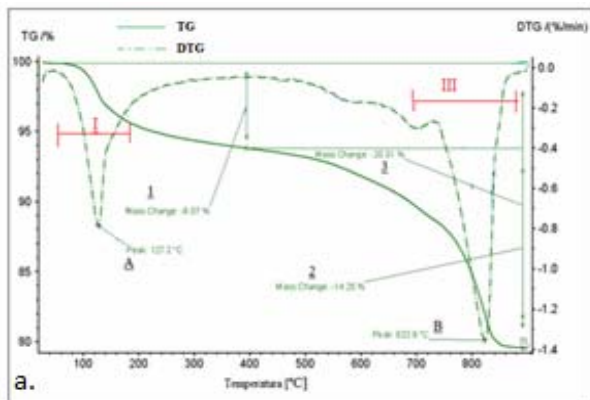
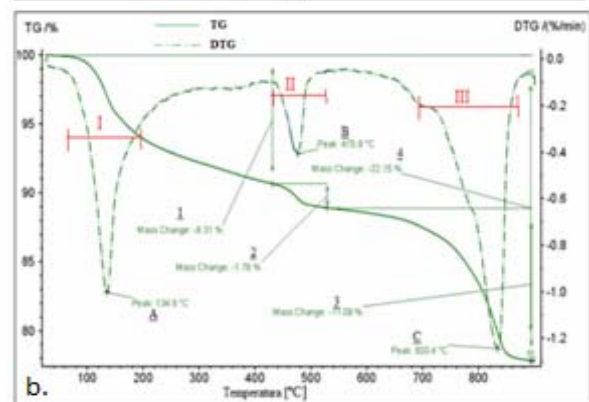
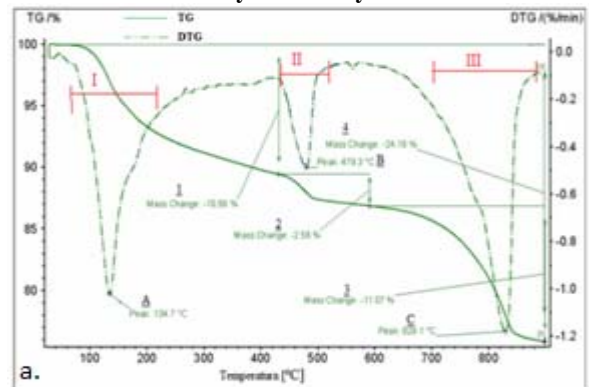


Fig. 3. Thermogravimetric analysis of simple cement paste, without superplasticizer additive, after 3 (a), 7 (b) and 28 (c) hydration days



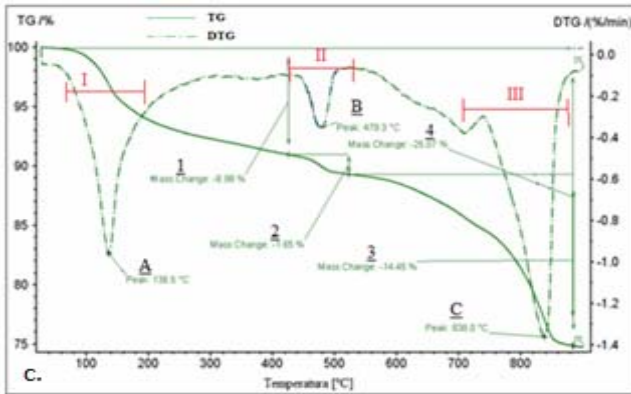


Fig. 4. Thermogravimetric analysis of cement paste with 2% superplasticizer additive Glenium Sky 526, after 3 (a), 7 (b) and 28 (c) hydration days

4. CONCLUSIONS

X-ray diffraction of the sample without additive at 3 days highlighted the hydration product $\text{Ca}_6\text{Si}_2\text{O}_7\text{SiO}_4(\text{OH})_2$ resulting from alite hydration, which is responsible for strength developing.

X-ray diffraction spectra of the sample without additive highlighted the presence of hydration product $\text{Ca}(\text{OH})_2$ at 7 days of hydration.

X-ray diffraction of the sample with the addition of 2% Glenium Sky 526 has detected the presence of $\text{Ca}(\text{OH})_2$ in all the hydration periods (3, 7 and 28 days). So, the Glenium Sky 526 additive favors the development of $\text{Ca}(\text{OH})_2$, which result from the hydration of calcium silicates,

Were revealed 3 temperature intervals where there are mass losses in the case of thermogravimetric analysis.

The smallest mass losses has the simple cement paste, cured at 3 days, 20.31%, while the largest mass losses has cement paste sample, prepared with 2% superplasticizer additive Glenium Sky 526, cured at 3 days, whose value is 25.07%.

It demonstrates the existence of a more important degree of hydration in the cement paste with 2%

Glenium Sky 526 comparing with the simple cement paste sample.

5 REFERENCES

Journals:

- [1] Spiratos, M. M., Page, N., Mailvaganam, V.M. Malhotra, C., Jolicoeur, S. - Superplasticizers for Concrete. Fundamentals, Technology, and Practice, Marquis, Quebec, Canada, 2006.
- [2] *** <http://www.basf.ro/ecp2/Romania/ro/>.
- [3] Moham, I., Vlad, N., Stanciu, G., Fechet, R. - Influenta conditiilor si duratei de pastrare a clincherului si zgurii granulate de furnal asupra caracteristicilor cimentului. Revista Romana de Materiale, 40 (2) 2010.
- [5] Juhuyuk, M., Seyoon Y., Wentzcovitch, R. M., Simon, M. C., Monteiro, P.J.M. - Elastic Properties of Tricalcium Aluminate from High-Pressure, Experiments and First-Principles Calculations. J. Am. Ceram. Soc., 95 (9), 2012.
- [7] Das, S. K., Daspoddar, P. K., - Dehydration kinetics of hydrated calciumdialuminate. Thermochemica Acta, vol 293, no 1, 1997.
- [8] Chotard, T., Gimet-Breart, N., Smith, A., Fargeot, D., Bonnet, J. P., Gault, C. - Application of ultrasonic testing to describe the hydration of calcium aluminate cement at the early age. Cement and Concrete Research, vol 30, no 3, 2001.
- [9] Miklos, R., Wagner, Z. - Determination of the expected decrease in strength of high alumina cement concrete by derivatography. Thermochemica Acta, no 31, 1979.
- [10] Stanciu, D. - Special Concretes with Additives. Doctorate thesis, Valahia University from Targoviste, 2014.

Books:

- [4] Cioara, A., Caluser, S. - Chemistry silicates and technical analysis, Publishing Didactic and pedagogical Bucharest, 1992.
- [6] Moldovan, V. - Additives in concrete, Publishing Technical, Bucharest 1978.

ANALYSIS OF THE COMBUSTION AIR PREHEATER FROM THE ALUMINUM MELTING FURNACES

**Aurel GABA, Vasile BRATU, Dorian MUSAT,
Ileana Nicoleta POPESCU, Maria Cristiana ENESCU**

Valahia University of Targoviste, Faculty of Materials Engineering and Mechanics, Str. Aleea Sinaia, No. 13,
Targoviste, Romania

E-mail: aurel_gaba@yahoo.com, v_bratu22@yahoo.com, pinicoleta24@yahoo.com, cristiana_enescu@yahoo.com

Abstract. *This paper presents solutions and the equipment for preheating combustion air from scrap aluminum melting furnaces through flue gas heat recovery. For sizing convection pre-heaters, there has been developed a mathematical model which has been transcribed into a computer program in C + +. A constructive version of the pre-heater was drawn up and a recovery heat exchanger was manufactured and mounted on an aluminum melting furnace. Both the functional parameters values and the reasons causing the pre-heater working out, as well as the steps taken for sizing and the achievement of a new air pre-heater able to bear the operating conditions of the aluminum melting furnace are shown.*

Keywords: *pre-heater, combustion air, furnace, aluminum scrap*

1 INTRODUCTION

The preheating of the combustion air in the aluminum melting furnaces is generally made by using radiation or convection preheating heat exchangers. It was found that the preheating devices can improve the practical efficiency of aluminum melting furnaces by 4-7% for every 100 °C the combustion air is increased in temperature [1]. Also, preheating devices offer the faster return the investments for preheating combustion air. Customers are realizing a 19-25% reduction in the fuel usage with these heat exchangers and ROIs are averaging 26 months [2]. The newest operational system of using the regenerative burners has several disadvantages: higher costs, greater space for their mantling and additional cost for their maintenance [3, 4]. Radiation air pre-heaters used in these furnaces are generally dr. Schack type. They are made of two concentric tubes where the flue gas flows through the inner tube and the combustion air flows in parallel through the section of the two tubes. The parallel flow is preferred due to the high temperature of the flue gas of over 1000 °C [1,3]. The parallel flow submits the refractory steel inner tube to lower temperatures which means a longer life for it, but this also leads to approx. 7-8%, lower temperatures of combustion air preheating, meaning a lower efficiency of recovery in comparison with the countercurrent flow [3,5,6,7].

The convection air pre-heaters used in these furnaces are usually cross flow type in countercurrent with vertical pipes between the air chambers and flue gas flowing perpendicularly on the tubes [3]. Due to the high temperatures of the flue gas of over 1000 °C, as well as of the components resulted from the flows of fluorine, chlorine based gases, etc., used in the process of scrap melting or from the reactions of the cast aluminum or magnesium oxidation and engaged by the flue gas, the life of the metallic recovery heat exchangers

is extremely short [3]. As a consequence, there are studies to find solutions for improving the metallic convection recovery heat exchangers, as well as for replacing the refractory steel grades with ceramic materials (for instance the recovery heat exchangers made of silicon carbide). Such a recovery device, made of Field tubes modules, has been tested and there has been reached a combustion air preheating temperature of 815 °C, for the exhaust flue gas temperature of 1205 °C [8]. For these ceramic recovery heat exchangers there are still sealing, mechanical strength or thermal shock resistance problems.

Improving the construction solution of the metallic convection pre-heaters could be made on the grounds of an exhaustive analysis of the causes leading to their working out. In the same time, the numerous construction possibilities should be analyzed, by sizing them by means of a computer program [7].

For the convection air pre-heater sizing we use our own computer program. The mathematical model and the calculation algorithm are presented in this paper [7].

The C++ transcribed mathematical model was used for sizing of the air pre-heater required by the Contractor of the modernization of an aluminum melting furnace on the base of the following design parameters:

- recovery heat exchanger type: bundle of tubes performed from refractory AISI 304 steel, outer diameter 76 mm, available;
- maximum natural gas flow: 1000 m³N/h;
- maximum temperature of the flue gas at the recovery heat exchanger entrance: 950 °C;
- maximum temperature of the hot air at the entrance of the burners: 480 °C.

In the same time, the Contractor settled that the combustion air temperature regulation is perform to exhausting into the atmosphere of certain quantity of air from the maximum available flow of 12000 [m³N/h].

Information related to the dust contain of the flue gas were required from the Beneficiary and therefore there has been decided the designing of the recovery heat exchanger with the inner pipes flue gas flow for different thicknesses of the deposition layers. In the same time, while building the entrance and exit chamber of the flue gas, these were endowed with detachable taps for inside cleaning of the pipes. As well, information was required from the Beneficiary of the furnace regarding its working regime, finding that the natural gas flow drops from the maximum value of 1000 [m³N /h], after reaching the preset temperature in the furnace, in order to maintain it at a constant value. As a consequence, after several tens of running it, the cross countercurrent or parallel flow construction option for the pre-heater was chosen (shown in figure 1).

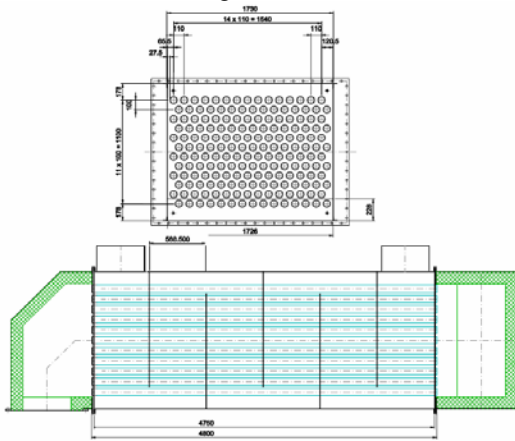


Fig.1 View of the cross countercurrent air flow pre-heater

Simulations of different natural gas flows, different air excess coefficient, on the air and flue gas side, respectively, and of thickness of the deposition layers on the inside of the tubes were undertaken on the same construction option, but with eight countercurrent passes (the length of the tubes is the same in everyone passes), as well as on a mix option of it, with the parallel flow on the first passes and countercurrent on the following ones. Figure 2, shows the chart of the temperature variation of the combustion air preheating, TAE, in [°C], as per the natural gas flow DC in [m³N/h] and the different thickness of the deposition layer, GF, considered 0.0000; 0.0005; 0.0001 and 0.00015 m, if operating with an air excess coefficient of 1.05 at the burners and for the flue gas from the recovery heat exchanger and with a difference of air excess coefficient of 0.1 between the air in the recovery heat exchanger and the one entered the burners, in the case of an eight countercurrent flows passes recovery heat exchanger.

Also, there were calculated the air flows for which the preset maximum temperature at the burners entrance of 480°C is not over passed while considering the temperature loss of 10°C between the pre-heater exit and burners entrance. In the case that the maximum air quantity is exhausted into the atmosphere, with the recovery heat exchanger without deposition layer, GF=0.0000m, the air flows will be of 7911 [m³N /h] instead of 6000 [m³N /h] for the fuel flow of 600 [m³N

/h] and it reaches 11905 [m³N /h] instead of 10000 [m³N /h] for a fuel flow of 1000 [m³N /h]. Thus, a maximum efficiency is reached with an air preheating temperature at the recovery heat exchanger exit in the range of 460-490 [°C], the lower air temperature values are for the maximum fuel flows (DC=1000 m³N /h) and higher depositions (deposition layer GF = 0.0015 m) and the higher values are for the lower fuel flows (DC=600 m³N /h) and without depositions (GF = 0.0000 m).

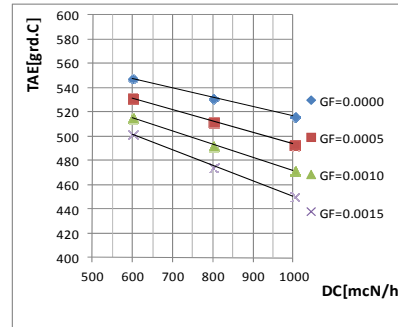


Fig.2 Variation of the combustion air preheating, TAE, in [°C], depending on the natural gas flow, DC, in [m³N /h] and on the thickness of the deposition layer, GF, in m, for the cross countercurrent flow recovery heat exchanger

In the same time, there was calculated that for the cross countercurrent recovery heat exchanger option the temperature of the pipes could reach maximum values of 700°C. As a consequence, in order to drop the temperature of the pipes, trials were made also for the mix flow recovery heat exchanger, with parallel flow in the first passes from the combustion air inlet and cross countercurrent flow in the last passes at the combustion air exit from the recovery heat exchanger.

Figure 3 shows, in the case of the recovery heat exchanger with the first three passages with parallel flow and the following five with countercurrent flow, the preheating temperature variation of the combustion air, TAE, in °C, depending on the natural gas flow, DC, in m³N /h and on the thickness of the deposition layer, GF, considered 0.0000; 0.0005; 0.0001 and 0.00015 m, in the case of an air excess coefficient of 1.05 in the burners and for the combustion air and flue gas in the recovery heat exchanger.

For the cross flow recovery heat exchanger with parallel flow in the first three passes and countercurrent flow for the next five, the temperature of the pipe wall reaches maximum 565 °C, which gives greater safety during a longer operation life against the cross countercurrent recovery heat exchanger.

In the same time, the maximum efficiency is reached through air preheating temperature at the exit of the recovery heat exchanger in the range of 460-490 [°C], as in the case of the cross countercurrent recovery heat exchanger, except when using natural gas flows greater than 800 [m³N /h] at maximum depositions of 0.0015 m during functioning.

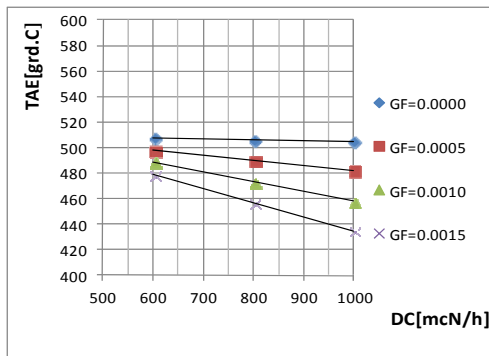


Fig.3 The combustion air preheating temperature, TAE, in [°C], depending on the natural gas flow, DC, in [m3N /h] and on the thickness of the deposition layer, GF, in m, for the mix recovery heat exchanger with cross parallel flow for the first three passes and countercurrent flow for the next five

Therefore, there was proposed to the Contractor to use the cross parallel flow scheme for the first three passes and countercurrent flow for the next five and the Contractor did not agree arguing this would change the initial offer we placed.

2 EXPERIMENTAL RESULTS

Cross countercurrent pre-heater heat exchanger schematically shown in figure 1, was manufactured and mantled on the aluminum scrap melting furnace. Figure 4 is a view of this air pre-heater while mounting it on the aluminum scrap melting furnace.



Fig.4 View of the air pre-heater while mounting it on the aluminum scrap melting furnace

After the Contractor started running the modernized furnace, he reported exceeding air preheating temperatures at the inlet of the new burners which are mounted by him. It has been found that the Contractor installed a lower flow air fan than indicated by our paper which did not assure the necessary flow for air exhausting into the atmosphere under specific operation conditions. Also, the Contractor installed 4 new burners, mounted two by two on the side walls with parallel air and natural gas flows, respectively, which collide above the liquid bath at a small distance from the flue gas exhausting hole. This incorrect solution, without

considering the CFD simulation, increased the flue gas exhausting temperature [9]. At approx. one month after starting operating the furnace this stops because of lack of combustion air. While dismantling the inlet flue gas chamber of the recovery heat exchanger, the following are found:

- the tubesheet, from the flue gas entrance side of the recovery heat exchanger is damaged (see figure 5 and figure 6);
- the pipes of the bundle of the recovery heat exchanger from the flue gas entrance side were submitted to higher temperatures than the accepted ones, on a maximum length of 110 mm;
- the ceramic fiber covering the turning loop of the exhaust flue gas from the furnace to the recovery heat exchanger is burned and shows the characteristics of burning at approx. 1250 °C as well as its fastening anchors;
- the deposition layer thickness is under 0.0001m and it is on the inside of the pipes on a length of only 0.7m towards the flue gas entrance side.



Fig.5 View of the air pre-heater, from the flue gas entrance side towards the damaged tubesheet



Fig.6 View of a part of the damaged tubesheet

3 RESULTS AND DISCUSSIONS

From the metallographic analysis and the chemical composition reports made by an authorized lab the followings resulted : from the sample microstructure (figure 7), of the heat treated area of the tubesheet we find intergranular rust aspects and isolated areas of intergranular rusty cracks in the austenitic matrix,

pressure corrosion areas under the conditions of high temperature exposure in aggressive environment.

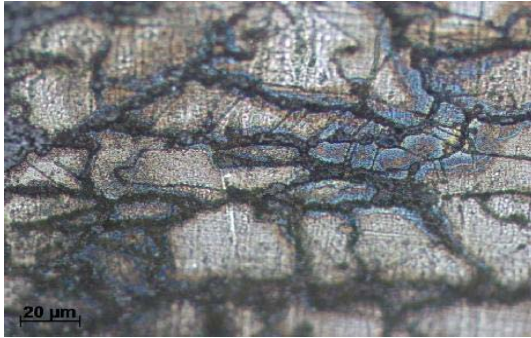


Fig.7 The sample microstructure of affected area from the tubesheet, by heat (x500)

From the sample microstructure (figure 8) of heat affected zone of the tube with a length of 100 mm we ascertain on the outer surface the depth of the corrosion of approx. 0.10 ÷ 0.15 mm. of the twinned polyhedra austenitic matrix and some carbide points. Enlarging X 500 titan nitride type inclusions are observed (figure 7).



Fig.8 The sample microstructure of the heat affected zone with a length of L=100mm (x500)

From the sample microstructure (figure 9) of the heat affected zone of the tube with a length of 25 mm we find that the inner surface is highly intergranular corrosive, which is as characteristic of the oxide environment exposure, highly aggressive and at high temperature.



Fig.9 The sample microstructure of the heat affected zone with a length of L=25mm (x500)

Consequently, the repairing of the cross countercurrent flow recovery heat exchanger is decided. The repairing of the cross countercurrent flow recovery heat exchanger meant the replacement of the tubesheet from the flue gas entrance side and of a 110 mm of the pipes.

In the same time, there was decided the use of the cross parallel flow scheme for the first four passes and the countercurrent flow for the next five, with varying distance between baffles (length of the pipes in one of the passes of combustion air) so that constant and high speeds of the combustion air should be reached and allowed by further use of the same air fan.

For such a recovery heat exchanger, named a mix, trials were run for various distance between baffles and under different natural gas flows, excess coefficients for the air and flue gas, respectively, and at different thickness values of the depositions on the inside of the tubes.

The input data and the obtained results on the computer, while running the sizing program for the functioning of the mix pre-heater heat exchanger, for instance, with a natural gas flow of 700[m³N /h] in a complete burning with an air excess coefficient of 1.15, the flue gas flow results of 8336.5 [m³N/h] and the thickness of the deposition layer is considered of maximum 0.001m are synthetically shown in table 1, 2 and 3. In table 1 the input data and parameters with constant values for the mix recovery heat exchanger are shown. Table 2 presents the results for the first four zones for which the flow is parallel and table 3 shows the results for the following five zones in terms of the countercurrent flow.

Table1. The input data and parameters with constant values for the mix recovery heat exchanger with cross parallel flow for the four passes and countercurrent flow in the following five

No.	Parameter	U.M.	Value
1	Natural gas flow	m ³ N /h	700
2	Combustion air flow	m ³ N /h	7636.5
3	Flue gas flow	m ³ N /h	8336.5
4	Efficiency	-	0.98
5	Air excess coefficient	-	1.15
6	Environment temperature	°C	40
7	Tube outside diameter	m	0.076
8	Tube wall thickness	m	0.003
9	Number of flue gas passes	-	1
10	Vertical length of the tubesheet	m	1.70
11	Horizontal length of the tubesheet	m	1.45
12	Tube pitch (vertical)	m	0.010
13	Tube pitch (horizontal)	m	0.011
14	No. of tubes on one row (vertical)	-	15
15	No. of tubes on one row (horizontal)	-	12
16	Distance to the wall (vertical)	m	0.010
17	Distance to the wall (horizontal)	m	0.010
18	Pressure	bar	1
19	Thickness of the scum layer	m	0.001
20	Deposition layer conductivity	W/m*K	0.1
21	Steel conductivity	W/m*K	50

Table 2. The results and the data regarding the different values parameters for the first four zones with parallel flow of the mix recovery heat exchanger

No.	Parameter	U.M.	ZONE I	ZONE II	ZONE III	ZONE IV
1	Inlet air temperature	°C	30	96	162	223
2	Outlet air temperature	°C	96	162	223	281
3	Inlet flue gas temperature	°C	950	901.3	851.2	801.7
4	Air heating value	W	185159.2	187613.1	184230.8	168873.4
5	Inlet flue gas heating value	W	3376173	3186158	2993977	2803526
6	Outlet flue gas heating value	W	3187235	2994716	2805987	2631206
7	Outlet flue gas temperature	°C	901.3	851.2	801.7	755.4
8	Average temperature difference	°C	852.6	747.0	635.3	526.1
9	Average gas temperature	°C	925.6	876.1	826.3	778.2
10	Average air temperature	°C	73.0	129.0	191.0	252.0
11	Distance between baffles	m	0.300	0.350	0.400	0.450
12	Flue gas flow section	m ²	0.692	0.692	0.692	0.692
13	Air flow section	m ²	0.161	0.188	0.215	0.242
14	Flue gas speed	m/s	14.67	14.07	13.46	12.87
15	Air speed	m/s	16.65	16.58	16.75	16.85
16	Flue gas convection coefficient	W/ m ² /K	21.81	21.74	21.65	21.51
17	Air convection coefficient	W/ m ² /K	59.56	59.89	61.00	61.97
18	Thickness of the gas layer	m	0.063	0.063	0.063	0.063
19	Gas radiation coefficient	W/ m ² /K	8.80	8.58	8.39	8.07
20	Gas transfer coefficient	W/ m ² /K	30.61	30.32	30.05	29.58
21	Overall heat transfer coefficient	W/m ² /K	3.98	3.96	3.96	3.95
22	Overall heat transfer coefficient	W/ m ² /K	17.35	17.29	17.30	17.24
23	Heating exchange surface	m ²	12.38	14.45	16.51	18.57
24	Air pressure loss	N/m ²	1058.5	1092.1	1167.2	1224.6
25	Gas pressure loss	N/m ²	31.99	30.71	29.49	28.24

Table 3. Results and data of the parameters with different values for the last five zones with countercurrent flow of the mix recovery heat exchanger (units of measure are identical to the one in the table 2)

No.	Parameter	ZONE V	ZONE VI	ZONE VII	ZONE VIII	ZONE IX
1	Inlet air temperature	281	321	360	398	439
2	Outlet air temperature	321	360	398	439	480
3	Inlet flue gas temperature	628	658	688	720	755
4	Air heating value	117490.8	115347.6	113137.7	122892.5	2629839
5	Inlet flue gas heating value	2161585	2272077	2375765	2498666	2503570
6	Outlet flue gas heating value	2041696	2154375	2260318	2373265	123743.1
7	Outlet flue gas temperature	596	628	658	688	720
8	Average temperature difference	311.6	299.5	286.5	278.9	273.0
9	Average gas temperature	612.5	643.0	671.4	703.1	738.1
10	Average air temperature	301.0	343.5	384.8	424.2	465.0
11	Distance between baffles	0.60	0.60	0.60	0.65	0.65
12	Flue gas flow section	0.692	0.692	0.692	0.692	0.692
13	Air flow section	0.322	0.322	0.322	0.349	0.349
14	Flue gas speed	10.84	11.21	11.56	11.95	12.38
15	Air speed	13.81	14.84	15.83	15.49	16.40
16	Flue gas convection coefficient	20.43	20.65	20.86	21.11	21.34
17	Air convection coefficient	53.43	57.16	60.85	60.37	63.80
18	Thickness of the gas layer	0.063	0.063	0.063	0.063	0.063
19	Gas radiation coefficient	5.85	6.41	6.97	7.60	8.31
20	Gas transfer coefficient	26.29	27.07	27.84	28.71	29.65
21	Overall heat transfer coefficient	3.54	3.67	3.80	3.86	3.99
22	Overall heat transfer coefficient	15.46	16.03	16.58	16.83	17.40
23	Heating exchange surface	24.77	24.77	24.77	26.83	26.83
24	Air pressure loss	698.3	894.0	1096.8	1047.5	1242.0
25	Gas pressure loss	23.9	24.7	25.5	26.3	27.3

For the mix cross flow recovery heat exchanger with parallel flow for the first four passes and countercurrent flow in the following five, the temperature of the tube wall reaches maximum 571 °C, which gives it a greater safety and longer life in comparison with the cross countercurrent flow recovery heat exchanger. In the same time, the maximum efficiency is reached by air preheating temperatures at the mix recovery exit point in 460-490 °C range.

A view of the new air pre-heater, from the exhaust gas entrance towards the tubesheet is shown in figure 10. Both the tubesheet and the side entrance taps of the air, the lower tap next to the tubesheet from the parallel flow zone and the higher tap from the countercurrent flow zone are covered with a metallic sheet for transportation purposes.



Fig.10 View of the repaired pre-heater from the flue gas entrance zone towards the tubesheet, covered by a metallic sheet for transportation purposes

After installing this recovery heat exchanger on the furnace, experiments will be undertaken in order to establish the functional parameters and its expected life term.

4 CONCLUSIONS

For the convection air pre-heater heat exchanger sizing we use our own mathematical model transcribed into a computer program in C + +. Simulations of different natural gas flows, different air excess coefficient, on the air and flue gas side, respectively, and of thickness of the deposition layers on the inside of the tubes were undertaken on the same construction option, with eight passes on a cross countercurrent flow recovery heat exchanger, as well as on a mix option of it, with the parallel flow on the first passes and countercurrent on the following ones. The Contractor decided to use the cross countercurrent flow recovery heat exchanger and 4 new burners, mounted two by two on the side walls with parallel air and natural gas flows, respectively, which collide above the liquid bath at a small distance from the flue gas exhausting hole.

The choice of the materials W1.4878 has been made as per the flue gas temperature (given by the Contractor in the project subject as 950°C) and as per the combustion air temperature in different operation regimes of the furnace, resulting a maximum tube wall temperature 700°C. This material has specified as heat treatment range 1020 ÷ 1120°C, without showing any micro structural change.

The lab results as well as the pictures shown, indicate a structural change, the occurrence of rust at the crystal limit and the burning of the sample material taken from the front tubesheet and from the welded tubes within. In conclusion, it follows that the flue gas temperature was much higher than the one in the project and over the indicated heat temperature.

Consequently, the repairing of the cross countercurrent flow recovery device is decided. The repairing of the cross countercurrent flow recovery heat exchanger meant the replacement of the tubesheet from the flue gas entrance side and of a 110 mm of the tubes. In the same time, there was decided the use of the scheme with cross parallel flow in the first four passes and cross countercurrent flow for the next five, with varying distance between baffles, so that constant and high speeds of the combustion air should be reached and allowed by further use of the same air fan. After installing this recovery heat exchanger on the furnace, experiments will be undertaken in order to establish the functional parameters and its expected life term.

5 REFERENCES

Journals:

- [1] Subodh, K.D., *Improving energy efficiency in aluminum melting*, DE-FC07-01ID14023, april 2007, http://www.phinix.net/services/Energy_Management/Improving_Energy_Efficiency.pdf.
- [2] White, D., *High efficiency aluminum melting, reverberatory furnaces and true ROI*, Die casting engineers, Jan.2011, pp.34-36.
- [3] Gorog, P., a.a., *Improved materials and operation of recuperators for aluminum melting furnaces*, DE-FC36-04GO14035,sept.2007. http://www.ornl.gov/sci/ees/itp/documents/FnIRptRecuperators_Final.pdf.
- [4] Schalles, D.G., *The next generation of combustion technology for aluminum melting*, <http://www.bloomeng.com/aluminum-studies.html>.
- [5] Schack, A., *Industrial heat transfer*, Chapmann and Hall, London 1965.
- [6] Heiligenstaedt, W., *Thermique appliques aux fours industriels*, Dunod, Paris 1971.
- [7] Gaba, A., *Heat transfer in industrial instalations*, Publishing Bibliotheca, Targoviste 2004.
- [8] Ward, M.E. a.a., *Application of a new ceramic recuperator technology for use on an aluminum remelt furnace*, *Gas Warne International*, band 37 (1988) heft 3, April, pp. 144-148.
- [9] Murza, S., Henning, B., Jasper, H.D., *CFD simulation of melting furnaces for secondary aluminum*, *Heat processing*, 2/2007, pp.122-126.

DETERMINING THE HEAT REGIME IN THE WORKING OF A COUPLING WITH SLIDING MOTION

Ivona PETRE, Elena Valentina STOIAN, Maria Cristiana ENESCU

Valahia University of Targoviste, Faculty of Materials Engineering and Mechanics,
Department of Materials Engineering, Mechatronics and Robotics,
Str. Aleea Sinaia, No. 13, Targoviste, Romania

E-mail: petreivonacamelia@yahoo.com

Abstract. *Following the sliding motion between two surfaces a heat release occurs which leads to a changing of the mechanical properties of the surfaces in contact. Amongst the factors that influence the heat release one may name the loading, the velocity, the surface topography, the surface material, the lubrication and last but not the least, the environment.*

The present paper proposes a computation model to determine the temperature in the working of a coupling to which the mechanical characteristics of the materials are not affected by changes which, at their turn, lead to undesired effects.

Keywords: *friction coupling, temperature, heat flux, contact surface, working parameters*

1. INTRODUCTION

The scientific literature abounds of opinions on the thermic aspects that occur during the working of a friction coupling. The temperature distribution in a coupling depends on the interconditioning of the working parameters (loading, speed etc), on the surfaces topography, on the properties of the materials in contact, on the lubrication etc.

It is considered that for small loadings, the contact between surfaces occurs on a finite number of asperities which define the nominal area or the contact area and the heat transfer is solid. For big loadings, the real contact area is closed to the nominal one and the heat transfer in asperities is a unidimensional one. When a lubricant film is inserted between the surfaces, the heat released following the sliding motion (friction) also get through the film, the lubricant being essential in diminishing the thermic effects.

In order to explain the distribution of the temperature and heat resulted by the friction of a sliding coupling, the most unfavourable case is considered, when between surfaces there is no lubricant film to help in fast release of heat during working.

2. WEAR MODEL BY MICRO-JUNCTIONS MELTING AND SHARING

Following the friction process, the temperature resulted by the friction of the asperities in contact is much higher than the medium temperature of the coupling surface [1,2,3,4]. It is considered that in the contact points of the surface asperities the temperature is so high that it generates the melting of the material.

The temperature value generated during the coupling working is connected with the loading parameters – contact pressure, sliding speed. For high pressure and speed (10-1000m/s) a fluid metal film that leads to a

“lubrication by melting” results [2,3,4,5]. Though the friction coefficient decreases because of this melting layer, the wear increases because the high temperature continues to melt more and more solid material.

For a complex analysis of the friction coupling wear process, wear maps may be defined to illustrate the interconditioning way of the working parameters so that to obtain a maximum durability or an imposed working precision for the friction coupling.

A wear model by micro-junctions melting and shearing is proposed by Lim and Ashby [6,7,8,9]. They got to the conclusion that the wear by melting takes places when the power dissipated by friction on the surface unit exceeds a certain value considered critical.

For a geometry of the pin-disk type surfaces with a circular movement, it is considered that the heat release occurs in the sliding area and its dissipation occurs only through the friction coupling elements.

It is estimated that a part (α) of the heat released (q) is dissipated in the pin and another part ($1-\alpha$) is dissipated in the disk. Evaluation of the heat partition coefficient (α) is done by considering that the medium temperature on the mobile surface is equal to the temperature on the fixed surface [10,11,12].

This coefficient depends not only on the thermal diffusion of the material and the piece size but also on the rate of travel of the coupling elements. This speed is determined by the help of the Peclet invariant [11,12,13,14] which is for the specific case of the contact (pin-disk):

$$Pe = \frac{vL}{4a_2}$$

where: a_2 - thermal diffusion of the pin material;

L - contact surface of the pin

Function of the Pe invariant, the partition coefficient is:

$$\alpha = \frac{\lambda_1}{\lambda_1 + \lambda_2} \text{ for } Pe \leq 0,1$$

$$\alpha = \frac{1}{1 + 0,795 \frac{\lambda_1}{\lambda_2} \left(\frac{a_1}{a_2}\right)^{1/2} Pe^{-1/2}} \text{ for } Pe \geq 5$$

$Pe \geq 5$

where: λ_1, λ_2 – thermic conductivities of the disk material, respectively of the pin

a_1, a_2 – thermic diffusion of the disk/pin material

For values of the Peclet invariant between $0,1 < Pe < 5$, a linear interpolation is recommended.

Considering, according to the mechanical molecular theory, that the friction is achieved at the asperities contact level, on the real contact area, the friction coefficient is:

$$\mu = \frac{\bar{\tau}}{p} + \mu_m$$

where: $\bar{\tau}$ - specific molecular resistance of material;

p - loading parameter;

μ_m - mechanical part of the friction coefficient

For the mechanical part of the friction coefficient (μ_m), the dependence of the Pe invariant is accepted as [8]:

$$\mu_m = \frac{2}{\pi} \text{tg}\theta \left(\frac{Pe \cdot 4 \cdot a_1}{L}\right)^a$$

where: θ - attack angle of the pin asperities;

a - a constant that depends on the material type.

After getting the thermic equilibrium in the elements of the two coupling, liniarizing the first law of the heat flow, the medium temperature of the contact surfaces may be established:

$$T_m = T_o + \alpha \mu F v \frac{l_m}{A_n \lambda_2}$$

where: T_o - temperature of the clamping system (about 20°);

μ - friction coefficient between the coupling materials;

F - coupling loading;

v - displacement speed;

l_m - distance of diffusion of the heat to the pin clamping system;

A_n - nominal contact area;

λ_2 - thermic conductivity of the pin material

For a pin-disk type friction coupling whose material and geometry features are known, one may establish the evolution of the medium temperature for different loadings (\bar{p}), function on the Peclet dimensionless speed, for the three intervals (Pe_1, Pe_2, Pe_3) (figure 1).

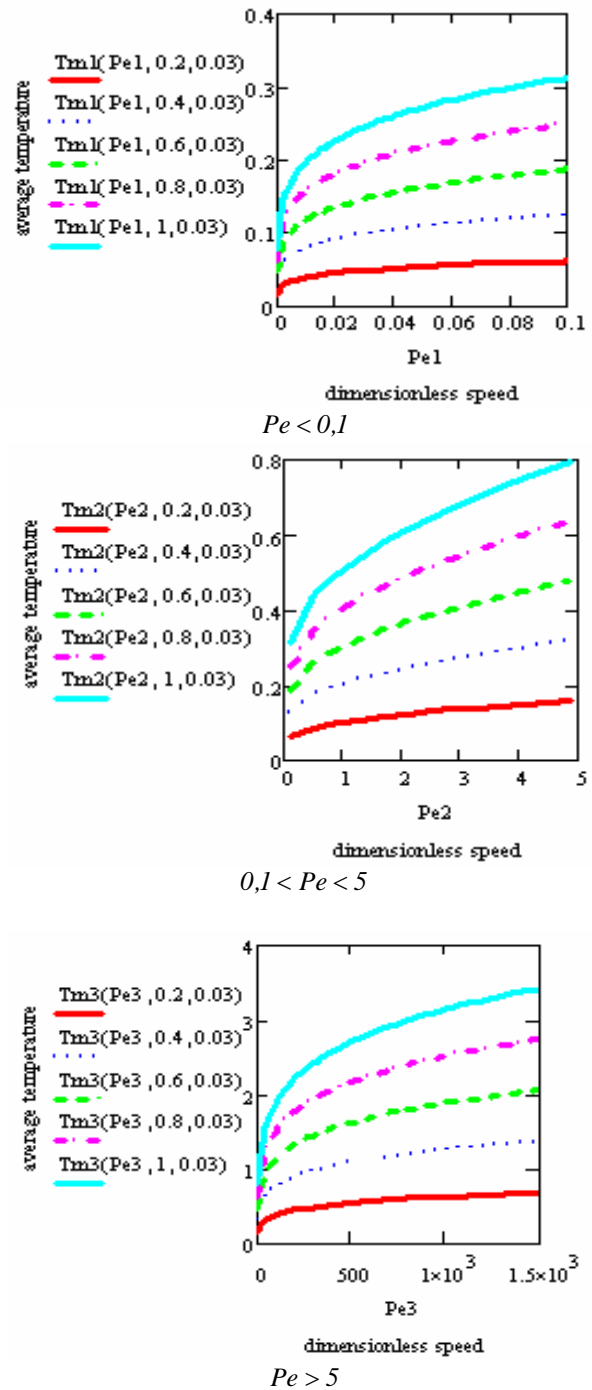


Fig.1 Variation of medium temperature with loading and Peclet variant

It is noted that the higher loading and speed of the coupling, the higher medium temperature on the contact surfaces.

With the view to evaluate the instant temperature, one says that the contact area increases with the external load as a result of the increase of the micro-areas. For small loadings, the total number of micro-areas in contact tends to one, and for large loadings the micro-areas get connected so that the nominal area tends to be equal to the real area ($A_n = A_r$). The solutions accepted by Tian and Kennedy [6,10,11,12] at the level of the surface micro-contacts appraise the dimensionless instant temperature as:

$$T_i = 2,72 \frac{r_a}{L} \frac{A_n}{A_r} \frac{(\bar{\tau} + \mu_m)Pe}{\sqrt{0,6575 + \left(2 \frac{r_a}{L}\right) Pe \left[1 + \frac{A_n}{A_r} \bar{p}(1 - \bar{p})\right]}}$$

where r_a is the micro-contact radius.

Fig. 2 presents the theoretical evolution of this instant temperature with the speed parameter Pe , for a pin-disk type friction coupling whose dimensional and material features are known. In case of small and very small speeds, for a large loading, the increase of temperatures at the asperities peak is high. For small loadings, the increase of instant temperature is much slowed. If the instant temperature is limited by factors connected to the wear intensity by friction, a map of the dimensionless loading function of the dimensionless speed for different instant temperatures may be determined (Fig. 3).

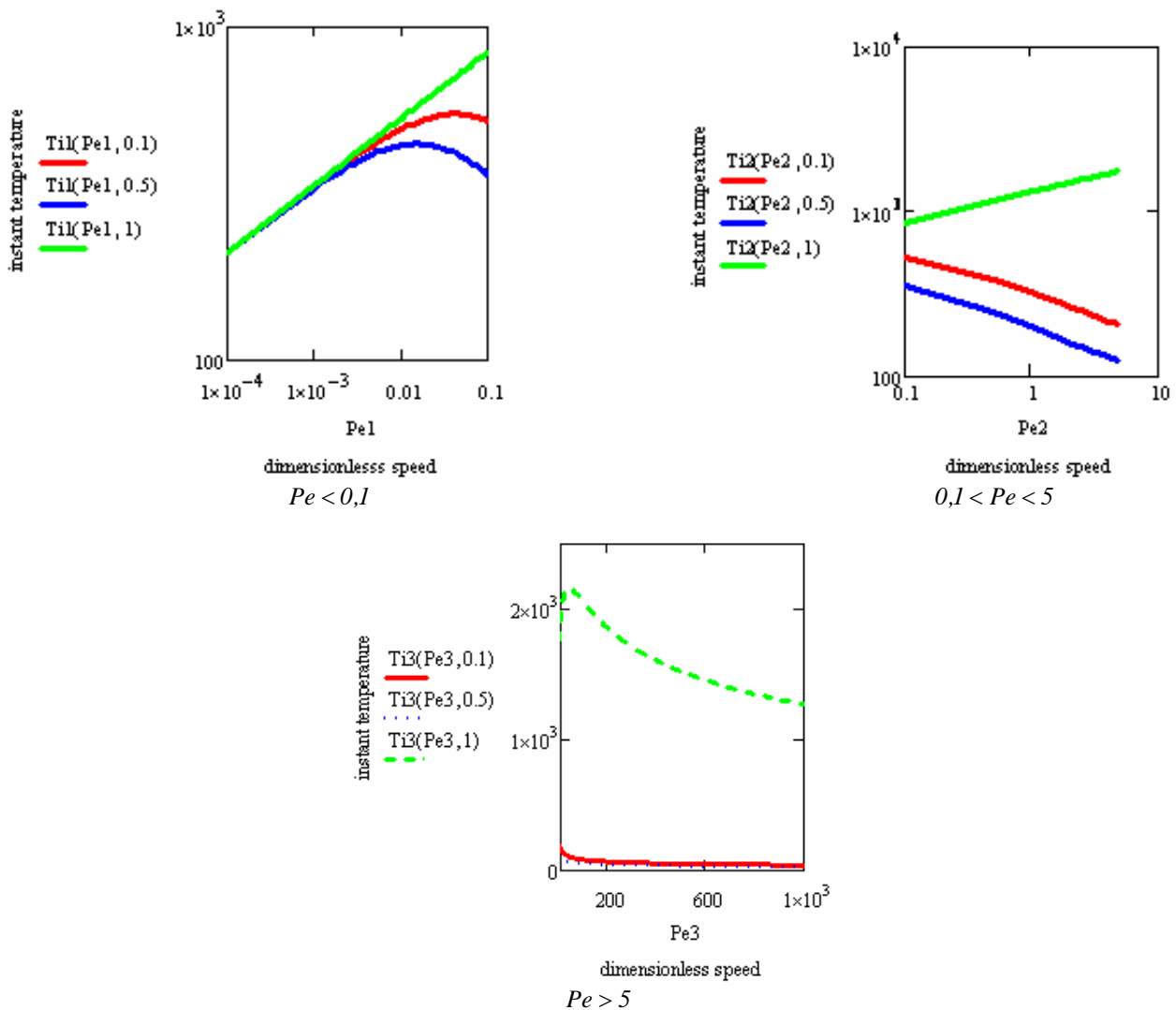


Fig. 2 Instant temperature evolution with speed parameter

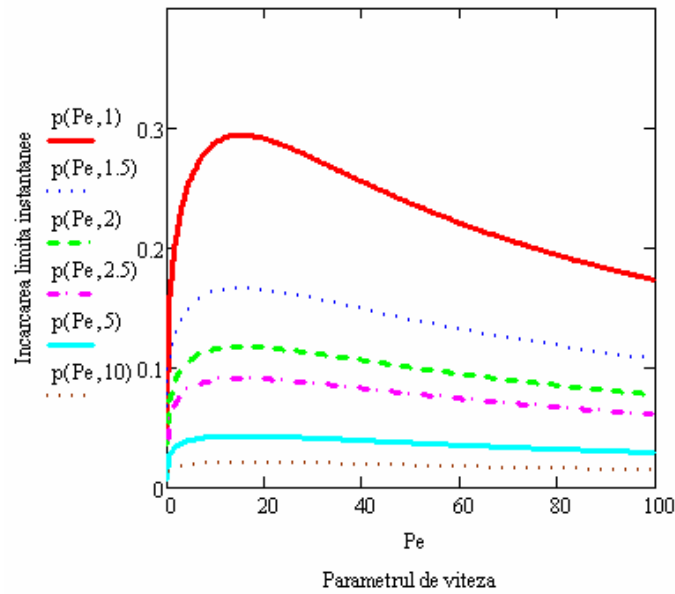


Fig. 3 Loading evolution for different temperatures

The increase of temperature in the contact area of the asperities also influences the hardness of the surfaces in contact. Thus, at the asperities level, a change in their micro-hardness occurs. This results in local plastic deformations occurrence which, at their turn, negatively

influence the good working of the coupling. If this law is applied at the micro-contacts level, for an instant temperature, the map of micro-hardness variation may be obtained (Fig.4).

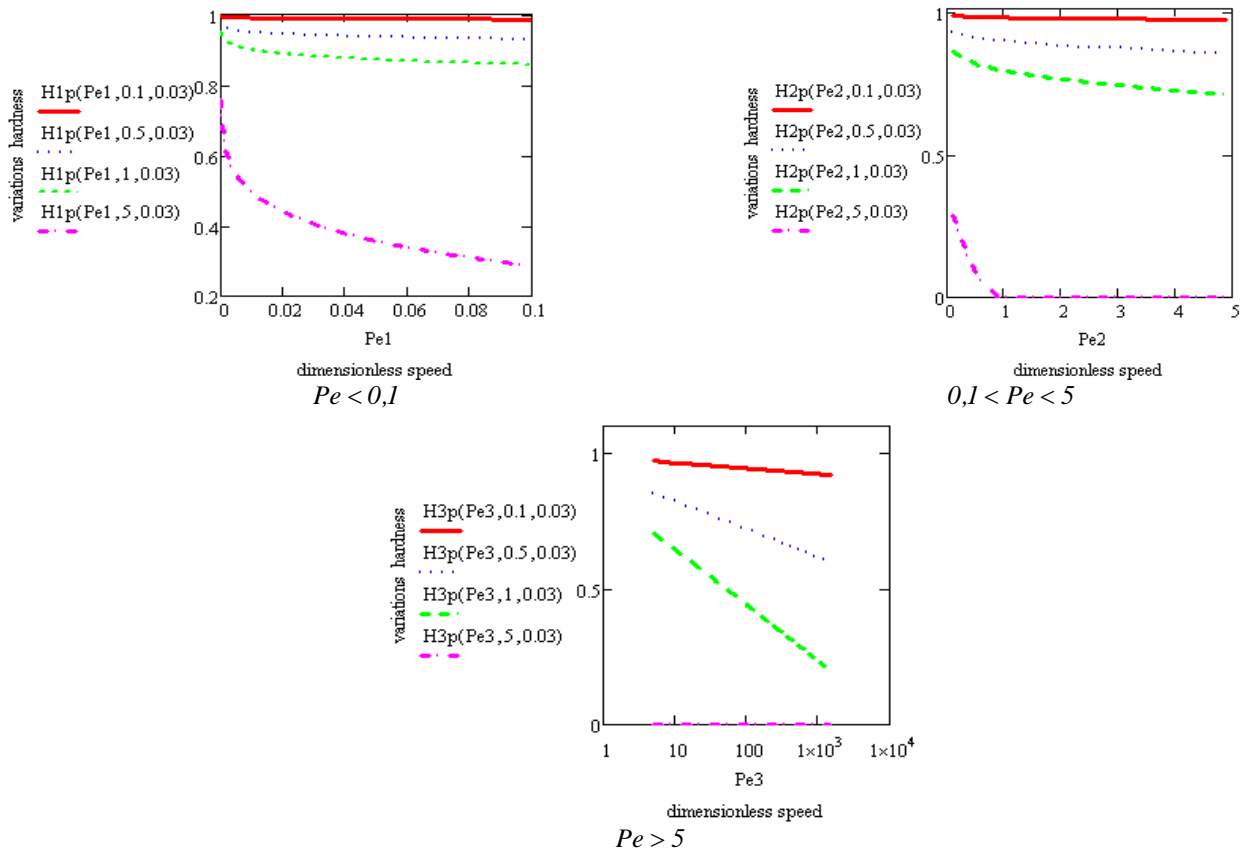


Fig. 4 Hardness variation for instant temperature

All these changes combined with the fatigue by friction are conclusive in wear particles occurrence [6, E, 7]. For the practical example, at the micro-contacts level, the variation of the flow voltage with the local contact

temperature is considered [3,8,13,14]. So, the linear intensity of wear for each element may be determined, this one being an indicator of wear process if the following are known: the length of friction for a single

cycle of each element of the coupling (L_{01}), the number of friction cycles (N_c) and the thickness of the worn layer (Δh_{12}):

$$I_{h1,2} = \frac{\Delta h_{1,2}}{N_c \cdot L_{01,2}}$$

Figure 4 presents the evolution of the wear intensity for a pin-disk type friction coupling whose dimensional and material features are known, according to the mathematical model proposed. One may note the decrease of the wear intensity with the loading parameters and temperature.

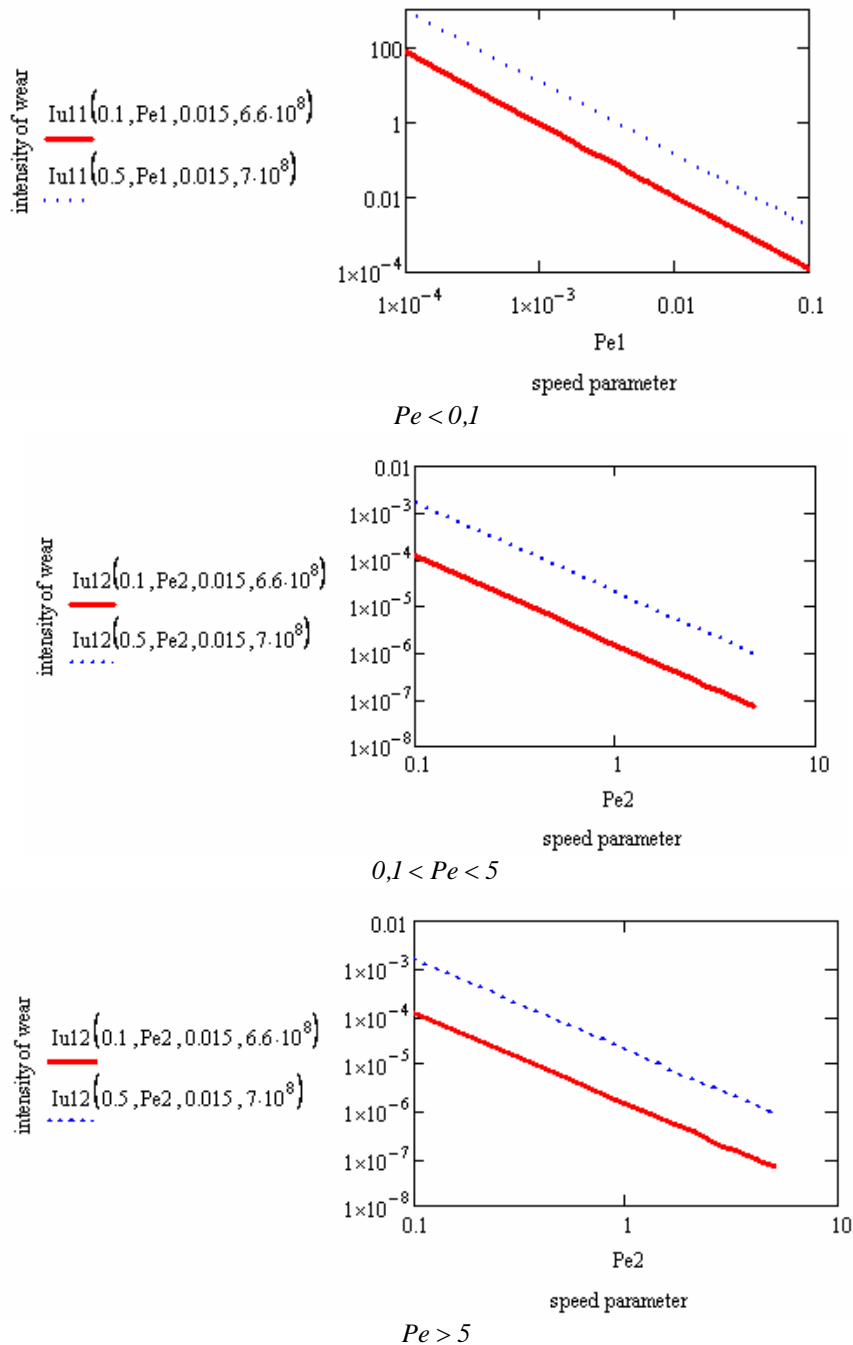


Fig. 5 Evolution of the wear intensity

If the contact surface remains constant during the wear, the wear coefficient may be determined:

$$k = \frac{\Delta V_{12}}{F \cdot L_{f1,2}} = \frac{A_n \cdot \Delta h_{12}}{F \cdot L_{f1,2}} = \frac{A_n \cdot \Delta h_{12}}{p_n \cdot L_{f1,2}} = \frac{I_{h12}}{p}$$

where: ΔV - worn material volume;
 F - normal force transmitted;
 $L_{f1,2}$ - friction length of the couplings;
 p_n - normal pressure

3. CONCLUSIONS

In designing any friction couplings one may establish from the beginning the optimal working conditions by interpreting the experimental analytical results with the help of the wear maps. These ones provide information with regard to the velocity parameter and the exploiting conditions. It may be considered that the working of the coupling is optimal if the velocity parameter and the exploiting conditions are situated under these high curves. These wear maps are considered working tools for tribological applications.

4. REFERENCES:

- [1] Gas,C., Kuhlmann, D., et all. - Fundamentals of stick-slip, *Wear* 162-164, (1993), p.1139-1149;
- [2] Gecim, B. and Winer, W.O. – Transit Temperatures in the vicinity of an asperity contact, *Trans ASME, Journal of Tribology*, vol. 107, 1985, p.333-342;
- [3] Aderghal, N., Loulou, T., Bouchoucha, A., Rogeon, Ph., - Analytical and numerical calculation of surface temperature and thermal constriction resistance in transient dynamic strip contact, *Applied Thermal Engineering* 31(8-9), 2011, 1527-1535;
- [4] Pavelescu, D., Muşat, M., Tudor, A., - *Tribologie, Ed Didactică și pedagogică, bucureşti* 1977, p.140-162;
- [5] Greenwood, J.A. – An interpolation formula for flash temperatures, *Wear*, 150, 1991, p.153-158;
- [6] Lim, S.C. and Ashby, M.F. – Wear mechanism maps, *Acta metall*, vol 35, no 1, 1987, p.1-24;
- [7] Kennedy, Jr.F.E. – Thermal and thermomechanical effects in dry sliding, *Wear*, 100, 1984, p.453-476;
- [8] Tian, X. and Kennedy, F.E.- Maximum and average flash temperatures in sliding contacts, *Journal of Tribology*, jan. 1994, vol 116, p.167-174;
- [9] Tian, X. and Kennedy, F.E.- Contact surface temperature models for finite bodies in dry and boundary lubricated sliding, *Journal of Tribology*, jan. 1993, vol 115, p.411-418;
- [10] Blok,H., - The Flash temperature Concept, *Wear*, 6, 1963, p.483-494;
- [11] Yevtushenko, A.A., Ivanyk, E.G., and Ukhanska, O.M. - Transient temperature of local moving areas of sliding contact, *Tribology Intl.*, 30, 1997, p. 209-214;
- [12] Greenwood, J.A. - An interpolation formula for flash temperatures, *Wear*, 150, 1991, p. 153-158
- [13] Bond-Zen Ting, Winer, W.O. – Friction induced thermal influences in elastic contact between spherical asperities, *Journal of Tribology*, 1989, vol.111, p.315;
- [14] Tudor A. și Petre I. – Câteva considerații privind aplicarea uzurii termomecanice la ghidajele cu alunecare, *Conferința VAREHD* 9, 1999, p. 345 – 348.

NEW CONCEPTS OF MODELING AND COMPLEX SIMULATION OF ELECTRONIC CIRCUITS FOR INTERFACING TACTILE SENSORS IN CYBER-MECHATRONIC SYSTEMS

Anghel CONSTANTIN¹, Gheorghe Ion GHEORGHE^{1,2}

¹National Institute of Research and Development in Mechatronics and Measurement Technique, Bucharest, Romania

²Valahia University of Targoviste, Romania- Faculty of Materials Engineering and Mechanics

E-mail: anghel.constantin@incdmtm.ro, geocefin@yahoo.com

Abstract. The paper presents an original concept for interfacing tactile force sensors in modern cyber-mechatronic systems. The authors show the results and conclusions of a PSPICE simulation of an original patented circuit. In the simulations, in models used were introduced some circuit components corresponding to the physical implementation for a practical mechatronic system which has already been used for the analysis of human walking. After these simulations were revealed important aspects of dynamic behavior and was proposed an optimal variant of the interface circuit as a non-typically instrumentation differential circuit spitted in two parts, one near to the sensor, and the second far from the sensor and close to an A/D converter of the data acquisition system. For electrical links between the two parts can be used low cost cable without important loss of the signal / noise ratio.

Keywords: PSPICE, simulation, tactile sensor, interface

1. INTRODUCTION

This paper presents recent research about the optimal design [1] of an electronic interface circuit between a tactile force sensor and the data acquisition system. Thus it is continued an original patented idea and an electronic schematic topology which is discussed in another article [2]. Based on practical observations, it was designed an optimization schematic by PSPICE simulation using complex models that approximates

physical reality in the real working environment. In the researched application the used sensor is a FlexiForce type – see Fig 1 a. The classical interface circuit is to introduce the sensor in a conductance-voltage converter circuit. In this case, can be achieved a calibration method for converting the output signal in measuring units for the force. The diagram which is recommended by the producer [3] is using a classical circuit like in Fig 1 b.

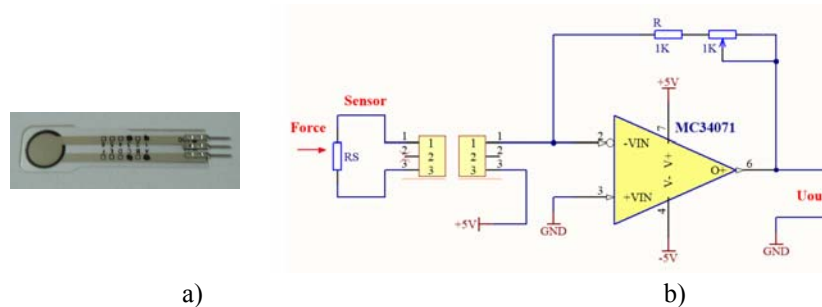


Fig.1 – a) Tactile sensor FLEXIFORCE and b) Classical schematic interface

FlexiForce sensor is made by laminating two flexible and polyester / polyamide thin films (thickness: 0.008 inch), each of them being re-covered with a silver film which serves as a conductor on the one hand and, on the other hand, playing the role of electrodes that define the geometry of the sensitive area. Between the two circular silver electrodes is inserted a pressure sensitive layer

made of special ink. When the sensor is unloaded its resistance is very high ($1 \div 2 \text{ M}\Omega$). That is the first observation [4].

If a force is applied on the sensor, its strength decreases, as shown in Fig. 2; the sensor is sensitive and have quasilinear behaviour.

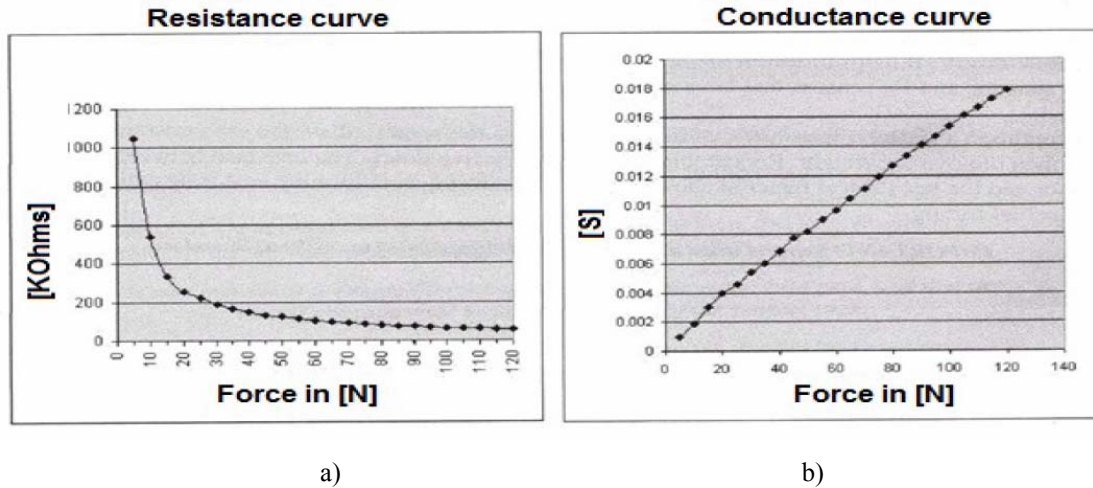


Fig.2 – a) Tactile sensor resistance b) Tactile sensor conductance

The classic circuit presents a great disadvantage in terms of common mode noise analyzed in detail in [2]. Fig. 3 shows the original patented circuit which has the advantage of drastically reducing the common mode noise and providing very good linearity. The tactile

sensor is placed as variable conductance on the position that sets the gain of an instrumentation amplifier circuit excited with a greater stability DC voltage made by a precision reference source.

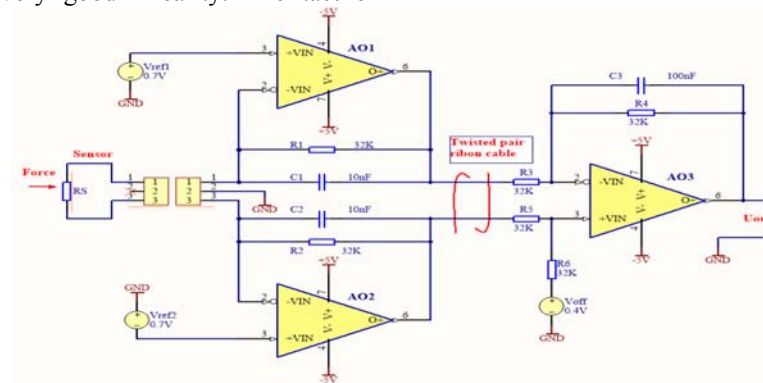


Fig.3 – Original circuit with high linearity and high common mode perturbation rejection

2. PSPICE MODELING AND SIMULATION

For optimal design of the interface circuit were investigated multiple circuits topologies for simulation and modeling of components with values close to reality as physical circuit. Thus, for the sensor was designed a model based on linear sources in order to create a

voltage controlled conductance. This allows the complex simulations and analysis such as the indicial step response (transient analysis), linearity, frequency response, Monte Carlo analysis and others. The symbol for voltage controlled conductance is shown in Fig4.

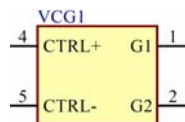


Fig.4 – Symbol for Voltage Controlled Conductance

Where: CTRL+ and CTRL- represent the connections for control voltage used in range 0-10V, and G1, G2 are the two connections of the controlled conductance with real range of the sensor.

The model for voltage controlled conductance is presented in the standard PSPICE in TABLE 1:

TABLE 1 – The PSPICE model code

```

*****VOLTAGE CONTROLLED CONDUCTANCE *****
*****PSPICE MODEL SUBCIRCUIT *****
* CONDUCTANCE - 1, 2 CONTROL - 4, 5 *
*****
.SUBCKT VCCconductance 1 2 4 5
ERES 1 3 VALUE = {I(VSENSE)*100K/(V(4,5)+0.001)}
VSENSE 3 2 DC 0V
.ENDS VCCconductance
    
```

2.1 Circuit Simulations Results

Fig. 5 shows the schematic circuit used for simulation. Actually, it is the diagram in Fig. 3 to which were added new circuit components such as parasitic capacitances of the connections wires between the sensor and the circuit (C6) and between the differential input of the circuit and single ended output circuit U1B. Because U1B and U1C are placed remotely and are connected with U1A, with a twisted pair ribbon cable which has parasitic capacitances (C3, C4 and C5) nanofarads

values. The spitted instrumentation circuit is part of the original idea for transmitting analog signals remotely (1m) in a differential mode with the multiple advantages derived from it. The input circuit is symmetric and placed near the sensor, and the differential outputs are transmitted at approx. 1m from where they are differentiated and this operation improves global signal to noise ratio.

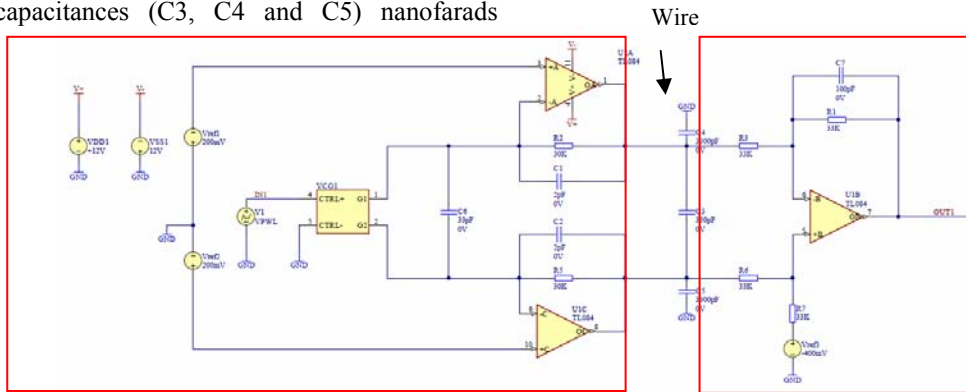


Fig.5 – Simulation circuit with parasitic capacitance models

Running the Transient Analysis and AC Analysis we determined the signal step response and the frequency response feature of the sensor interface circuit - considering that the variable frequency source is V1 as the range of forces applied is of 0 - 100N (the sensor resistance varies from the 5MOhms to 1Kohm). In Fig. 6

are depicted the settings used as PSPICE directives analysis in Altium Designer software. For the Transient Analysis was checked the option "Use initial conditions" and for capacitors was considered the null voltage as the initial status [5].

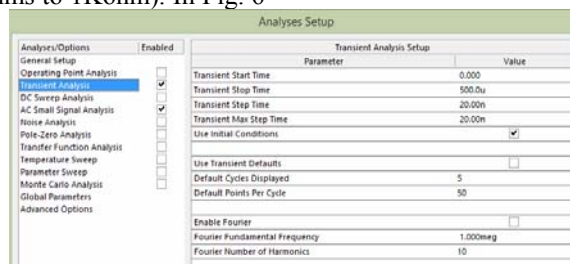


Fig.6 – Simulation options in Altium Designer

The simulations results are showed in the following charts. Fig. 7 shows the Transient Analysis step response with signal sensor in the range 0 - 100N. The resistors of the schematic circuit were calculated for a maximum output signal does not exceed 2.5V well the maximum input voltage allowed from the acquisition system used. Fig. 8 shows the result of AC Analysis simulation for frequency behavior.

Observe that the circuit has a frequency characteristic as a Low Pass Filter (LPF) with a bandwidth about 10KHz but both simulations show an instability with null load (equivalent resistance of the sensor is high - about 5MOhms) hereby parasitic oscillations with a frequency around 300KHz occur.

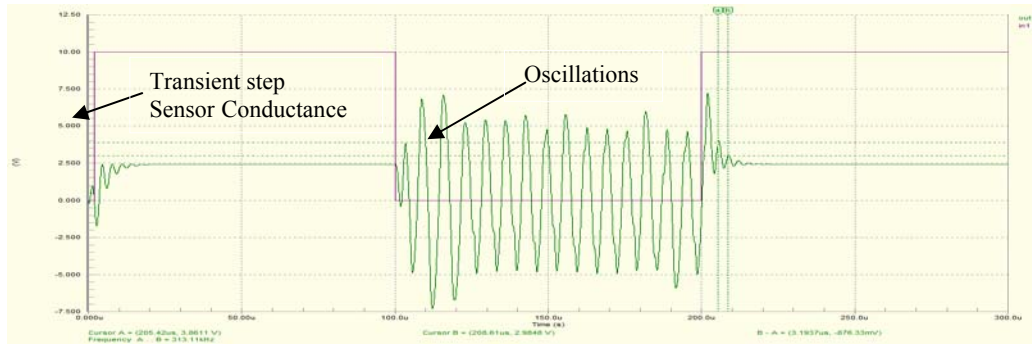


Fig.7 – Simulation results of Transient Step Response

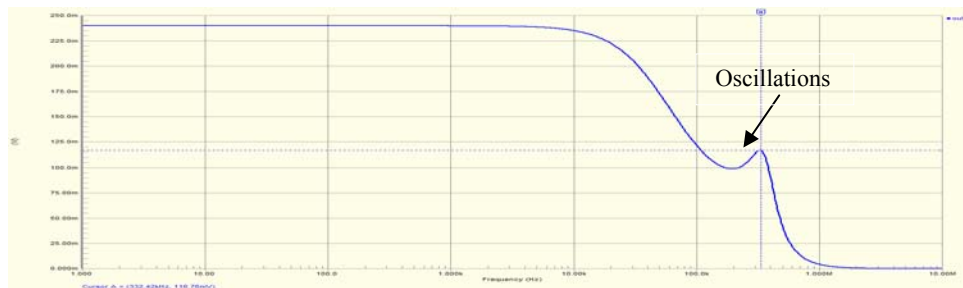


Fig.8 – Simulation results of AC Analysis response

2.2 Circuit Simulations Results after Optimisations

Analyzing the causes of unwanted oscillations that occur when the force pushes a little bit the sensor (the conductance is very small and equivalent resistance is very high) found in datasheet of the operational amplifiers (OPAMPS) does not accept a capacitive loads exceeding 100pF [6]. But the wire capacitance have

nanofarads values and can not be reduced by simple methods. A good idea is to place the resistors R3 and R6 near the outputs of the amplifiers U1A and U1C and after this connecting the wires to remote input of the amplifier U1B. The new topology scheme was modeled and simulated as shown in Figure 9.

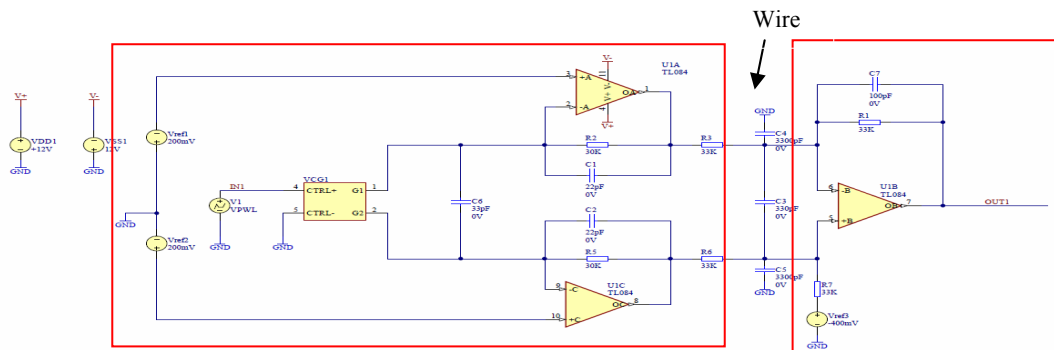


Fig.9 – Optimal topology of the circuit interface

Fig. 10 shows the result of the Transient Analysis simulation indicial response. The disappearance of the unwanted oscillations are observed even at very

null load of the tactile sensor The rise time and the fall time is the same because of the symmetry of the input circuit.

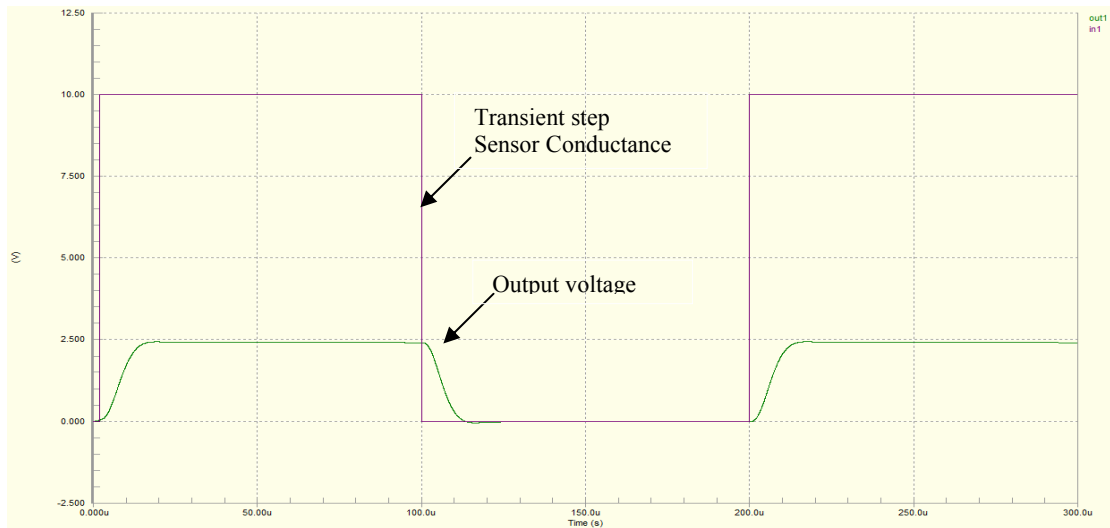


Fig.10 – Simulation results of Transient Step response

Fig. 11 shows the simulation results of the characteristic frequency of the entire interface circuit and sensor. Here is obvious the disappearance of the

oscillations and in general, it represents a characteristic of a second order LPF with cutting frequency (Cutoff Frequency) around 46KHz

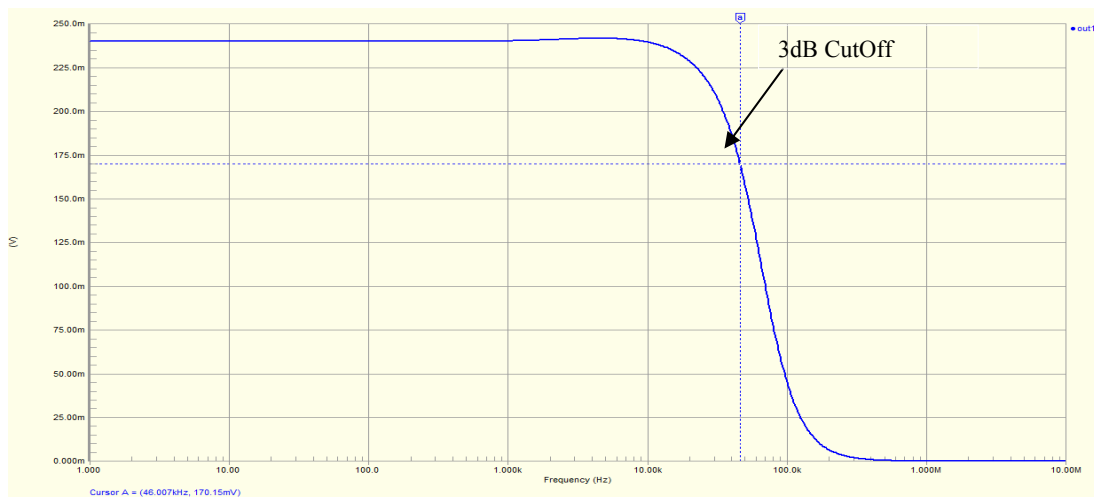


Fig.11 – Simulation results of AC Analysis response

3. CONCLUSIONS

By complex modeling of the real elements of connections (wires) between the sensor and the circuit interface on the one hand and the input interface with the remote circuit at 1 m distance on the other hand were obtained remarkable results confirmed by the experiments: linearity, stability and immunity to disturbances [7].

Thus it is noted that by placing resistors R3 and R6 near the output amplifiers U1A and U1C (basically in series with connection wires between blocks) can be minimized the capacitive loading of the outputs which eliminates the unwanted oscillations due to instability.

Also, R3C4 and R6C5 together with C3 form an additional LPF filter that improves the noise immunity.

The Bandwidth of the circuit around 40KHz is enough to use the tactile sensors in the cybermechatronic systems for vibration analysis up to 20KHz bandwidth (according to Shannon Theorem) [8,9].

Increasing the values of C1, C2 and C7 can decrease to the minimum allowable Bandwidth until the band reaches the useful frequency of sensor signal.

The circuit is optimal but other issues may be discussed yet concerning the choice of operational amplifier circuits and their power for remote or local.

4. REFERENCES

- [1] Anghel Constantin, Dumitru Sergiu, Patent no. 125345 / 08 August 2007, OSIM, Bucharest, Romania
- [2] ANGHEL V. Constantin, GHEORGHE Ion Gheorghe, Research on Tactile Sensors Interface - Review of Theoretical and Practical Approach, Applied Mechanics and Materials Vol 772 (2015) pp 299-304 Submitted: 2015-02-02, Trans Tech Publications, Switzerland Revised: 2015-02-11
- [3]. ***, Tekscan - A201/ AH2, User manual;
- [4] Gheorghe I. Gheorghe, Vasile Bratu, Octavian Dontu, Adaptronics an intelligent science adaptive to advanced systemes/micronanosystem, Applied Mechanics and Materials.2013. 332:471-484, ISSN: 1662-7482 -ISI
- [5] ***, TL084ACD datasheet, <http://www.farnell.com/datasheets/1764390.pdf>
- [6]. Jon S. WILSON, Sensor Technology Handbook, British Library Cataloguing, Publication Data 2005, ISBN: 0-7506-7729-5;
- [7] Vasile Bratu, Marian Ionescu, Tehnologii și Inovații. - Targoviste: Valahia University Press, 2014, ISBN 978-606-603-097-7
- [8] Octavian Dontu, Gheorghe I. Gheorghe , D. Besnea, I. Avarvarei, R. Ciobanu, Experimental and theoretical studies regarding intelligent sensors and actuators of high precision used in precision mechanic, mechatronics and robotics domain, International Conference on Mechanical Engineering, Robotics and Aerospace, CMERA 2010, 2-4. dec.2010, Bucharest, Romania; ISI
- [9] Machado Jose, Seabra, Eurico, HiL Simulation Workbench for Testing and Validating PLC Programs, 2013 11th Ieee International Conference on Industrial Informatics (Indin) pp: 230-235.

NEW CYBER-MIXMECHATRONIC CONCEPT FOR THE REALIZATION OF SMART CYBERNETIC SYSTEMS WITH APPLICATIONS IN THE INDUSTRY, ECONOMY AND SOCIETY

Gheorghe Ion GHEORGHE^{1,2}, Anghel CONSTANTIN^{1,2}, Iulian ILIE¹

¹National Institute of Research and Development in Mechatronics and Measurement Technique– Bucharest, Romania,

²University „VALAHIA” of Targoviste – Faculty of Materials Engineering and Mechanics

E-mail: geocefin@yahoo.com, anghel.constantin@incdmtm.ro

Abstract: *The current scientific work show for the first time, (i) a new complex mixmechatronic concept of integration and fusion in the structures of smart technical and technological systems and (ii) the systems of electronic control for holistic physical-virtual assembly.*

The content of the paper highlight some results of professional researches in Mechatronics and Cyber-Mix Mechatronics fields at the National Institute of Research and Development in Mechatronics and Measurement Technique– Bucharest and also at Politehnica University of Bucharest (PUB) from Romania. Some of these results are in the process of transfer and capitalization to the industry, economy and society.

Keywords: *cyber-mixmechatronic concept; cyber systems; electronic control; holistic physical and virtual assembly; mechatronics and cyber-mechatronics.*

1. INTRODUCTION

This scientific work responds to "challenge in the paradigm of European strategy" to create and develop new scientific concepts and Intelligent new systems with Multi-applications into new industrial value chains. The scientific work require focus, combining and merging various skills and innovative solutions - especially new multidisciplinary mechatronic, cyber-mechatronic and cyber-mixmechatronic technologies - and integrating them into solutions and advanced competences with high-tech IT & C for efficiency and eco-innovation of more advanced and intelligent products, systems and systems of systems.

In these mechatronic and cyber-mechatronic systems, mechatronics and cyber-mixmechatronics facilitate an integrative-generative behavior in (a) the whole mechatronics, mixmechatronics and cyber-mixmechatronics elements or (b) in the elements of calculation, control / remote control, detection / remote sensing and monitoring / remote monitoring and smart grids. These items can be deeply integrated and assembled, and their actions can be safe and interoperable.

2. THE NEW CYBER-MIXMECHATRONIC CONCEPT INTEGRATED IN THE ARCHITECTURE AND CONSTRUCTION OF INTELLIGENT MULTI-APPLICATION CYBER SYSTEMS

Integration of new and complex concept includes a flexible fusion of architecture of smart mechatronic,

cyber mechatronic and cyber-mixmechatronic systems expressed by the complex structures of specialized sensors and actuators. They are placed on physical work systems – both static systems and/or mobile, that sends information to smart 4G devices, and also process, store or transmit them to other entities or centers of monitoring /remote monitoring, for control databases. Using 4G smart devices allow monitoring, diagnostics and interventions in real-time, remotely, for all intelligent mechatronic systems and static and mobile equipment. Multi-application and adaptive mechatronic, cyber-mechatronic and cyber-mixmechatronic systems, can be used and developed in the form of a "black box" entity that will integrate innovative hardware circuitry and software for the capture, modeling and communication of data to or from a "command center".

The architecture of multiplicative adaptive devices/mechatronic, cyber-mechatronic and/or cyber-mixmechatronic systems will be modular, with the possibility of integrating other devices / smart sub-devices type "add-on" - special or dedicated to certain specific activities.

The types of data captured by these devices / sub-device smart will be processed, normalized and standardized by a multi-application and adaptive mechatronic cyber-mechatronic and/or cyber-mixmechatronic system/mother device, in formats that ensure interoperability with the platform for real-time monitoring.

The complex mechatronic, cyber-mechatronic and/or cyber-mixmechatronic concepts can be applied in many industrial environments, such as:

- remote monitoring and remote control in real time of the quality and functioning of electronic control of the automotive;

- remote monitoring and remote control in real time of the parameters of complex thermo-chemical treatment for installations with controlled atmosphere for thermo chemical treatment of machine parts;
- remote monitoring and remote control in real time for the quality of hydraulic oil from the drive farm machinery;
- remote monitoring and real-time control for CO2 and other exhaust gases in the automotive industry;
- remote monitoring and remote control in real time of the quality and functioning of electronic and automotive control stability and direction;
- remote monitoring and remote control in real time of innovative technology separation and selection of waste paper and other flexible packaging materials. etc.

3. REALIZATION AND EXPERIMENTATION OF CYBER-MIXMECHATRONIC SYSTEMS WITH APPLICATIONS IN INDUSTRY AND ECONOMY

It was thought the new complex concept cyber mixmechatronic and also created the concept of constructive architecture of new solutions for mechatronic cyber systems and integrated intelligent control for the automobile industry and respectively for cast auto parts and machined auto parts. In the architecture of the cyber-mixmechatronic architecture an important role is played by smart software sensors integrated into an assembly comprising pre-processing information modules, signal conditioning modules, feature extraction modules, fault detection,

calibration and reconfiguration modules and IT & C modules, as follows:

- the initial stage of preprocessing converts the signal into a unit of applied engineering, including basic filtering algorithms of anti-duality, noise rejection and improved signal-to-noise ratio with calibration, normalization and (temperature) compensation algorithms;
- the calibration process may include signal linearization using a simple approach by searching the table using the coefficients stored in the data sheet of electronic sensors;
- the linearization alternative technique involves summing a mutual feature of a sensor signal;
- the additional features offered by the calibration procedure include removal of the sensor polarization;
- the calibrated signals pass through a signal conditioning module software to attract a number of features that characterize data;
- the feature extraction is a process to obscure information derived during the "history" signal sensor information that is useful both as output and as part of the research strategy of defects;
- the derivatives are a component of the main features of self-diagnostics and fault detection;
- communicating information to sensors management uses sets of error codes based on electronic mechanisms and sets of software and IT & C hardware;
- etc.

Figure 1 is a block diagram of an intelligent mechatronic system for measurement and integrated control with the main functional modules and the link between them:

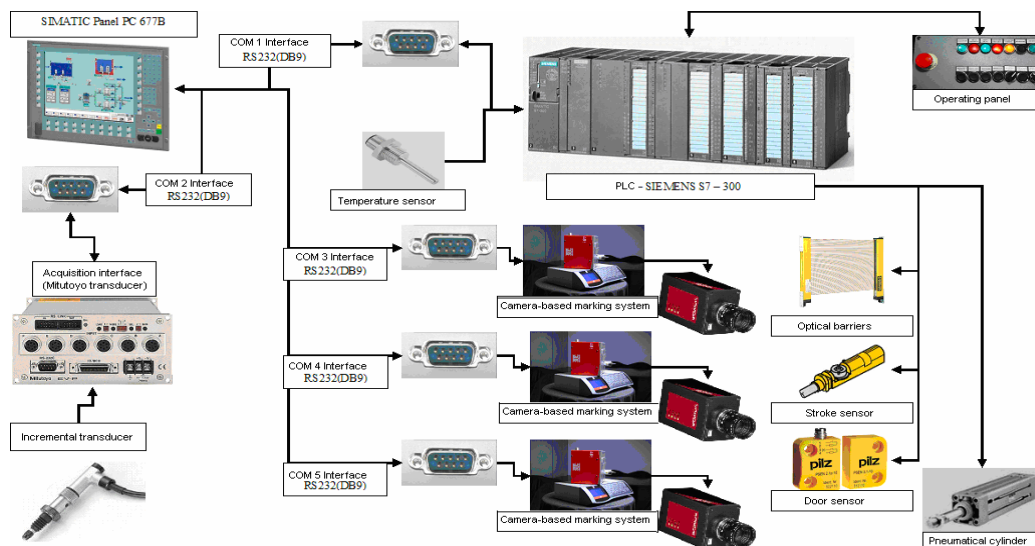


Fig. 1 Block diagram of an intelligent mechatronic system for measurement and integrated control

Figure 2 shows the complex system intelligent mechatronic with three offices (two for measurement and one for marking) for measurement and control of parts.



- Legend:
- 1 – PC with display application;
 - 2 – Optical protection barrier;
 - 3 – Measuring office 1;
 - 4 – Measuring office 2;
 - 5 – Measuring office 1;
 - 6 – Light beam;
 - 7 – PLC;
 - 8 – Sensor interface;
 - 9 – Control panel;

Fig. 2. Complex system intelligent mechatronic for measurement and control of auto parts

We will present further a few other examples of such type of smart ultra-precise mechatronic systems of parts in the automotive industry as follows:

Figure 3 shows Intelligent control system - "crankcase oil S2G Raw":



Fig. 3

The Intelligent control system is based on pneumatic measuring principle, also based on the comparison with a "standard air room" that has two offices of intelligent control and one office of laser marking for part corresponding to standards; it has a complex mechatronic structure of ultra precise sensor and actuator architectures with automated functioning and coordinated by a special and adapted software).

4. SMART ARCHITECTURES OF THE PHYSICAL (MECHATRONIC) SYSTEM AND VIRTUAL (IT&C) SYSTEMS

In Figs. 4 and 5 are presented the smart physical (mechatronic) architectures and virtual (IT&C) architectures, along with data systems:

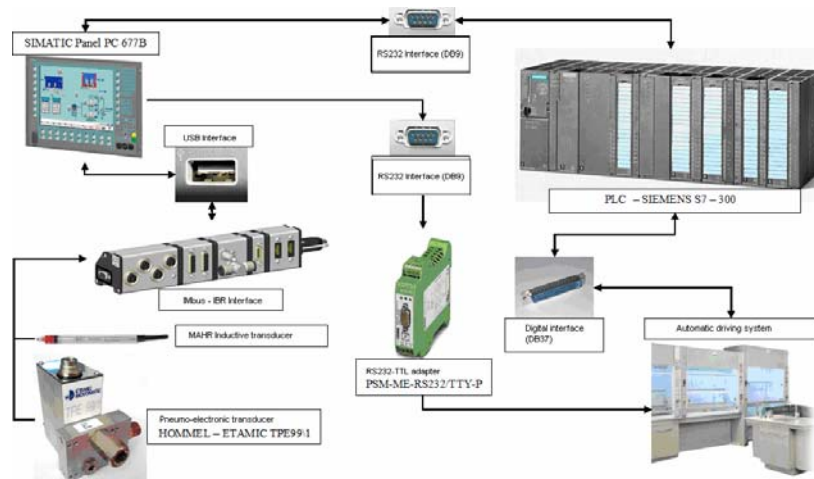


Fig. 4

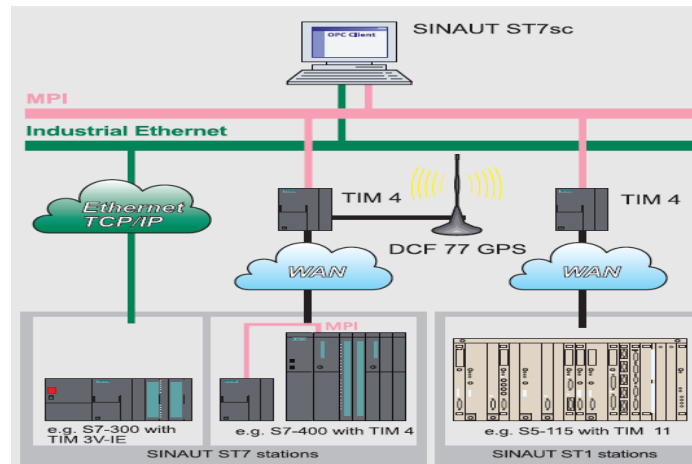
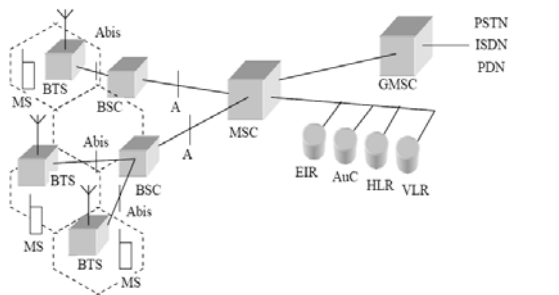


Fig. 5

Along with intelligent architectures, aims to collect data, in which case it is considered that the management system is placed away from the driven process. Thus, the actuators receive control signals via the communication network while the data acquired from the

process by sensors and transducers are also directed to the controller through the network.

Data services are monitored by the GSM communications system, whose architecture is shown in Figure 6, as follows:



Legend:

- | | | | |
|------|------------------------------------|------|-------------------------------------|
| BTS | Base transceiver station | VLR | Visited location register |
| BSC | Base station controller | EIR | Equipment identity register |
| BSS | Base station subsystem (BTS + BSC) | AuC | Authentication center |
| MSC | Mobile services switching center | PSTN | Public switched telephone network |
| GMSC | Gateway MSC | ISDN | Integrated services digital network |
| MS | Mobile station | PDN | Public data network |
| HLR | Home location register | | |

Fig. 6

For the remote monitoring (remote control, remote service or remote configuration) process, in the architecture of multi-application smart mechatronic systems are also integrated other additional systems such as:

- Active components for connecting the (PROFIBUS)

network with the network of the Wireless industrial environment (IWLAN / PBPN IO mode that supports antennas type IWLAN and WLAN, etc.):

- Active components for connecting the (PROFIBUS)network-DP slave, to the AS-I interface (Figure 7-example of how to use a DP / AS-I module);

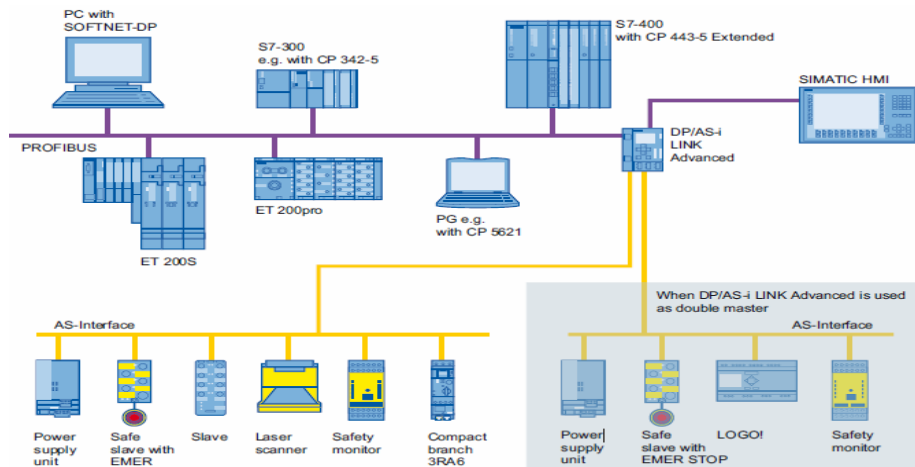


Fig. 7 Example of using a DP/AS-I module

In Figure 8 is given an example of linking to internet WAN for remote monitoring the process and the system:

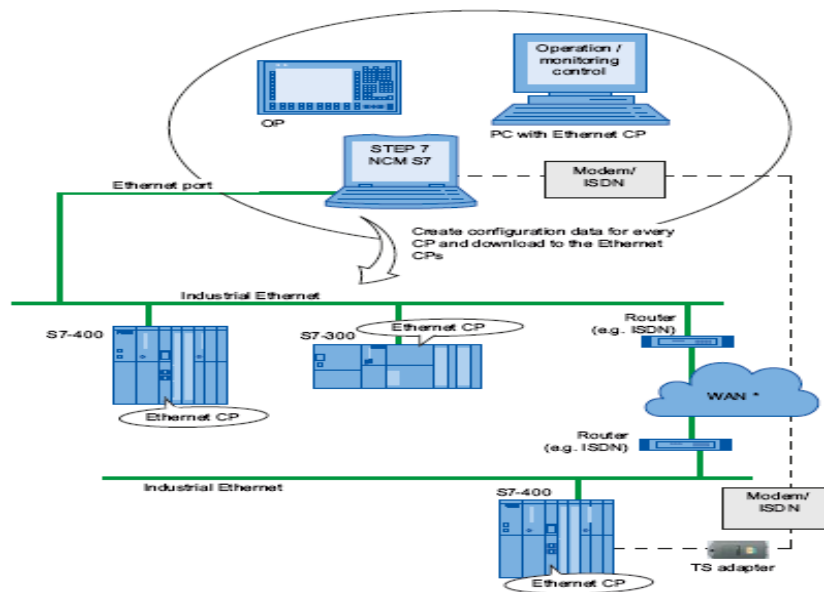


Fig. 8 Example of linking to internet WAN for remote monitoring the equipment

In Figure 9 is given the block scheme of remote monitoring and remote configuration of GPS-GPRS and Internet:

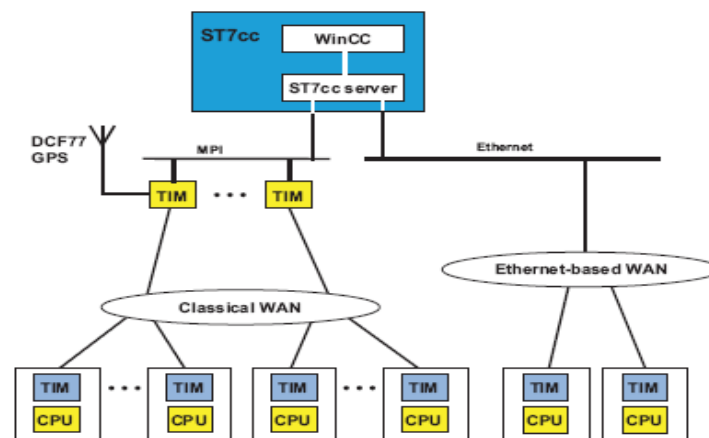


Fig. 9 Block scheme of remote monitoring and remote configuration of GPS-GPRS and Internet

The remote monitoring and remote service software on a PC platform is written in Visual C++ and uses modem configured "as a client" that connects to the cyber-mechatronic system monitored using a RS232 connection.

Thus, in Figure 10, is presented a screen capture of the software in which are positioned the signs (1)-representing the state of inputs number [xx bitwise, the validation controllers (2)-checkbox that easy means by which the user you can set or reset the desired output Q++, the sign (3)-representing the current values of the digital outputs Q++, the button (4) that is pressed to achieve connecting the application of the cyber-

mechatronic system to the monitor, the control editing (5) that is supplemented by the number of numeric values to be issued or requested for the actual amount taken from the cyber-mechatronic system monitored, the start address of the publisher (6), which is supplemented by a numerical value between 0 ... 7 specifying the address of the first model IO selected "board" command in the list (8), select the user for reading digital outputs and all the user completes the starting address in the editor (6) and the number of bytes editor (5). The message is transmitted by cyber-mechatronic system (see Figure 11) monitored and feedback is displayed through signs of type (1).

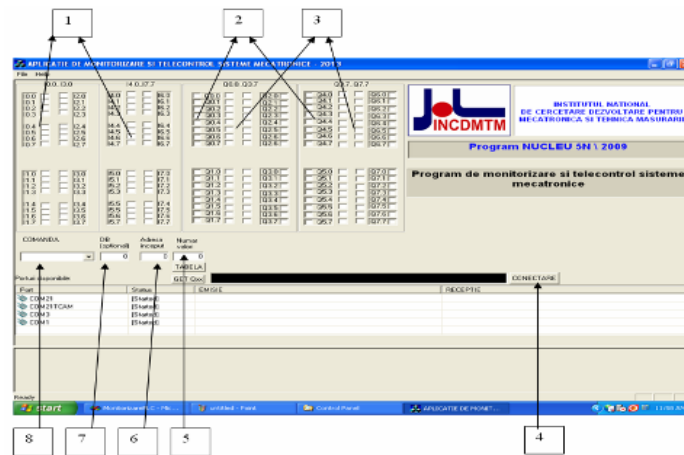


Fig.10

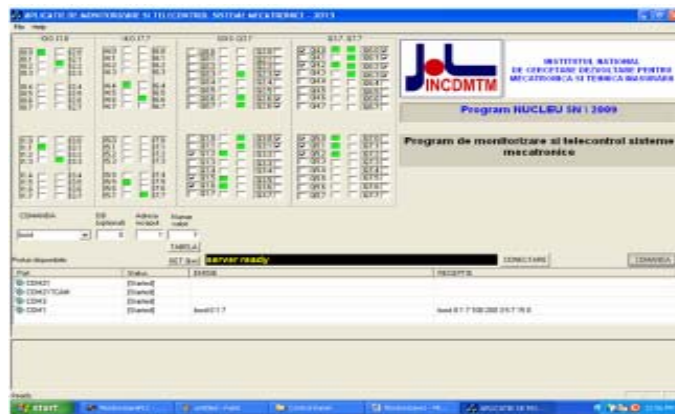


Fig. 11

For writing digital outputs, the user selects the command list (8) and completes the starting address in the editor (6) and the number of bytes in the editor (5). Next, the user actuates the button (9), pressing an editable table (11) (see Figure 12). The number of columns equals the number of output value bytes of which shall be transmitted to cyber-mixmechatronic system monitored. In every column of the table, the operator can enter

numeric values between 0 and 255. You can use a method in a more elegant way: the operator selects or resets, as desired, each bit of Oxxx configuration using validation checks type (2) and then acts on button (10). The numerical values of each byte of output assembled are in the appropriate box. The command message is sent to the cyber-mixmechatronic system monitored (Figure 12), and feedback is displayed through indicators type (1).

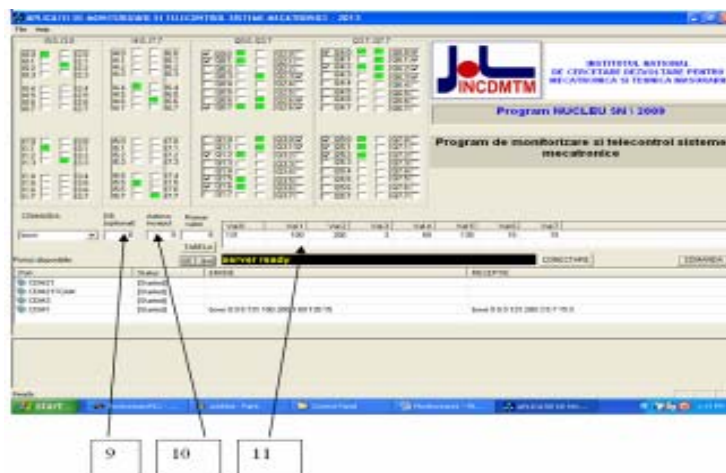


Fig. 12

5. NEW CONCEPTIONS OF MULTI-INDUSTRIAL PROCESSES AND LABORATORY APPLICATIVE CYBER-MIXMECHATRONIC PROCESSES

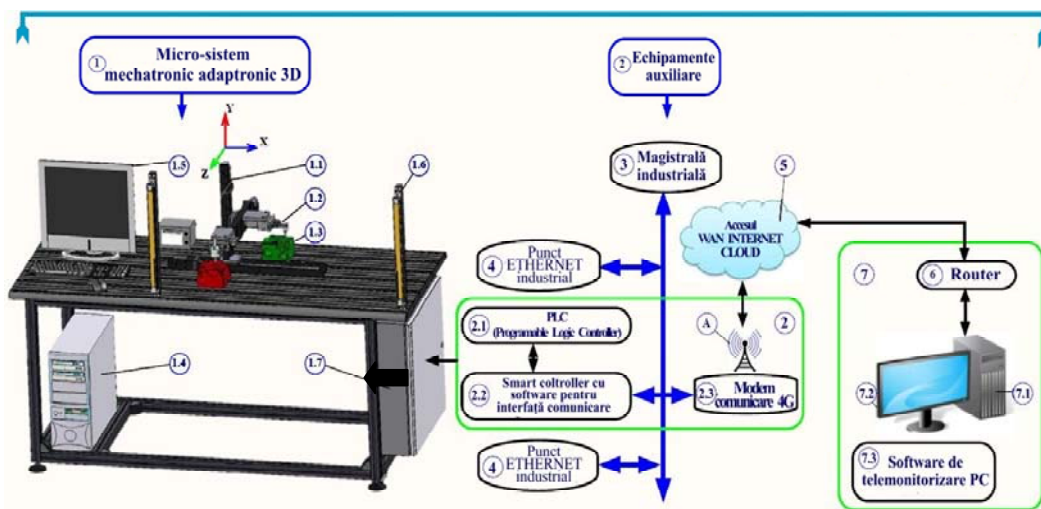
The Presentation of a cyber - mixmechatronic system adaptive to process measurement and control system 3D is configured in Figure 13.

The new complex mechatronic, cyber mechatronic and / or cyber-mix-mechatronic concept created and developed by the author, was implemented in the construction of 3D smart cyber-mechatronic and / or cyber- mix-mechatronic systems for remote control, monitoring the performance of several functions (specific new concept) and ultra precise 3D remote control and adaptive appropriate environment control (metrology laboratory / industrial metrology), for transmission and transfer of data remotely (remote control according to IEC 60870-5-104), remote monitoring / remote monitoring process, and smart

control through a command centre (for 3D ultra precise process control) and transfer of information through the Internet and Intranet by means of remote monitoring.

Following is the concept of a 3D Multi-application smart remote control and remote monitored ultra precise cyber mix-mechatronic system used in the metrology laboratory or industrial metrology (Figure 13).

The smart remote control and remote monitored ultra precise cyber mix-mechatronic system is aimed at achieving the control of movement functions X, Y, Z and measurement function (control) based on information from the system and from the " Highly precise 3D probe " button embedded in the designed system.



Legend:

- | | |
|--|--|
| <ul style="list-style-type: none"> 1. 3D cyber-mix-mechatronic system: 1.1 Ultra-precise 3D measuring system / measuring robot / ultra precise control robot (x=300mm; y=200mm; z=250mm; accuracy:0.1-1nm); 1.2 3D ultra precise probe (accuracy: 0.1 nm); 1.3 Control / measurement part; 1.4 PC local host; 1.5 Display and local user interface; 1.6 Laser protection barrier 1.7 Unit with command system, driving system and telecommunications system; | <ul style="list-style-type: none"> 2. Auxiliary equipments: 2.1 PLC (Programmable Logic Controller); 2.2 Smart controller with software for communication interface; 2.3 4G communication modem; 3. Industrial BUS; 4. Industrial ETHERNET point; 5. WAN INTERNET CLOUD access; 6. 802,1 lb/g router 7. Control Centre 7.2 PC Display 7.3 PC Remote monitoring software |
|--|--|

Fig.13 Remote control and remote monitored ultra precise cyber mix-mechatronic system

In the 3D mode of travel, the cyber-mix-mechatronic system is designed to be operated locally using a program preinstalled on PC equipped with display and control software and modeling and emulating remote position. Switching between the two operating modes can be done anytime and measurement (3D control) points may be stored in the memory functioning in the automatic PLC mode.

Thus, all these complex functions may be implemented by integrating several functional testing and smart subsystems.

The overall block diagram of the ultra precise cyber-mix-mechatronic system, shown in figure 13 depicts the

componential mix-mechatronic structure & the functional cybernetic presentation below:

- **On the local unit PC (1.4)** are collected data from the 3D Mechatronic System and they are transmitted to the SMART TELECONTROL system. The data provided by SMART TELECONTROL will be wrapped, compressed and protected by a VPN server private key. After establishing bidirectional communication with the remote monitoring system, they will be sent and accepted based on CRC checksums. After unpacking the package, the information gathered will be included in a database which will analyze the components of the cyber-mix-mechatronic micro-system.

Besides all these data into the database will be inserted also in the rangefinder system positions that will be replicated using remote monitoring software desktop. Based on this information, the software will generate a 3D image with maximum accuracy depending on how much data is received, and where there are not enough data, the previous data is interpolated to generate a more fluent. On request provides the possibility of saving the session and the image generated for use and analysis. The micro-cyber-mix-mechatronic system can be controlled in real time by using remote control software.

• **Connections and interconnections** between modules and sub-systems architecture components of the system (system of systems) differ depending on the type. The 3D mechatronic system and the 3D ultra precise probe (with nanometer precision and sub-nanometer accuracy) can be fitted if necessary with smart data transmission cables such as serial cable, parallel cable, CAN, PROFIBUS, SSI, Interpose, Ethernet, Device Net, and other specialized types.

• **The cyber-mix-mechatronic 3D (1)** is an absolute novelty in Romania, not far approached this field clever conception and realization.

• **The Programmable Logic Controller-PLC (2.1)** is a digital computer used for automation of cyber-mix-mechatronic systems to be used for storing the specific control program of the 3D micro-system (with axes X, Y, Z or robot control) to synchronously receives information from the probe in 3D.

This controller is designed for multiple inputs and outputs for use in an extended temperature range and to withstand vibration generated by the machines they control kinematics and accidental impact caused by various factors. The control program is generally protected by a copy or stored on a non-volatile memory. PLC is a system in "real time" as it outputs must be produced in response to input conditions within a limited time, otherwise unintended operation will occur that will result in undesired results. The PLC is programmed in graphic language ("ladder logic") notation used for programming being chosen so as to reduce programming time.

• **The module for achieving smart remote control (2.2)** can be implemented either with RISC microcontroller or FPGA microcontroller and will link the PLC and the 4G telecommunication modem using a specific RS232 protocol.

• **To access the 4G connection (2.3)** the system will use different public or private networks. In order to ensure the connection there are a variety of modems (2.3) compatible with RS232 data protocols. Event-driven type processing or cyclic data processing is performed using special protocols allowing remote operating personnel to control and effectively managing the process as a whole

or in detail. One or more software platforms developed can be used for connecting remotely, based on modern GPRS technologies or Internet global WAN network with PLC control system often used in other mechatronic automation equipment.

• **In the remote control Centre (7)** ensures Internet connection (5) using a router equipped with the VPN to provide a first level of data security. A 2nd level of security will be studied by using a proprietary algorithm and an encryption function for the FIREWALL specific configuration of the operating system on your PC (Windows or Linux). Scheduling an application on the network requires an RTOS (Real Time Operating System), which is offered by Dream DSP ++ kernel by VDK. This is a multitasking kernel, which incorporates mechanisms for planning and resource allocation compatible with the memory space and time constraints required by Blackfin programming process. Other facilities are VDK development of powerful applications using templates (such as the implementation of applications TCP / IP).

• **The software (7.3)** is a web application for remote controlling desktop that can be considered as two separate components: a web service and PHP front-end remote control software with real-time emulation capability. PHP Web Service is responsible for integrating telemetry database back-end and front-end and returning results from performing the remote control function in the format.

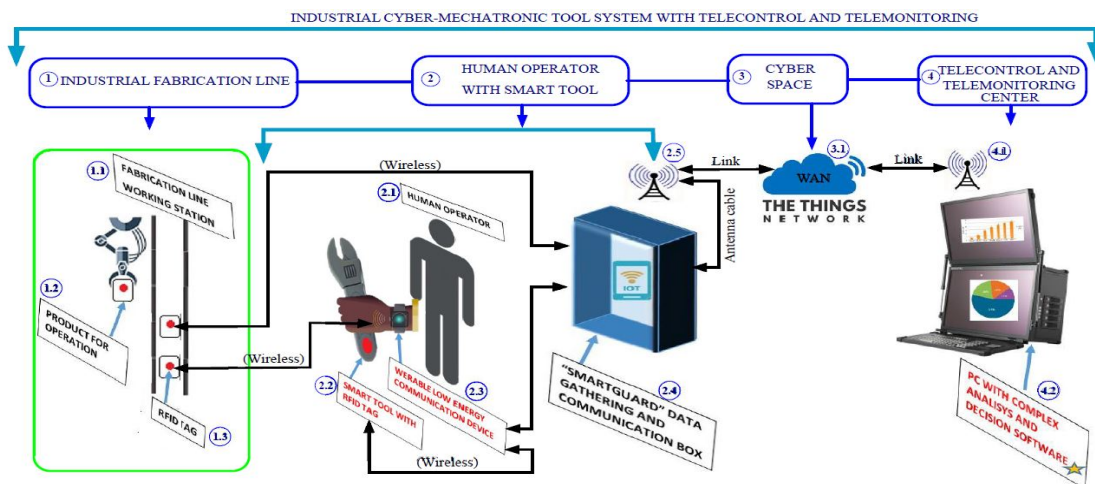
To minimize the amount of data that is transferred to the front-end in real time it will be necessary to request data only for mechatronic measurement regime. After receiving the front-end data the remote control software generates a virtual model in real-time of the 3D mix-mechatronic cyber emulated system.

• The structural component of the testing notions of the evaluation and validation of the mix-cyber-mechatronic system aim to ensure a final configuration of the system developed so that it meets the initial requirements and specifications. To meet this goal, the following aspects must be detailed:

- determining the criteria for testing, evaluation and validation of the 3D cyber-mix-mechatronic system;
- description of categories of tests and evaluations involved;
- planning tests and assessments within the period of development of the mechatronic system;
- preparation of the mechatronic system for testing and evaluation.

The presentation of another industrial cyber-mixmechatronic system for protecting against human

error in smart fabrication lines, using remote control and remote monitoring capabilities is configured in Figure 14.



- Legend:
- | | | | |
|--|---|------------------|--|
| 1. Industrial manufacturing line | 2. Human operator with smart instruments | 3. Cyber space | 4. Remote control and remote monitoring centre |
| 1.1 Workstation on the fabrication line | 2.1 Human operator | 3.1 Internet WAN | 4.1 Antenna |
| 1.2 Product for technological applications | 2.2 Unique identification system with RFID | | 4.2 PC with software for complex analysis and decision |
| 1.3 Unique identification system with RFID | 2.3 Smart communication and warning bracelet | | |
| | 2.4 Unit with system for data acquisition and communication | | |
| | 2.5 Antenna | | |

Fig. 14

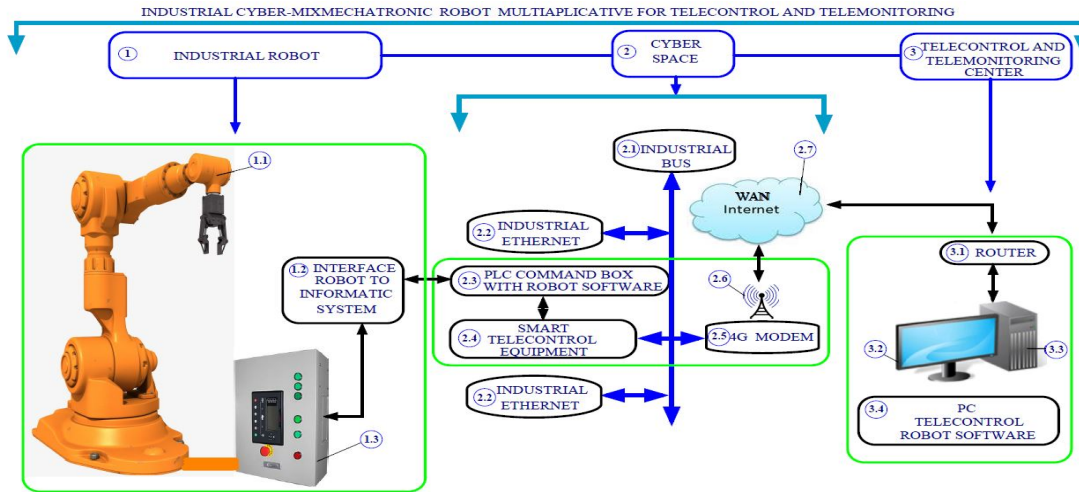
According to the above mentioned Figure, the structure of the physical matrix [Mechatronics and Cybernetics (IT & C)] of the system allows remote automation and computerization remote control and remote monitoring) in the industrial line of manufacturing.

The system performs the function of protecting workstations from human errors specific to fabrication lines (1.1) in the series in the industry, such as automotive parts in the manufacturing industry. Parts (1.2) call feature tags with unique ID RFID (1.3) communicating bi-directionally with a drive (2.4) with automation equipment and telecommunication local but also a smart bracelet (2.3) situated on the hand of the operator who is using the device (2.2) equipped with RFID tag and bidirectional communication.

Intercommunication between elements listed (part, device, operator) is collected and transmitted using antennas (2.5) and (4.1) through the Internet to a (4.2) computing station at the center of remote monitoring and remote control (4).

The computer center remote monitoring and remote control (4.2) running special software designed to synchronize tasks on a database technology and eliminate errors caused by real-time tracking and manufacturing through a comprehensive analysis and forecasts.

Presenting another complex smart multi-application cyber-mixmechatronic device type industrial robot for remote control and remote monitoring of operational and service processes is configured in Figure (15).



- Legend:
- | | | |
|--|---|---|
| 1. Industrial robot | 2. Cyber space | 3. Center of remote control and remote monitoring |
| 1.1 Universal robotic arm (with gripper / 3D feeler) | 2.1 Industrial communication bus | 3.1 Router linking to WAN Internet |
| 1.2 Interface between the robot and the informatic environment | 2.2 Industrial ETHERNET network | 3.2 PC monitor |
| 1.3 Command tools | 2.3 Programmable PLC with ROBOT software | 3.3 Central unit |
| | 2.4 Smart devices for remote control and remote communication | 3.4 UPC with ROBOT remote control software |
| | 2.5 4D GPRS modem | |
| | 2.6 Internet WAN | |

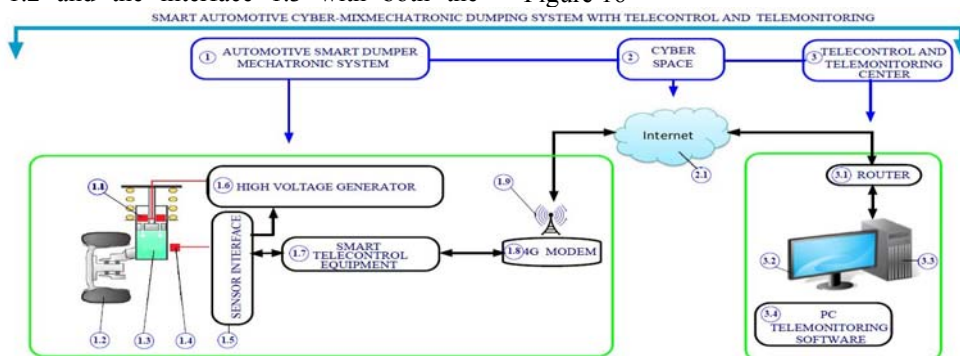
Fig. 15

According to the above mentioned figure, the structure of the physical matrix [Mechatronics and Cybernetics (IT & C)] of the system allows the cybernetization and remote communication of technological operational processes and of processes that service the industry, thus contributing to a higher increase in productivity and of quality of smart industrial. The cyber-mixmechatronic multi-application system performs a remote control and remote monitoring of an industrial robot (1) connected to the cyberspace via the control unit 1.2 and the interface 1.3 with both the

internal industrial bus (2.1) and Internet via a 4G GPRS modem.

Through this communication connection is made the link to a centre of remote control and remote monitoring (3) provided with a computing station (3.2) and (3.3) connected to the router (3.1) and running specialized software for robot control (3.4).

The presentation of another cyber-mixmechatronic system for dampening for automotives and with remote control and remote monitoring functions is configured in Figure 16



- Legend:
- | | | |
|---|------------------|--|
| 1. Smart cyber mix-mechatronic system for dampening | 2. Cyber space | 3. Centre of remote control and remote monitoring |
| 1.1 Electromagnet or coil | 2.1 Internet WAN | 3.1 Router linking with WAN Internet |
| 1.2 Section of a tire | | 3.2 PC monitor |
| 1.3 Rheological fluid | | 3.3 Central PC unit |
| 1.4 Acceleration sensor | | 3.4 PC with software for remote monitoring and remote control smart DAMPER |
| 1.5 Interface between sensor and acceleration | | |
| 1.6 High tension source | | |
| 1.7 Smart remote control device | | |
| 1.8 4D GPRS modem | | |
| 1.9 Antenna | | |

Fig. 16

According to the above figure, the structure of the physical matrix (damper and cybernetics (IT & C) of the cyber-mixmechatronic system for dampening for automotives allows the smart computerization and cybernetization of the automotive and of the automotive industry, by raising the quality and increasing productivity of the automotive industry.

The cyber-mixmechatronic system for dampening for automotives allows the function of remote monitoring and remote control of a smart damper (1) provided with an electromagnet (1.1) powered by a high voltage source (1.6) in order to modulate the degree of viscosity of the rheologic fluid (1.3).

To obtain information on the global acceleration of the cyber-mechatronic assembly attached to a tire of a vehicle uses the sensor (1.4) and the interface (1.5) connected to an intelligent control and remote control equipment (1.7).

Internet WAN network connection is performed using a specialized 4G GPRS modem (1.9) provided with an antenna (1.8).

Through this communication connection is made the link to a centre of remote control and remote monitoring (3) provided with a computing station (3.2) and (3.3) connected to the router (3.1) and running specialized software for robot control (3.4).

6. CONCLUSION

This scientific paper aims to present "The New Complex Multi-application Cyber - Mixmechatronic Concept " used in the construction of "Ultra precise Cyber-Mixmechatronic Systems for 3D Smart Control" for laboratory metrology processes and / or industrial processes (in the automotive industry, aerospace industry, hydronic and pneumatic industry , medical and biomedical industry, etc.).

Cyber-mixmechatronic systems in coordinates, in the conception of the authors, are an absolute novelty in Romania, addressing for the first time this complex cyber-mixmechatronic concept and designed to perform the functions of 3D remote control and remote monitoring in the process of measurement and / or in the smart industrial process through signals and information on Cartesian X,Y,Z travel and ultra precise rotation travel ψ_1 , ψ_2 , ψ_3 and probe measurement / control in 3D and of the software preinstalled on your PC and the software of control and modeling and remote position emulation so " position-touch information packets " will build "packages of vectors" for complex mathematical processing that can be done both locally and remotely.

7. REFERENCES

[1] Zaharescu, M., Ciurea, M., Kleps, I. și Dascălu, D: Nanostructuring and Nanocharacterization ISBN 978-973-27-1905-3, 2010, Editura Academiei Române;
 [2] Fijalkowski, B. T.: Automotive Mechatronics: Operational and Practical Issues, vol.II ISBN 978-94-007-1183-9, Editura Springer- Germania;

[3] Saikalis, G. et al.: Virtual Embedded Mechatronics System, SAE Technical Paper, 2006, ISBN: 2006-01-0861;
 [4] Zhou, K., Ye Cen, Wan J., Liu B. and Liang L.: Advanced Control Technologies in Cyber-physical System, 5th International Conference on Intelligent Human-Machine Systems and Cybernetics (INMSC), Aug. 2013, doi: 10.1109/IHMSC.2013.284.
 [5] Gheorghe, Gh.: Mecatronica & Sistemele Cyber – Mecatronice, ISBN 978-606-8261-22-5, 2015, Ed. CEFIN – Romania;
 [6] Gheorghe, Gh (RO), Stiharu, I. (Canada): Nano Ingineria, ISBN: 978-606-8261-16-4, 2011, Ed. CEFIN- România;
 [7] Rizescu C. I., Ciocan M. and Rizescu D., Robot Control for Home Application, Applied Mechanics and Materials Vol. 332 (2013) pp 145-153, ISSN 16609336, ISBN (978-3-03785-733-5) DOI: 10.4028/www.scientific.net/ AMM.332.145
 [8] Machado, Jose; Soares, Filomena; Leao, Celina P.; et al., A Virtual Workbench Applied to Automation: Student's Response Analysis, Control'2014 – Proceedings of the 11th Portuguese Conference on Automatic Control Vol: 321, Pages 709-719, Published: 2015, Times Cited: 0; DOI:10.1007/978-3-319-10380-8_68;
 [9] Machado, J.; Campos, J. C.; Sevcik, L; et al., Development of Dependable Controllers in The Context of Machines Design, Modern Methods of Construction Design, Pages:125 - 131, Published: 2014, DOI: 10.1007/978-3-319-05203-8_18;
 [10] Silva, M.; Pereira, F.; Soares, F.; et al., An Overview of Industrial Communication Network, New Trends in Mechanism and Machine Science from Fundamentals to Industrial Applications, Vol. 24, Pages: 933-940, Published: 2015, DOI:10.1007/978-3-319-09411-3_97;
 [11] M, Avram; V, Constantin; C. Rizescu: " Speed and position control for a hydraulic rotary motor", The Romanian Review Precision Mechanics, Optics & Mechatronics, 2014, No. 45, pag. 63-67, ISSN: 1584 – 5982§
 [12] O, Donțu, ș.a: "Influence of thermal deformations in the solid laser medium on the emitted radiation parameter", Journal of Mechanical Engineering, Aug 2005, Vol. 219, No. C8, pag. 823-829;
 [13] Labo, Edgar; Machado, Jose; Mendacos, Joao, P: Development of Controller Strategies for a Robotized Filament Winding Equipment", 11th International Conference in Numerical Analyzes and Applied Mathematics, 2013, Pts 1 and 2, Volume: 1558 Pages: 1037-1040, 2013
 [14] Lee, E. A. *Cyber-physical systems design challenges*. International Symposium on oriented items/ components/ services distributed using real-time computational technique (ISORC), Orlando, FL, pp. 363-369.
 [15] Lee, E. A.. *Are cyber-physical systems fundamentals of adequate calculus?* FSN Workshop on cyber-physical systems: Motivation of research, Techniques and Roadmap, Austin, TX.
 [16] Lee, E.A.. *CPS fundamentals in the Proceedings of Automation Design Conference. (DAC 2010), Association for Computing Machinery*, Anaheim, CA, pp. 737-742.
 [17] Campbell, R.H., Garnett, G. and McGrath, R. E. *Cyber-physical systems: CPS position document - environments*. Cyber-physical systems, National Science Foundation, Austin, TX. Available at: <http://varma.ece.cmu.edu/cps/Position-Papers/Roy-Campbell.pdf>.
 [18] Campbell, J., Goldstein, S. & Mowry T.. *Cyber-physical systems*, National Science Foundation, Austin, TX. Available at: <http://varma.ece.cmu.edu/cps/Position-Papers/Goldstein-Mowry-Campbell.pdf>.
 [19] West, R. & Parmer, G.. *A software architecture for next-generation cyber-physical systems*. Cyber physical systems,

- National Science Foundation, Austin, TX. Available at: <http://varma.ece.cmu.edu/cps/Position-Papers/richard-west.pdf>.
- [20] Kornerup, J.. 2006. *A vision for overcoming the challenges of building cyber-physical systems*. Cyber-Physical Systems, National Science Foundation, Austin, TX. Available at: <http://varma.ece.cmu.edu/cps/Position-Papers/Jacob-Kornerup.pdf>.
- [21] Rajkumar, R., Lee, I., Sha, J., Stankkovic, & J.. *Cyber-physical systems: The next revolution calculation of the Design Automation Conference (DAC 2010)*, Association for Computing Machinery, Anaheim, CA
- [22] Gheorghe, I. Gh., *Mechatronics and Cyber-Mechatronic Systems*, ISBN 978-606-8261-22-5, CEFIN Publishing House, 2015;
- [23] Gheorghe I. Gh., *Adaptronica Micro-Engineering*, ISBN 978-606-8261-21-8, CEFIN Publishing House, 2014;
- [24] Gheorghe, I Gh., *Mechatronics & Cyber-Mechatronics & Micro-Nano-Mechatronics & Cyber-Micro-Nano-Mechatronics in smart industrial and societal applications*, International Conference OPTIROB 2016, June 29– July 2, 2016, Jupiter, Romania, ISI quoted; impact factor: 0,15;
- [25] Gheorghe, I. Gh., ILIE I., Anghel C-tin, „*Scientific Evolution from Mix-Integrative Mechatronics to Smart Cyber-Mechatronics and towards Claytronics*”, International Conference OPTIROB 2016, June 29 – July 2, 2016, Jupiter, Romania, ISI quoted; impact factor: 0,15;
- [26] Gheorghe, I. Gh., „*From Mechatronics to Cyber-Mechatronics and from µMechatronics to Claytronics*” International Conference - ACME 2016 „Advanced Concepts in Mechanical Engineering”, 09–10 iunie 2016, Iași, Romania;
- [27] Gheorghe, I. Gh., „*From Mechatronics to Cyber-Mix-Mechatronics and in the future to Claytonics*”, Annual Scientific Session of professors and researchers of University Valahia, June 2, 2016, Târgoviște, România;
- [28] Spânu, A.R., Donțu, O., Besnea, D., Avram, M., *Improvements on Design of Propeller for Chemical Compound Mixer*, REVISTA DE CHIMIE, Volume 66, Issue 3, pp. 422-425, ISSN 0034-7752, 2015 (ISI Web of Science, IF=0,810);
- [29] Spânu, A.R., Besnea, D., Avram, M., Constantin, V., „*Laser mechatronic system used for accurate measurement of spatial shapes*”, Optoelectronics and Advanced Materials - Rapid Communications, Volume 8, Issue 1-2, pp.1-6, ISSN 1842-6573, 2014 (ISI Web of Science, SCOPUS, IF=0,394);
- [30] Nitu, C., Nitu, S., Gramescu, B., „*Application of Electromagnetic Actuators to a Variable Distribution System for Automobile Engines*”, Journal of Materials Processing Technology, vol. 161/1-2, 200, 5pag. 253- 257, Elsevier, ISSN 0924-0136 (ISI Web of Science -WOS:000229375200046) - impact factor 2.236 – 8 citations;
- [31] Nitu, C., Nitu, S., „*An Improved Analytical Model for Electromagnetic Actuators Design*”, in “Elektronika” nr.8-9/2004, pag.47-49, ISSN 0033-2089, Varsovia (INSPEC);
- [32] Nitu, C., Comeaga, C.D., Gramescu, B., „*Micropositioning devices for optical applications*”, Proceedings of SPIE, nr. 5227, pag. 355-360, 2002 (Web of Science WOS:000186473500050);
- [33] Lemos, D.; Nunes, A.; Machado, J., „*Mechanical simulation model of the systemic circulation*”; et al., Source: Measurement Volume: 66 Pages: 212-221 Published: APR 2015 Times Cited: 0, DOI: 10.1016/j.measurement.2015.01.026;
- [34] Barros, Carla; Leao, Celina Pinto; Soares, Filomena, „*QR Codes and Java Applied to Physiological Data Acquisition in Biomedical Engineering Education*”, Source: Proceedings of the International Conference of Numerical Analysis and Applied Mathematics 2014 (Icnaam-2014) Volume: 1648 Published: 2015 Times Cited: 0, DOI: 10.1063/1.4912855;
- [35] Rizescu C. I., Ciocan M. and Rizescu D., „*Robot Control for Home Application*”, Applied Mechanics and Materials Vol. 332 (2013) pp 145-153, ISSN 16609336, ISBN (978-3-03785-733-5), DOI: 10.4028/www.scientific.net/ AMM.332.145;
- [36] Rizescu, C.I., Udrea, C. Rizescu, D., „*Experimental Setup for Harmonic Drive Efficiency Determination*”, Advanced Materials Research Vols. 463-464 (2012) pp. 1518-1521, ISSN 10226680, ISBN 978-303785363-4, Accession Number: WOS: 000308114100299, Inspec Accession No.: 13066151, DOI: 10.4028/www.scientific.net/ AMR.463-464.1518.

EXPERIMENTAL RESULTS OBTAINED IN A PROACTIVE MAINTENANCE OF INDUSTRIAL EQUIPMENT OPERATING IN LUKOIL REFINERY

Ionel RUSA¹, Cornel MARIN²

¹BIT INVEST Romania

²VALAHIA University of Târgoviște, Faculty of Materials Engineering and Mechanics

E-mail: ionelrusa@gmail.com, marin_cor@yahoo.com

Abstract. *In the engineering practice, knowing the technical condition of industrial equipment under operating results shortening of repairs, repairs machinery to smart planning based on the time evolution of bearing wear, detect and correct errors on their installation or repair. This is one of the most important objectives of proactive maintenance; maintenance engineer must follow and monitor the wear of equipment with moving parts to prevent damage and removing them permanently from service, ensuring repair costs as low as possible. The aim of this paper is to present a particular case study on vibro- acoustic diagnosis of equipment and components subject to wear during operation to prevent catastrophic damage, as well as human and material losses.*

Keywords: *proactive maintenance, bearing wear, vibro- acoustic diagnosis*

1. INTRODUCTION

Proactive maintenance activities have become a necessity today, even if to start its implementation involves high cost. The software used for surveillance and maintenance planning within the firm LUKOIL produced by "International VMI AB Sweden - SPECTRA PRO" is professional software dedicated to a proactive maintenance program. Proactive maintenance activity aims to limit and eliminate accidental defect, growth productivity in manufacturing equipment, always knowing the technical condition of equipment, planning current and general repairs without affecting the operation of the main installations.

2. PROACTIVE MAINTENANCE OF NEW EQUIPMENT

Example proactive maintenance presented in this article is a case of better functioning of new equipment put into operation after installation and proper alignment of the elements in motion.

This example is an electric pump that serves a supply power having a boiler flow with a capacity 240t / h (shown in Figure 1 and Figure 2); the equipment was installed in March 2015. The main features of this equipment (the electric power - EPA no. 3) are as follows:

- Engine power = 1.7 Mw,
- Supply voltage = 6000 V
- Nominal pump (Q) = 2985 l / min,
- Working pressure = 140 bar,
- Temp water supply > 1500 C

Figure 1 shows the placement of electric motor and pump produced by ELECTROPUTERE Romanian company.

Figure 2 shows the location of the equipment seen from another angle from which we can observe the supply pump and motor, local control panel.



Fig. 1 . The electric motor and pump No. 3



Fig. 2 – The electric motor, local control panel

2.1. Evolution of wear in the bearing No.1.

Figure 3 presents the variation wear of mounted bearing No. 1 measured in units of gravitational acceleration g , depending on the rotation speed of the machine RPM .

According to the four diagrams of Figure 3, the bearing wear of mounted bearing no. 1 is $0.11 g$ - this is a very good value, considering that was acquired after

equipment operating longer than one year (measured on the period 27.05.2015 - 28.06.2016).



Fig. 3 – EPA nr.3 : The bearing wear of mounted bearing no. 1

Standard ISO-10816-3				
Viteza de vibrație mm/s (RMS)	Clasa I Mașini cu putere > 10 Mw	Clasa II Mașini cu putere > 300 Kw	Clasa III Motoare electrice 15 Kw – 75 Kw	Clasa IV Motoare electrice < 15 Kw
0.28	A	A	A	A
0.45				
0.71				
1.12	B	B	B	A
1.8				
2.8	C	C	B	B
4.5				
7.1	D	D	C	C
11.2				
18				
28	D	D	D	D
45				

Fig. 4 – The international standard for vibration ISO - 10816

In order to monitor the status of technical equipment necessary for adequate monitoring / recording and processing vibration levels, which is a method of non-invasive which is achieved through the placement of transducers for measuring vibration levels in three directions: vertical, horizontal and axial.

To determine the technical condition of equipment under operating continuously measured values must be compared with standard values established by the international standard for vibration ISO - 10816.

This standard includes different values of vibration speeds RMS for four classes according to power plant their (Figure 4) colors represented for each area of vibration speeds RMS OVERALL values reflect the

technical condition of equipment: green - very good; yellow - good; orange - carefully; red - failure.

In Figures 5, 6, 7 are bearing mounted on the observed evolution of the wear of the bearing no. 1 values are measured on the period 27.05.2015 - 28.06.2016.

- In the horizontally direction: RMS OVERALL = 1.823 mm/s , the bearing wear = $0.11 g$ (Figure 5). We can observe the trend of variation in amplitude is an almost constant during the period of one year after start up.

- In the vertical direction: RMS OVERALL = 0.438 mm/s , (Figure 6).

- In the axial direction: RMS OVERALL = 0.641 mm/s , (Figure 7). We can observe the trend of variation in time is an almost constant during the same period.

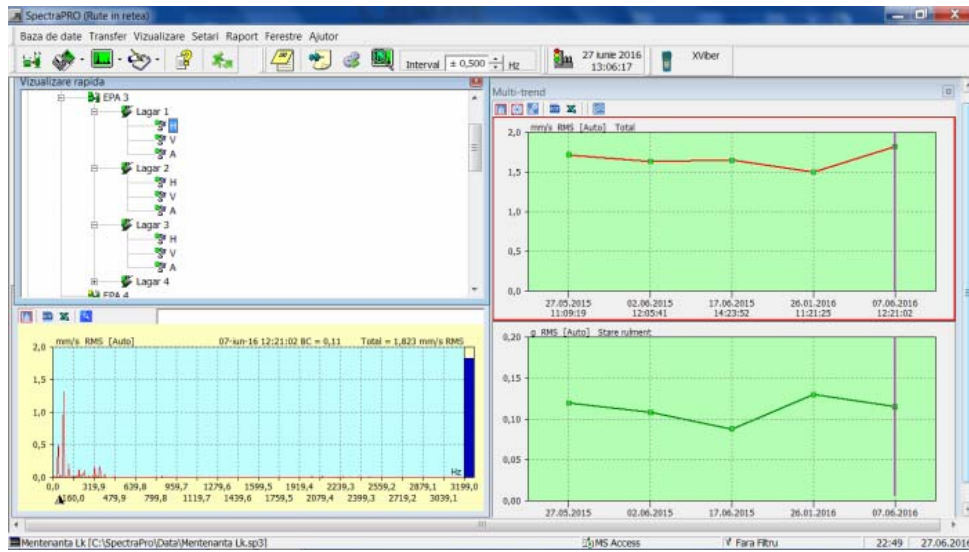


Fig. 5 – EPA No.3 : Bearing No 1- horizontally direction

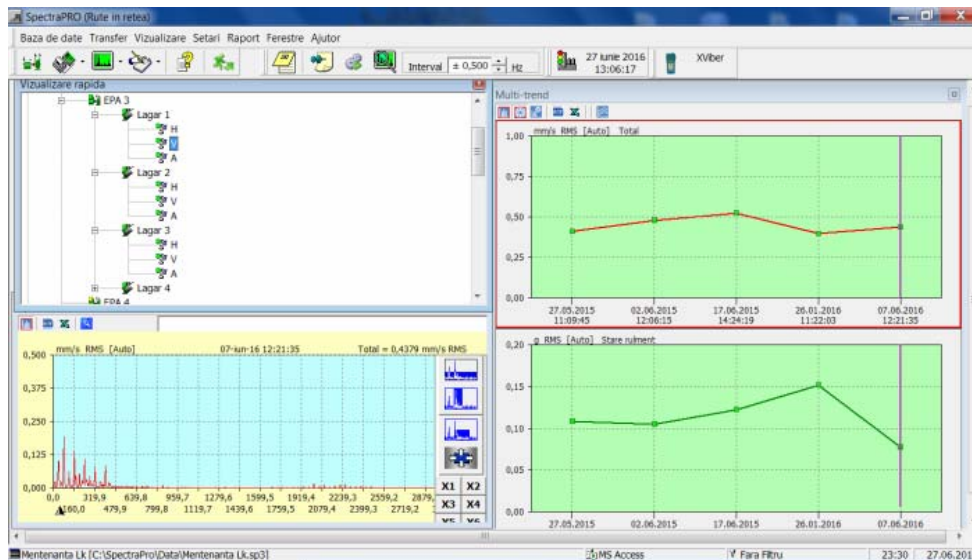


Fig. 6 – EPA No.3 : Bearing No 1- vertical direction

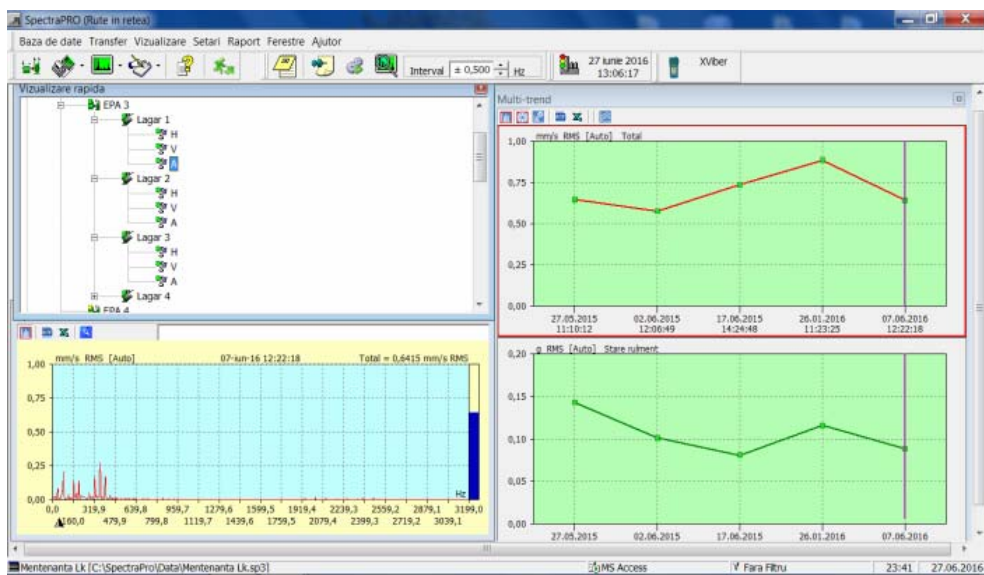


Fig. 7 – EPA No.3 : Bearing No 1- axial direction

2.2. Evolution of wear in the bearing No.2.

Figure 8 presents the variation wear of mounted bearing No. 2 measured in units of gravitational acceleration g , depending on the rotation speed of the machine RPM .

According to the four diagrams of Figure 8, the bearing wear of mounted bearing no. 2 is $0.18 g$ - this is a very good value, considering that was acquired after equipment operating longer than one year (values are measured on 27.06.2016).

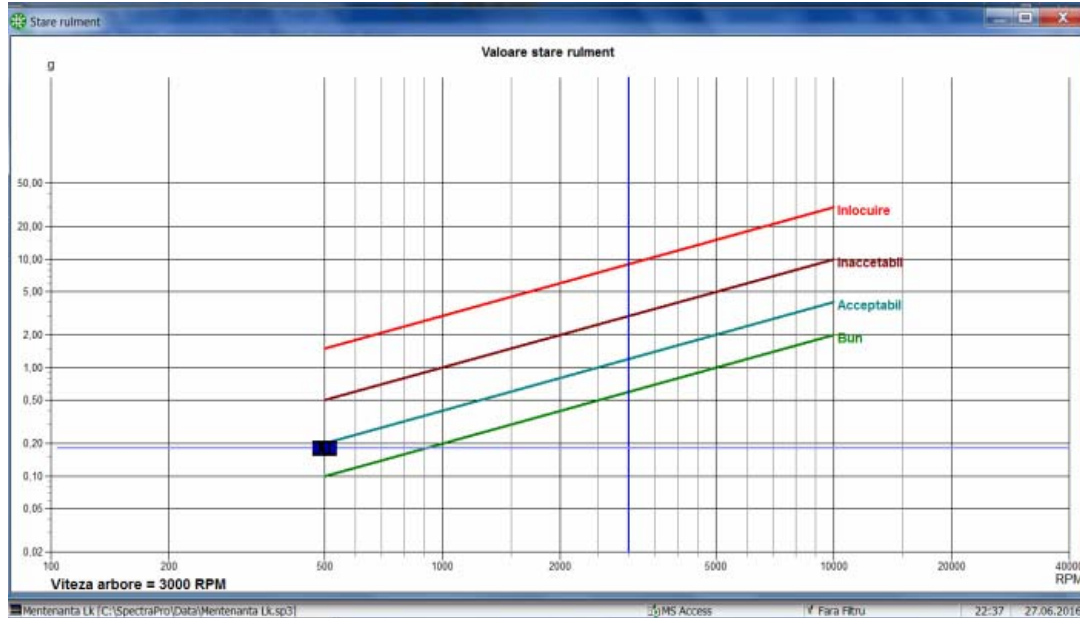


Fig. 8 – EPA No.3 : The bearing wear of mounted bearing no. 2

In Figures 9, 10, 11 are bearing mounted on the observed evolution of the wear of the bearing no. 2 values are measured on 27.06.2016:

- In the horizontally direction: RMS OVERALL=1.015 mm / s, the bearing wear= 0.18 g (Figure 9).

- The vertical direction: RMS OVERALL =0.5005 mm / s, the bearing wear =0.21 g (Figure 10).

- In the axial direction: RMS OVERALL= 0.5479 mm / s, the bearing wear = 0.13 g (Figure 11).

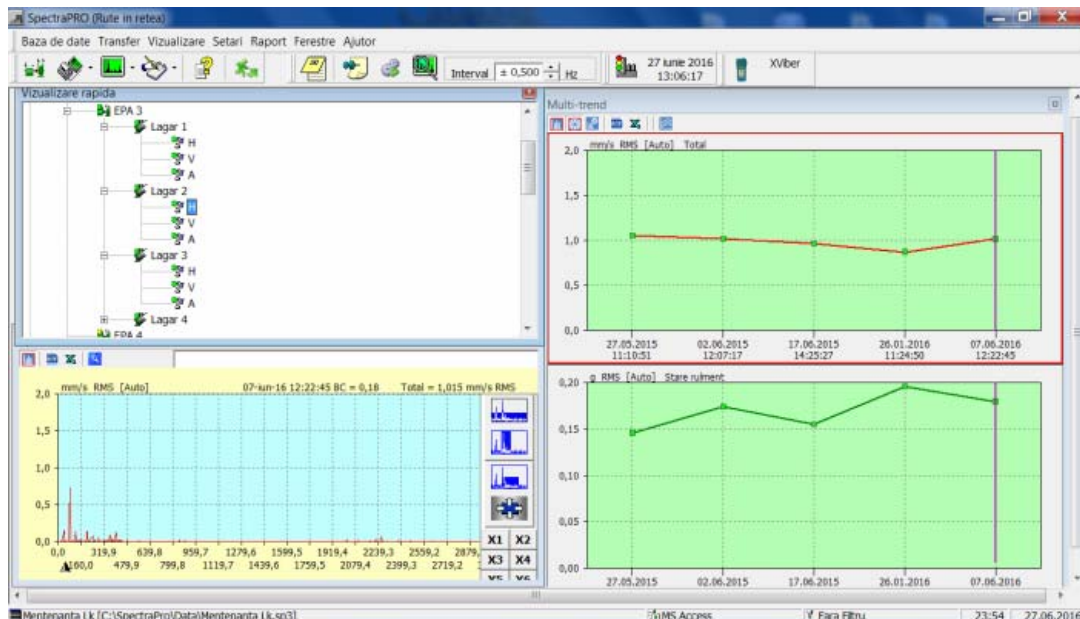


Fig. 9 – EPA no.3 : Bearing No 2 – Horizontally direction

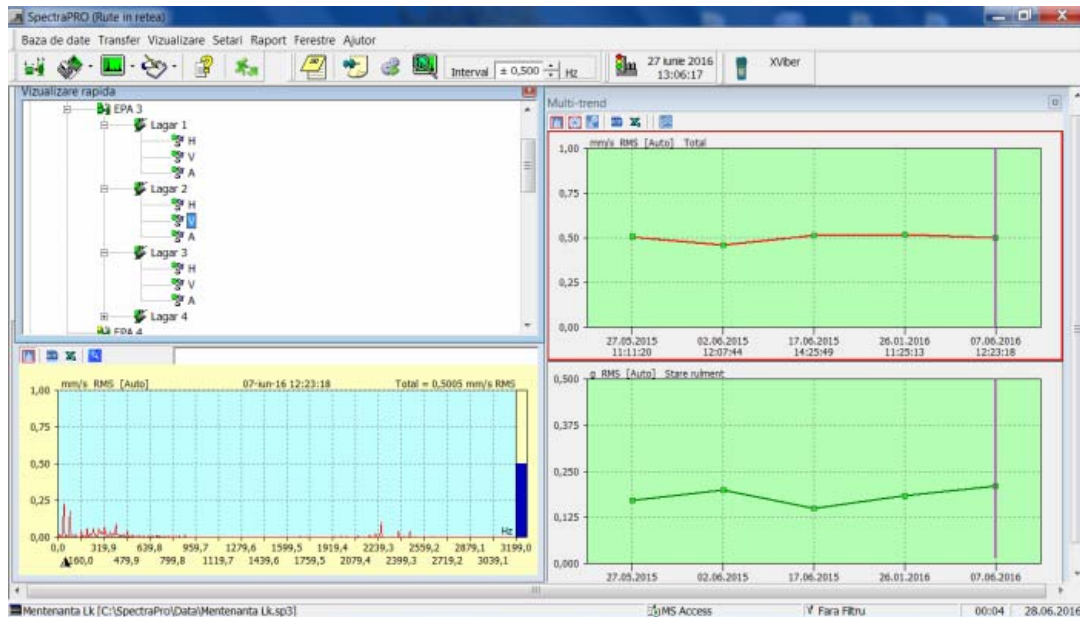


Fig. 10 – EPA no.3 : Bearing No 2 – Vertical direction

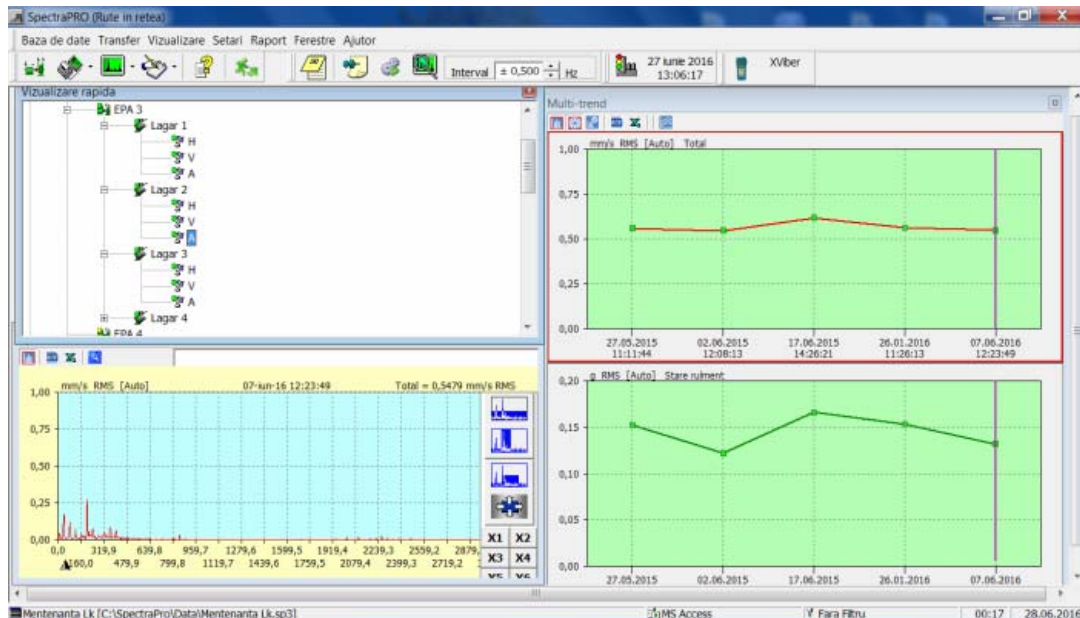


Fig. 11 – EPA no.3 : Bearing No 2 – Axial direction

2.3. Evolution of wear in the bearing No.3.

Figure 12 presents the variation wear of mounted bearing No. 3 measured in units of gravitational acceleration g , depending on the rotation speed of the machine RPM .

According to the four diagrams of Figure 12, the bearing wear of mounted bearing no. 2 is $0.36 g$ - this is a very good value, considering that was acquired after equipment operating longer than one year (values are measured on 28.06.2016).

In Figures 13, 14, 15 are bearing mounted on the observed evolution of the wear of the bearing no. 3 values are measured on 28.06.2016:

- In the horizontally direction: $RMS\ OVERALL = 1.182\ mm / s$, the bearing wear = $0.36\ g$ (Figure 13).
- The vertical direction: $RMS\ OVERALL = 0.991\ mm / s$, the bearing wear = $0.34\ g$ (Figure 14).
- In the axial direction: $RMS\ OVERALL = 0.572\ mm / s$, the bearing wear = $0.61\ g$ (Figure 15).

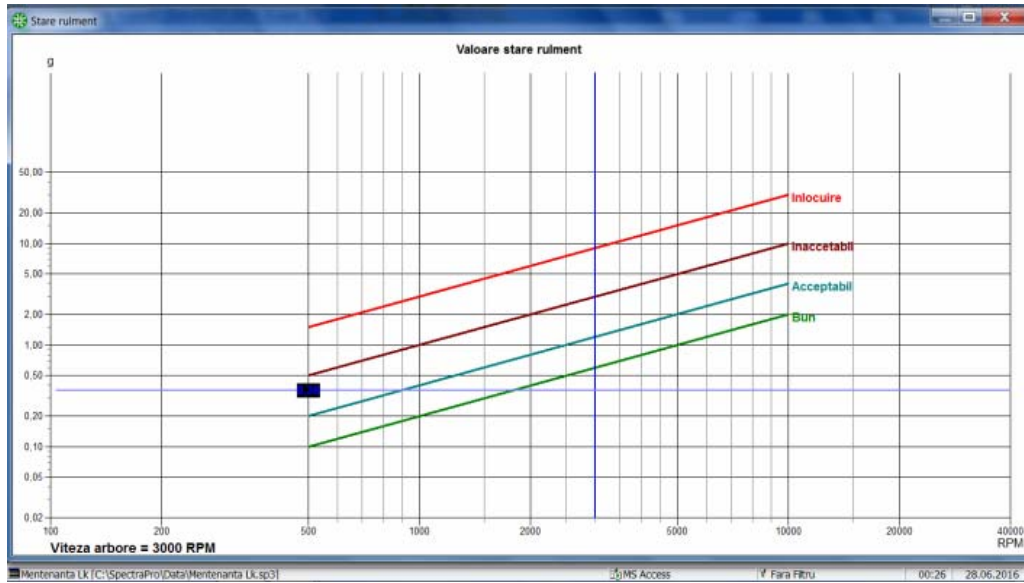


Fig. 12 – EPA No.3 : The bearing wear of mounted bearing no. 3

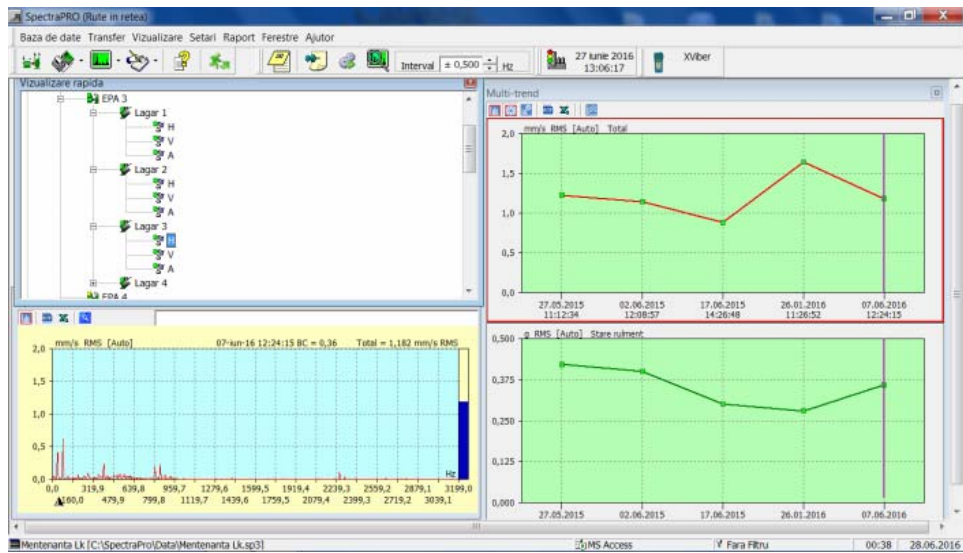


Fig. 13 – EPA no.3 : Bearing No 3 – Horizontally direction

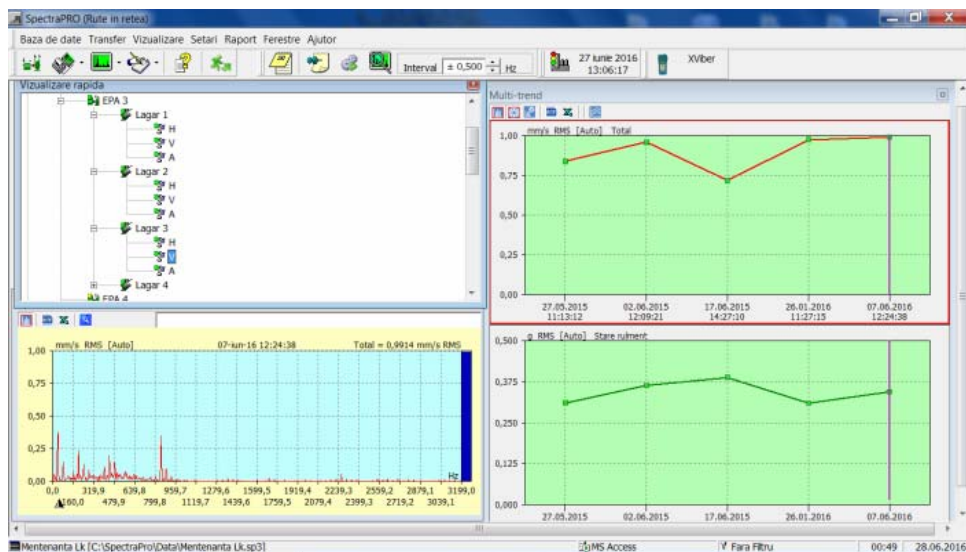


Fig. 14 – EPA no.3 : Bearing No 3 – Vertical direction

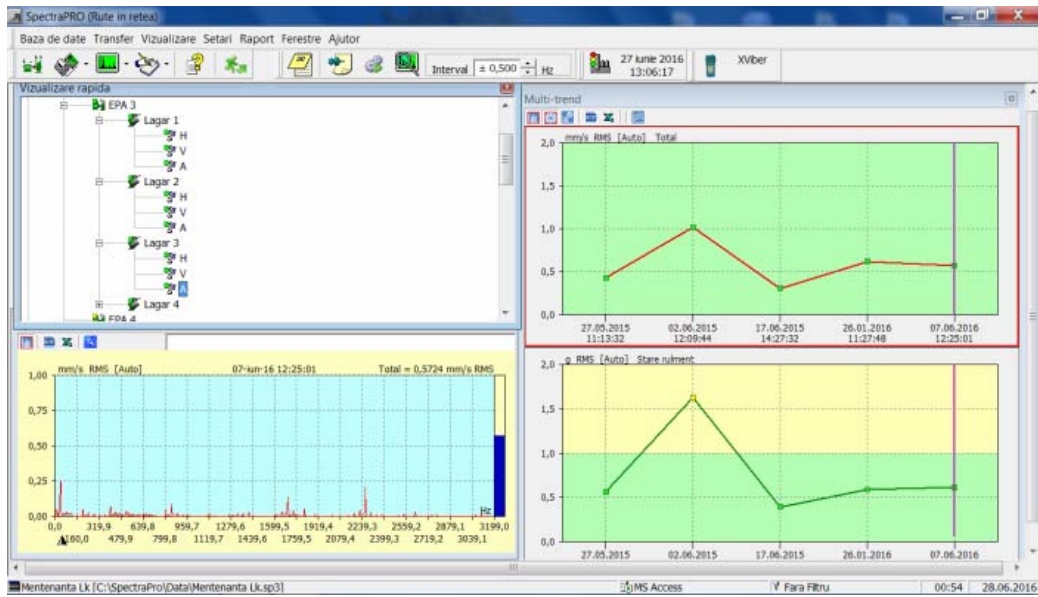


Fig. 15 – EPA no.3 : Bearing No 3 – Axial direction

2.4. Evolution of wear in the bearing No.4.

Figure 16 presents the variation wear of mounted bearing No. 4 measured in units of gravitational acceleration g , depending on the rotation speed of the machine RPM.

According to the four diagrams of Figure 12, the bearing wear of mounted bearing no. 4 is $0.57 g$ - this is a very good value, considering that was acquired after equipment operating longer than one year (values are measured on 28.06.2016).

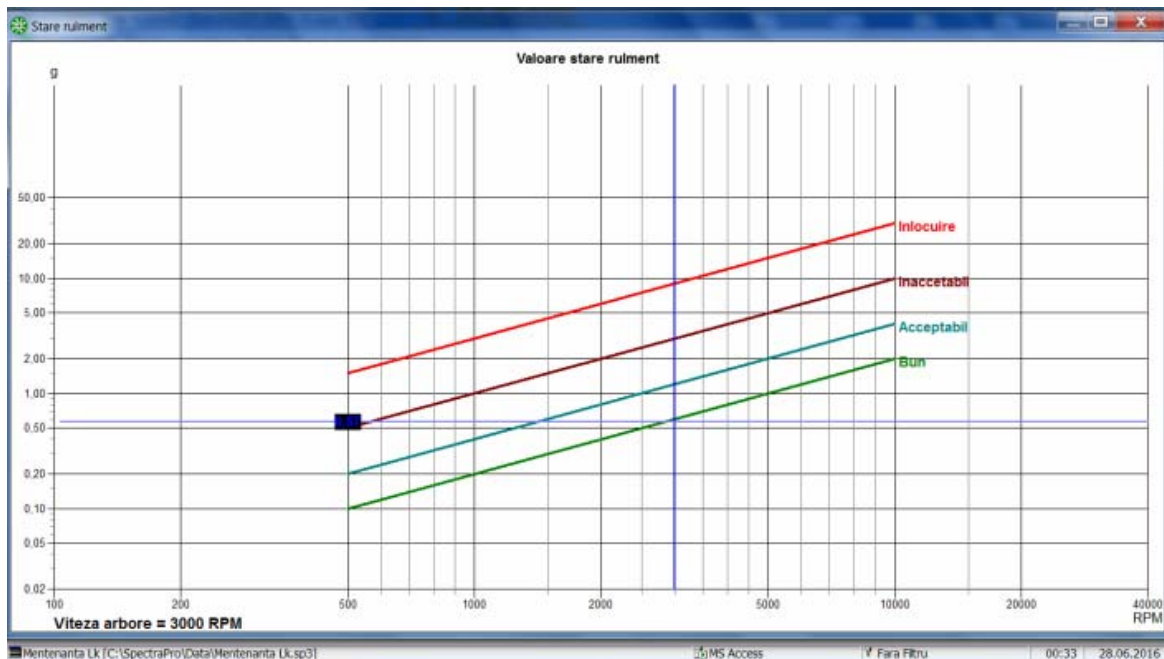


Fig. 16 – EPA No.3 : The bearing wear of mounted bearing no. 4

In Figures 17, 18, 19 are bearing mounted on the observed evolution of the wear of the bearing no. 4 values are measured on 28.06.2016:

- In the horizontally direction: RMS OVERALL= $0,6142 mm / s$, the bearing wear= $0.57 g$ (Figure 17).

- The vertical direction: RMS OVERALL = $0.8525 mm / s$, the bearing wear = $0.71 g$ (Figure 18).

- In the axial direction: RMS OVERALL= $0.656 mm / s$, the bearing wear = $0.64 g$ (Figure 19).

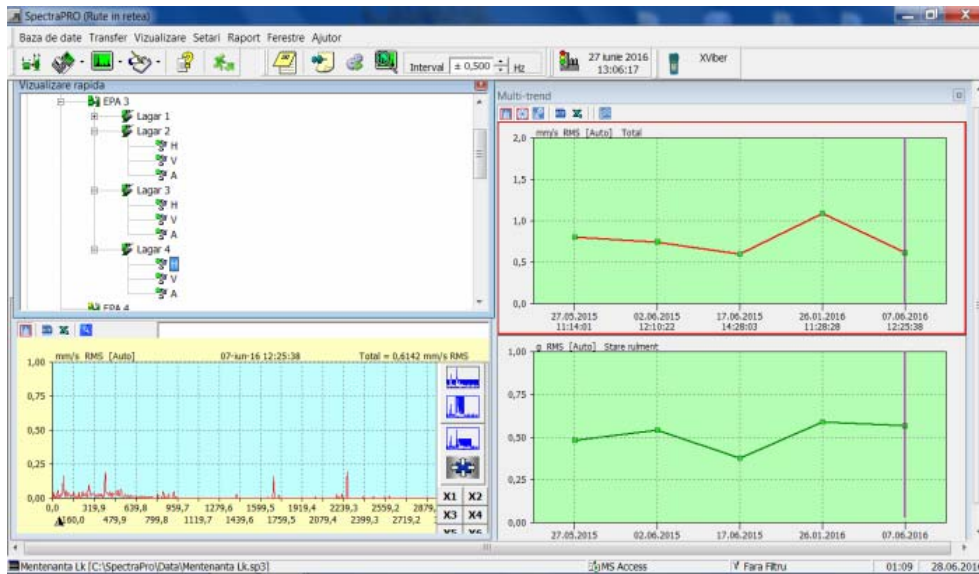


Fig. 17 – EPA no.3 : Bearing No 4 – Horizontally direction

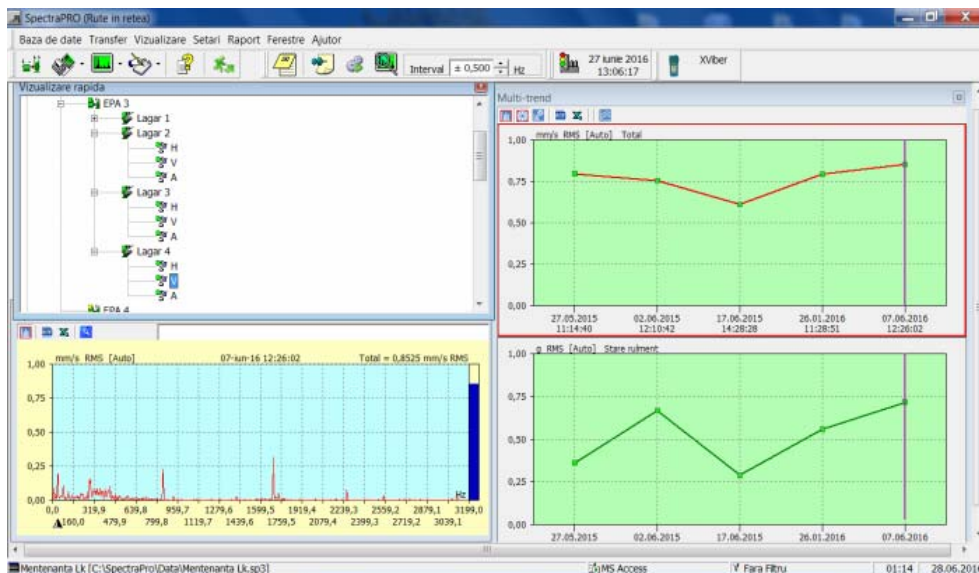


Fig. 18 – EPA no.3 : Bearing No 4 – Vertical direction

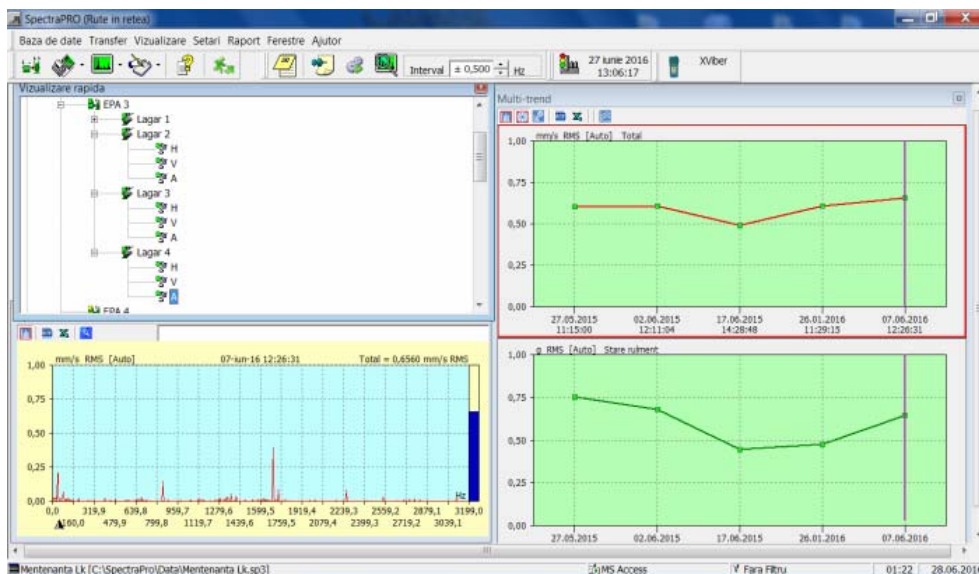


Fig. 19 – EPA no.3 : Bearing No 4 – Axial direction

3. CONCLUSIONS

- Appendix 1 contains the report of wear bearing of equipment studied **CET2/EPA 3** obtained on June 28, 2016 and shows the status of operation of the equipment; this report can be imported into a database containing information about wear and maintenance program to be watched.
- Due functional role in the technological and particular importance of this equipment, application program properly maintenance will lead to operation at nominal parameters of equipment, in good condition throughout the period of operation envisaged - **this is the first point of the concept of maintenance proactive;**
- Implement a software maintenance is the main component of a database containing the results of measurements for at least one year, its processing showing: history of operation equipment, the failures that have occurred and how they were resolved, as it influences plant productivity - **this is the second point of the concept of proactive maintenance ;**
- Knowledge of the technical condition of equipment at any time, but especially knowing the trend for depreciation of machinery, provides predictability on the operation Equipment for the foreseeable future, and smart planning repairs to reduce production losses, reduce costs repeated, avoiding damage human and material - **this is the third point of the concept of proactive maintenance.**

REFERENCES

- [1] Introducere în vibrații - Ref. Doc. MI 119 – Notă tehnică / Mobil Industrial – Pitești (2013) www.mobilindustrial.ro
- [2] Menținerea utilajelor dinamice vol . 1 – Mobil Industrial AG – Pitești (2011) www.mobilindustrial.ro
- [3] Vibration Calibration Technique and basics of Vibration Measurement - Torben R. Licht – Singapore 2011
- [4] Vibration Monitoring Predictive Maintenance, King, Joseph, W., Industrial Fuel Conference, Purdue university 1988
- [5] An Introduction to Vibration Analysis Theory and Practice, de Silva, Clarence W. Boca Raton: CRC Press LLC, 2000
- [6] Automated machinery maintenance – Bill Powel , Tony Burnet
- [7] Bearing vibration analysis – Connected Technology Center - Training modules
- [8] Ghidul analistului de vibrații – Costin Ciprian Ilie 2001
- [9] Reliability –Centered Maintenance, Anderson R.T., Neri L., Elsevier Science Publishing, London, England, 1990
- [10] Quality and Reliability of Technical Systems, Birolini A., Springer – Verlag, Berlin, 1994
- [11] *Fiabilitatea, mentenabilitatea și disponibilitatea sistemelor tehnice*, Burlacu, G., ș.a., Editura MatrixRom, București, 2005
- [12] Idhammar I., Preventive Maintenance, Essential Care and Condition Monitoring Book, IDCON Inc. 1999
- [13] Pavel, A., *Siguranța în funcționare a utilajelor petrochimice* (vol. 1 – 3), Editura Tehnică, București, 1987

APPENDIX 1

S.C. VIROMEK SOLUTION S.R.L.

Date: 28 .06. 2016

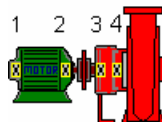
Time: 01:38

Maintenance report

Lk

Equipment: CET 2/EPA 3

Horizontal mounting



Measuring point	Direction	Date	RMS/gBC Value	Measurement units	W HI	D HI
Bearing 1	H	27.06.2016	1,823	mm/s RMS	4,00	7,00
	H	27.06.2016	0,115	g	1,00	2,00
	V	27.06.2016	0,438	mm/s RMS	4,00	7,00
	V	27.06.2016	0,077	g	1,00	2,00
	A	27.06.2016	0,642	mm/s RMS	4,00	7,00
	A	27.06.2016	0,088	g	1,00	2,00
Bearing 2	H	27.06.2016	1,015	mm/s RMS	4,00	7,00
	H	27.06.2016	0,179	g	1,00	2,00
	V	28.06.2016	0,501	mm/s RMS	4,00	7,00
	V	28.06.2016	0,210	g	1,00	2,00
	A	28.06.2016	0,548	mm/s RMS	4,00	7,00
	A	28.06.2016	0,132	g	1,00	2,00
Bearing 3	H	28.06.2016	1,182	mm/s RMS	4,00	7,00
	H	28.06.2016	0,358	g	1,00	2,00
	V	28.06.2016	0,991	mm/s RMS	4,00	7,00
	V	28.06.2016	0,344	g	1,00	2,00
	A	28.06.2016	0,572	mm/s RMS	4,00	7,00
	A	28.06.2016	0,611	g	1,00	2,00
Bearing 4	H	28.06.2016	0,614	mm/s RMS	4,00	7,00
	H	28.06.2016	0,566	g	1,00	2,00
	V	28.06.2016	0,853	mm/s RMS	4,00	7,00
	V	28.06.2016	0,716	g	1,00	2,00
	A	28.06.2016	0,656	mm/s RMS	4,00	7,00
	A	28.06.2016	0,645	g	1,00	2,00

TRIBOLOGICAL CHARACTERIZATION OF THE NANOSTRUCTURED THIN FILMS DEPOSITED BY INTELLIGENT METHODS, FOR MECHATRONIC AND BIOMEDICAL APPLICATIONS

Valentin GORNOAVA¹, Gheorghe Ion GHEORGHE^{1,2}, Liliana-Laura BADITA¹

¹National Institute of Research and Development in Mechatronics and Measurement Technique, Bucharest

²Valahia University of Târgoviste, Faculty of Materials Engineering and Mechanics

E-mail: valentin_gornoava@yahoo.com

Abstract. *The main objectives of the present project are to study and to improve mechanical properties of different systems from mechatronic and biomedical domains, in order to increase their functionality and life span. This is why nanostructured thin films (e.g. Al, Cr, Ti, Ti/Al multilayers) were deposited on different steel substrates, used in mechatronic and biomedical applications. By the characterization of coated surfaces of the products used in various fields such as medicine, mechatronics, electronics, etc. depends their proper operation, durability and reliability. This is the main reason why, we studied new types of layers and multilayers using Atomic Force Microscopy and scratch tests. The main result of the realized tests is that all studied nanostructured thin films offer the possibility of increasing the lifetime of substrates, being an important factor for proper functional operation, durability and reliability of the final systems in which they are used.*

Keywords: *nanometric coatings, thin films, structural characterization, mechatronic methods*

Introduction

Thin films (made of materials with micro and nano structures) deposited by intelligent mechatronic methods can be used in various fields, such as mechatronics (mechatronic components), electronics, and medical (implants - dentures, orthopaedic).

During the time, in the institute we have tried different methods for obtaining materials with improved physical and mechanical properties, but it has been proven that the most important method in this process is the deposition of thin films. It has been revealed that the key factor to increase the durability of the materials coated with thin layers of nanostructured materials is to provide a tightly adhering coating on the substrate.

Thus, the project team has set the research and development of thin films deposited, by means of intelligent modern methods, on materials used in mechatronic applications such as: high-precision gears for miniaturized construction, bearings for precision equipment, components of mechatronics equipment for measuring, positioning and adjustment: races, guides, grippers, actuators, components for biomedical devices, MEMS & NEMS, etc., in order to increase the lifetime of these materials coated with thin films.

The idea of this project started from older studies, which aimed to establish methods to ensure high durability of prosthetic components. In the

conclusions on severe mechanical stresses faced prosthetic elements, complex investigations were made about theoretical and experiential modelling of tribological behaviour of these biomedical components. Hip prostheses specimens were made and were coated with nanoscale thin films, respectively TiN. Scratch tests were performed with constant load and demonstrated a substantial increase of hardness for the surfaces coated with biocompatible nanostructured materials. The present project aims to extend these experiments to new types of deposited nanostructured films by various ultra-modern procedures, and to demonstrate the functionality of already formulated concept.

In the present studies, based on mentioned documentary studies and internal analysis, Ti, Cr, Al thin films and Ti/ Al multilayer were deposited on the following steel substrates:

- OLC 45 (rolled steel quality) used in the production of mechatronic actuators, roto-translational mechanisms, components for industrial robots, measuring pivots, centring pivots, gauges, bushings, etc.;

- Rul 1 (ball bearing steel) used for the production of mechatronic actuators, measuring pivots, positioning supports, manufacture of small bearings, tools, dowel drilling, gauges, etc.;

- C120 steel, used into mechatronics applications to produce moulds, punches, perception heads, sensors, calibres, etc.;

- OSC steel, used in mechatronics to produce perception heads, gauges, thread gauges, dies, etc.

These substrates were chosen because of the importance they have in engineering applications; are commonly used in mechatronic components that are subject to the phenomenon of wear throughout the operating cycle.

Experimental research on qualitative increase of physical and mechanical properties of steels, via deposition of thin films

In a specialized laboratory, with controlled ambient environment, deposition of Ti, Cr, Al thin films, and Ti/ Al multilayer was realized by "method of deposition by evaporation electron beam" using a TEMESCAL FC-2000 system (Figure 1). Through

Besides the deposition of nanostructured thin films, this technical paper put a valuable focus on characterization of the obtained thin films surfaces with micro and nanostructures. In the present scientific article we present a part of the originally program of thin film deposition, designed to improve the functional characteristics of the components/ parts of mechatronic structures by coating with micro/ nanostructured materials and a part of the structural characterization results.

the process of evaporation deposition electron beam have been deposited layers of Ti, Cr, Al and multilayer Ti / Al on four types of steel: OLC 45, Rul 1, C 120 and OSC.



Fig. 1: TEMESCAL FC-2000 –deposition system by electron beam evaporation

Temescal FC-2000 is a versatile evaporation system that accepts a variety of accessories to meet almost any requirement. Engineered for efficient operation and clean room compatibility, these systems combine maximum flexibility with ease of use. The FC-2000 is a fast-cycle, load-locked system that allows the source to remain under vacuum during substrate reloading.

To begin operation TEMESCAL FC-2000 were tested and put into operation the system components: control system, power supply, pumping and vacuum control air system, water system, vacuum chamber, the source beam electrons.

TEMESCAL Control System (TCS) provides a fully integrated process control, operating in ways including password protected, also provides variable monitoring, tracking and trend data archiving process.

In TCS Automatic Mode, the user performing fully automatic control of programmed recipes composed of up to twenty steps of the process; being available self-pumping and self-ventilation operations, and also automatic testing of the growth rate.

More practical and preferable, is the TCS Manual Mode, which allows the user matching easy process parameters, individual exploiting major components and subsystems with full protection blocking, and performing non-automatic processes for coating of a single thin film, on a whole lifecycle.

TCS Operating Mode Services provides basic-level control, lock on any valves, pumps, motors or power supply system.

The main factors that have ensured deposits accurate, pre-set parameters are:

- Electron beam sources of TEMESCAL offers improved convenience and reliability and transfer in applications, leading to specialized coatings;

- Thoroughly controller of the electron beam of TEMESCAL offers full digital operation, internal storage up to 64 user-defined models and compatibility with almost any electron beam gun;

- Programming software based on Windows™ and a hand controller with remote control it provides precision and flexibility required by the most stringent PVD processes with electron beams.

Experimental results

Ti, Cr, Al thin films obtained had a thickness of 50 nm and the Ti/ Al multilayer 100 nm (50 nm each metallic layer). These nano-layers were deposited on various substrates of steel from those selected as highly used in mechatronics industry, for components that are in a gearing dynamic, with long direct contact, inducing wear accentuated during the whole working cycle, like: OLC 45, RUL 1, C120, OSC.

The thickness of thin films obtained was measured using quartz crystal microbalance method.

A quartz crystal microbalance (QCM) measures a mass variation per unit area by measuring the change in frequency of a quartz crystal resonator. The resonance is disturbed by the addition or removal of a small mass due to oxide growth/decay or film deposition at the surface of the acoustic resonator.

In Figure 2a-d are shown images of Ti thin films deposited by electron beam evaporation on the four types of substrates enunciated before.

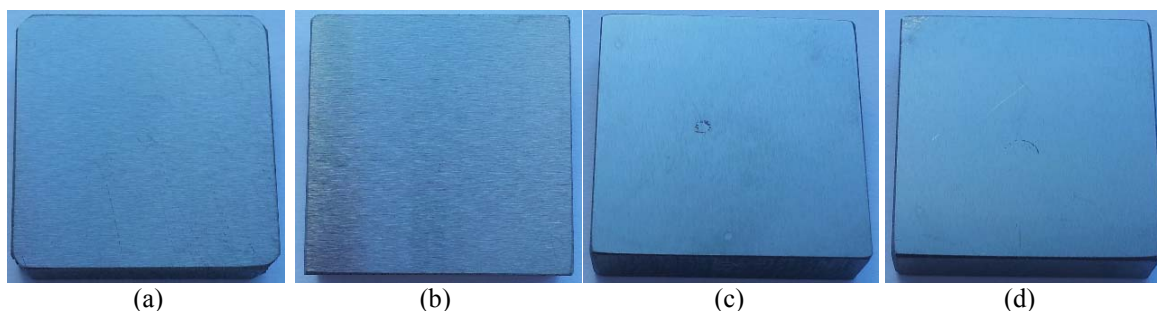


Fig. 2: Photos of Ti films deposited by the electron beam evaporation deposited on steel substrates 4: (a) OLC 45; (b) RUL1; (c) C120; (d) OSC

These thin films were structurally characterized using atomic force microscopy. Such a system helps to determine few parameters, in order to obtain supplementary information about the structure.

We took some instant images using the CCD camera of the NTEGRA NT-MDT atomic force microscope, in order to see the interaction points between the thin films and materials used as substrates. These information will be important in the future, for adhesion determination, when we

proposed to make some physico-mechanical characterization of the obtained thin films.

In the next figure (Figure 3) it can be observed the interaction surface between the Al thin film of 50 nm and the 4 types of steel substrates. It can be clearly seen that between the layer and substrate is a good connection, the thin films materials penetrating through all the substrate material irregularities. In the case of the Ti/ Al double layer, was also clearly seen this kind of interaction between the thin layer and substrate, but also between the two layers deposited in order to obtain a multilayer.

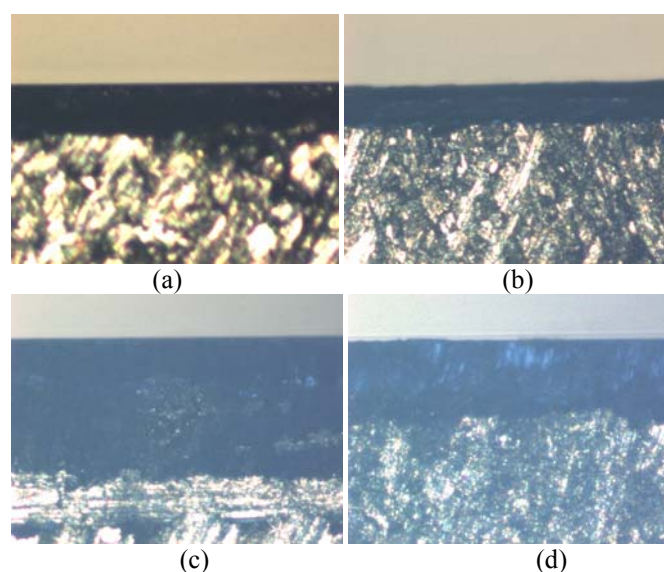


Fig. 3: Photos of the interaction surface between the Al thin films deposited by the electron beam evaporation, and the 4 types of steel substrates: (a) OLC 45; (b) RUL1; (c) C120; (d) OSC

Using atomic force microscopy, we made surfaces scans of $50 \times 50 \mu\text{m}$, and we obtained few topographic parameters (Figure 4).

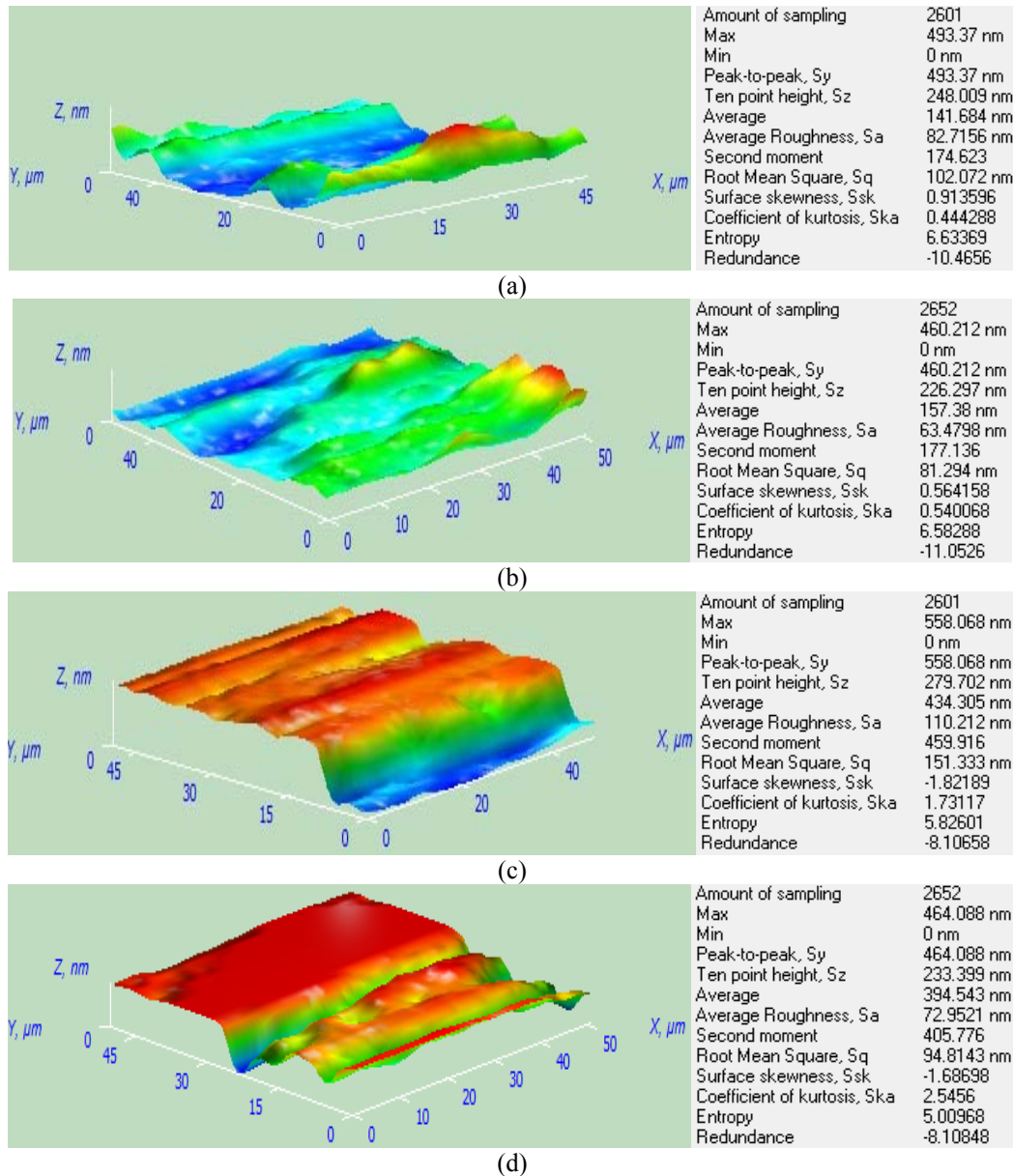


Fig. 4: Atomic force microscopy analysis of Ti/Al thin layers deposited on the 4 types of steel substrates: (a) OLC 45; (b) RUL1; (c) C120; (d) OSC

Analysing all these obtained results, we can conclude that the thin films were deposited uniformly on all the substrates used, but have a relatively high

roughness. This can be due to some possible defects of the substrate.

Table 1. Mean values of the roughness (nm) of the thin layers deposited on different type of substrates using electron beam evaporation.

Thin film	Substrates	Mean roughness (nm)
Ti	OLC 45	110,571
	RUL1	110,898
	C120	78,025
	OSC	87,486
Al	OLC 45	110,005
	RUL1	74,347
	C120	78,880

	OSC	52,642
Cr	OLC 45	43,845
	RUL1	85,59
	C120	72,557
	OSC	149,135
Ti/ Al	OLC 45	84,467
	RUL1	105,063
	C120	78,025
	OSC	74,766

Conclusions

In this paper are presented a part of the results obtained after the structural analysis of nanomaterials thin layers deposited on some steel substrates using the electron beam evaporation. We choose to study metallic (Ti, Cr, Al) thin films, monolayer and multilayer, with thickness of 50 and 100 nm, because of its importance in mechatronic applications.

Different types of steel used as substrates are used in applications like: high-precision gears in miniaturized constructions, high precision bearings, components of mechatronic equipment for measuring, positioning and adjustment: runways, guideways, grippers, etc., components for biomedical devices, MEMS & NEMS.

It was observed that between the deposited layers and substrates is a good connection, the thin films materials penetrating through all the substrate material irregularities. In the case of the Ti/ Al double layer, was also clearly seen a good interaction between the thin layer and substrate, but also between the two layers deposited in order to obtain a multilayer.

The main conclusion that was reached after the atomic force microscopy structural characterizations is the fact that it was proved the deposition of thin films with a uniform structure that can be tested mechanically in the next stages of the project.

References

- [1] A. O. Mateescu, G. Mateescu, "Multilayer inorganic/organic tribological coatings for space applications-SpaceCoat", Contract with Romanian Space Agency, 2013-2014
- [2] S. L. Rohde, W. D. Munz, "Sputter deposition in Advanced Surface Coating": A Handbook of Surface Engineering, Glasgow and London, 1991, 96-126.
- [3] W. D. Sproul, "Physical vapour deposition tool coatings". Surface and Coatings Technology. 1996; 81, 1-7.
- [4] I. Stamatina, "Nanomaterials. Applications in biosensors, renewable energy, medicine, biology". University of Bucharest, 2008.
- [5] Springer Handbook of Nanotechnology, Buschan Editor.
- [6] R. Pato, "Multifunctional Titanium Nitride Thin Films", PhD thesis.
- [7] G. Vermesan and colab., "Introduction to surface engineering", Dacia Publishing House, Cluj-Napoca, Romania, 1999.
- [8] A. W. Robert and A. B. Heather, "Basic Theory Atomic Force Microscopy (AFM)". Department of Chemistry, Northern Kentucky University, Highland Heights, KY 41099.
- [9] Patent no. 128144/ 30.06.2014, "Coating methods of the metal parts with lubricant thin layers".
- [10] Gheorghe, Gh.: Mecatronica & Sistemele Cyber – Mecatronice, ISBN 978-606-8261-22-5, 2015, Ed. CEFIN – România
- [11] O, Donțu, ș.a: "Influence of thermal deformations in the solid laser medium on the emitted radiation parameter", Journal of Mechanical Engineering, Aug 2005, Vol. 219
- [12] Machado, Jose; Soares, Filomena; Leao, Celina P.; et al., A Virtual Workbench Applied to Automation: Student's Response Analysis, Controlo'2014 – Proceedings of the 11th Portuguese Conference on Automatic Control Vol: 321, Pages 709-719, Published: 2015, Times Cited: 0; DOI:10.1007/9783319103808_68;
- [13] Machado, J.; Campos, J. C.; Sevcik, L; et al., Development of Dependable Controllers in The Context of Machines Design, Modern Methods of Construction Design, Pages:125 131, Published: 2014, DOI: 10.1007/9783319052038_18